Technische Universität München

TUM School of Engineering and Design

Microstructure, Mechanical Properties and High-Pressure Torsion Processing of the Refractory High-Entropy Alloy MoNbTaTiVZr

Chuyi Duan

Vollständiger Abdruck der von der TUM School of Engineering and Design der Technischen Universität München zur Erlangung des akademischen Grades eines

Doktors der Ingenieurwissenschaften (Dr.-Ing.)

genehmigten Dissertation.

Vorsitz: Prof. Dr. techn. Jan Torgersen

Prüfer der Dissertation:

1. Prof. Dr. mont. habil. Dr. rer. nat. h.c. Ewald Werner
2. Prof. Dr. mont. habil. Reinhard Pippan

Die Dissertation wurde am 15.06.2023 bei der Technischen Universität München eingereicht und durch die TUM School of Engineering and Design am 02.10.2023 angenommen.

子曰：譬如为山，未成一篑，止，吾止也；譬如平地，虽覆一篑，进，吾往也。

— 《论语 · 子罕》

The Master said, “The prosecution of learning may be compared to what may happen in raising a mound. If there want but one basket of earth to complete the work, and I stop, the stopping is my own work. It may be compared to throwing down the earth on the level ground. Though but one basketful is thrown at a time, the advancing with it is my own going forward.”

— *Analects of Confucius, translated by James Legge*

Abstract

Refractory high-entropy alloys (RHEAs) have garnered interest for their exceptional high-temperature properties, making them potential alternatives to conventional superalloys in the aerospace industry. However, their application is challenged by issues such as limited ductility and the difficulty to eliminate chemical segregation. This work investigates the microstructure and mechanical properties of the RHEA MoNbTaTiVZr, fabricated by vacuum arc-melting and processed by the severe plastic deformation (SPD) technique, specifically by high-pressure torsion (HPT).

This study demonstrates that the phase composition of the RHEA aligns more closely with Scheil-solidification simulations than with equilibrium phase composition predictions. It also reveals that the presence of multiple phases contributes to enhanced ductility while maintaining high strength. Moreover, HPT processing results in chemical homogeneity and additional solid solution hardening due to the forced dissolution of the segregated region.

The findings underline the importance of understanding solidification paths in RHEA design and emphasize the advantages of devising multi-phase RHEAs to improve ductility. Furthermore, they highlight the potential of SPD in achieving chemical homogeneity and reveal new insights into the commonly observed microsegregation in RHEAs.

Kurzfassung

Refraktäre Hoch-Entropie Legierungen (engl. *RHEAs*) haben aufgrund ihrer außergewöhnlichen Hochtemperatureigenschaften großes Interesse geweckt, und stellen eine potenzielle Alternative zu herkömmlichen Superlegierungen in der Luft- und Raumfahrtindustrie dar. Ihre Anwendung wird jedoch durch Herausforderungen wie begrenzte Duktilität und Schwierigkeiten bei der Beseitigung chemischer Segregation limitiert. In dieser Arbeit werden die Mikrostruktur und mechanischen Eigenschaften der Legierung MoNbTaTiVZr untersucht, die durch Vakuum-Lichtbogenschmelzverfahren hergestellt und mit einem Verfahren der plastischen Hochverformung (engl. *SPD*), der Hochdruck-Torsion (engl. *HPT*), verarbeitet wurde.
Die Untersuchung zeigt, dass die Phasenzusammensetzung der Legierung eher den Erstarrungssimulationen nach dem Scheil-Gulliver-Modell als den Vorhersagen der Phasenzusammensetzung im Gleichgewicht entspricht. Sie zeigt auch, dass das Vorhandensein mehrerer Phasen zur verbesserten Duktilität beiträgt, während gleichzeitig eine hohe Festigkeit aufrechterhalten wird. Des weiteren führt die HPT-Verarbeitung zur chemischen Homogenität und zusätzlichen Mischkristallhärtung aufgrund der erzwungenen Auflösung der segregierten Region.
Die Erkenntnisse verdeutlichen die Wichtigkeit des Verständnisses der Erstarrungspfade bei der Entwicklung von RHEAs, und unterstreichen die Vorteile der Gestaltung von mehrphasigen RHEAs zur Verbesserung der Duktilität. Sie demonstrieren auch die Möglichkeit der SPD zur Erzielung chemischer Homogenität und geben neue Einblicke in die häufig beobachtete Mikroseigerung in RHEAs.

Vorwort

Die vorliegende Arbeit entstand während meiner Tätigkeit als wissenschaftlicher Mitarbeiter am Lehrstuhl für Werkstoffkunde und Werkstoffmechanik (seit August 2022 Lehrstuhl für Werkstoffwissenschaften) der Technischen Universität München in den Jahren von 2019 bis 2023.

Zunächst möchte ich meine tiefste Dankbarkeit gegenüber meinem Doktorvater, Herrn Prof. Ewald Werner, zum Ausdruck bringen. Dieser Dank gilt nicht nur für die Gelegenheit zum Schreiben dieser Arbeit, sondern auch für seine große Geduld und Ermutigung während der teilweise erfolglosen Phasen meiner Forschung. Darüber hinaus möchte ich Herrn Prof. Reinhard Pippan von der Österreichischen Akademie der Wissenschaften (ÖAW) herzlich danken, sowohl für sein Interesse an der Prüfung im Rahmen des Promotionsverfahrens als auch für die Arbeit im Zusammenhang mit High-Pressure Torsion (HPT).

Des Weiteren möchte ich mich bei folgenden Personen am Lehrstuhl bedanken: Herrn Prof. Jan Torgersen für die vielen wertvollen Diskussionen und die Finanzierung der letzten fünf Monate meiner Anstellung, Herrn Dr.-Ing Christian Krempaszky für seine stetige Hilfsbereitschaft, Frau Yvonne Jahn für die organisatorische Angelegenheit, Frau Dr. mont. Zhonghua Wang für ihre Unterstützung beim Erlernen der Rasterelektronenmikroskopie, Frau Carola Reiff für die Probenvorbereitung für die Metallographie, Herrn Dr.-Ing Alexander Fillafer für die Reparatur vieler Instrumente, Herrn Dr.-Ing Marius Reiberg für die Zusammenarbeit und wissenschaftliche Diskussion, Herrn Patrick Hegele für die Hilfe bei der Röntgendiffraktometrie, Herrn Stefan Humplmair und Herrn Kjetil Baglo für die Bearbeitung meiner Proben, sowie allen anderen Kollegen für die freundliche Arbeitsatmosphäre.

Ferner möchte ich den nachstehenden Personen danken: Herrn Dr. rer. nat. Xiaohu Li vom Heinz Maier-Leibnitz Zentrum (MLZ) für die Hilfe bei den Versuchen am Deutschen Elektronen-Synchrotron, Herrn Armin Kriele vom MLZ für den Zugang zum Materials Science Lab am MLZ, Frau Dr.-Ing Zirong Peng von der Carl Zeiss AG und Herrn Dr.-Ing

Aleksander Kostka von der Ruhr-Universität Bochum für die Transmissionselektronenmikroskopie, Herrn Peter Kutlesa von der ÖAW für die Durchführung der HPT-Versuche, sowie Herrn Dr.-Ing Yulong Zhao vom Lehrstuhl für Elektrische Energiespeichertechnik für das Korrekturlesen dieser Arbeit.
Ein besonderer Dank gilt meinen Eltern, die mich zur Welt gebracht haben, und meiner lieben Frau Qin Wang, für ihren Beistand in der schwierigen Zeit.

List of Symbols and Abbreviations

Latin letters

Symbol	Description	Unit
a	lattice constant	Å
c_i, c_j	atomic fraction of the i-th/j-th component	–
c_0, c_1, c_2	solute concentrations in solidification	–
D	average diagonal length of indentation impression	mm
f	volume fraction	–
H	microhardness	HV
l	length of rod	mm
M	molar mass	g/mol
n	number of components in system	–
N	number of revolutions in HPT	–
P	indentation load	kg
Q	magnitude of wave vector	1/Å
r	radial position within the disk	mm
r_e	equivalent atomic radius of a crystal structure	Å
r_i	atomic radius of the i-th component	Å
$\bar{r}$	average atomic radius	Å
R	universal gas constant	J/(K·mol)
R_0	radius of disk	mm
R_m	compressive strength	MPa
$R_{p0.2}$	0.2 %-offset yield strength	MPa
t	thickness of disk	mm
T	temperature	K

Symbol	Description	Unit
T_{m}	average melting temperature	K
T_{SC}	temperature at spinodal point	K
T_{BC}	temperature at binodal point	K
x	addition of vanadium	–

Greek letters

Symbol	Description	Unit
ε	von Mises equivalent strain	–
ε_{f}	fracture strain in compression tests	–
ΔG_{mix}	Gibbs free energy of mixing	kJ/mol
ΔH_{mix}	mixing enthalpy	kJ/mol
ΔH_{ij}	mixing enthalpy of binary liquid alloys	kJ/mol
ΔS_{mix}	mixing entropy	J/(K mol)
$\Delta\chi_{\mathrm{Allen}}$	Allen-electronegativity mismatch factor	–
χ_{Allen}	Allen-electronegativity	–
δ	atomic size mismatch	–
γ	shear strain in pure torsion	–
λ	wave length	Å
μ	parameter indicating the ratio of T_{m} to T_{SC}	–
Ω	parameter indicating the ratio of ΔS_{mix} to ΔH_{mix}	–
ρ	density	g/cm^3
θ	diffraction angle	°

Abbreviations

Abbreviation	Meaning
at.	atomic
a.u.	arbitrary unit
ADF	annular dark-field imaging
BCC	body-centered cubic
BF	bright-field imaging

Abbreviation	Meaning
BSE	backscattered electron
CALPHAD	CALculation of PHAse Diagrams
CSD	coherently scattering domain
DESY	Deutsches Elektronen-Synchrotron
EBSD	electron backscatter diffraction
EDS	energy-dispersive X-ray spectroscopy
FCC	face-centered cubic
FIB	focused ion beam
HCP	hexagonal close-packed
HEA	high-entropy alloy
HEXRD	synchrotron high-energy X-ray diffraction
HPT	high-pressure torsion
HT	heat treatment
HV	Vickers hardness
IPF	inverse pole figure
RMS	root mean square
RHEA	refractory high-entropy alloy
RT	room temperature
SAED	selected area electron diffraction
SE	secondary electron
SEM	scanning electron microscopy
SPD	severe plastic deformation
STEM	scanning transmission electron microscopy
TEM	transmission electron microscopy
UFG	ultra-fine grained
UMH	ultra-microhardness
WEDM	wire electrical discharge machining
XRD	X-ray diffraction

Contents

Chapter 1

Introduction

1.1 Refractory high-entropy alloys

The rapid development of the aerospace industry and the growing demand for energy solutions highlight the importance of designing high-efficiency turbines for aircraft engines and power generators. However, achieving greater efficiency in turbine design typically involves operating at elevated temperatures and pressures [1]. This condition, in turn, presents new challenges for developing materials with enhanced mechanical properties at high temperatures.

When selecting materials, polymers and their composites often exhibit decomposition at high temperatures, while ceramics face limitations in applications due to their lack of ductility. In contrast, metals generally offer advantages over these materials, stably demonstrating high strength and ductility even at high temperatures. Among different high-temperature materials, superalloys are commonly used in turbines, such as the commercially available Ni-based alloys Haynes-230 and Inconel-718. Nevertheless, their exceptional mechanical properties are still constrained due to rapid degradation at temperatures above 800 °C. Additionally, a reduction in strength is frequently observed at temperatures exceeding 0.6 of their melting point [2]. Consequently, there is a growing need for the development of innovative metallic materials.

A novel group of alloys, high-entropy alloys (HEAs), has been gaining attention due to their exceptional properties. The first developed HEA was CoCrFeMnNi, which has been named the Cantor-alloy after its originator [3, 4]. Unlike traditional alloys that rely on a few principal alloying elements, HEAs contain equimolar or near-equimolar concentrations of multiple principal alloying elements. This characteristic apparently leads to a substantial configurational entropy, which is supposed to promote the formation of a

single-phase solid solution and prevent the emergence of intermetallics [5]. Such a single-phase solid solution, comprising atoms with large differences in atomic radii, is expected to exhibit a considerable lattice distortion due to the deviation of atoms from their ideal sites [5, 6]. This lattice distortion impedes dislocation motion and results in significant hardening effects, and hence enhancing the alloy's strength. A schematic illustration of the crystal structure of such HEAs is shown in Fig. 1.1.

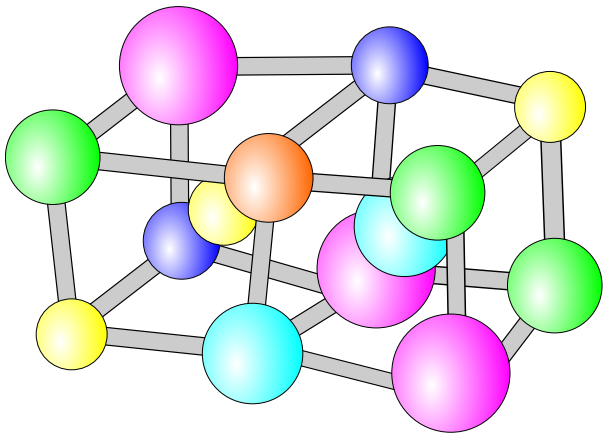

Fig. 1.1: Schematic illustration of the crystal structure in high-entropy alloys exhibiting severe lattice distortion, with different colors representing different atoms.

The broad definition of HEAs allows for a wide range of elemental combinations. Furthermore, recent research has also indicated that mechanical properties can be optimized by adjusting the concentration that deviates from equimolar ratios [7]. This finding expands the definition of HEAs to include alloys with element concentrations ranging from 5 % to 35 %, presenting nearly limitless possibilities for elemental combinations for HEAs [6]. Hence, since introducing the HEAs concept, the primary task has been exploring compositions with outstanding properties.

Based on the constituent elements, HEAs can be classified into several subgroups. Among them, extensive research has been conducted on the exploration of two main subgroups: 3d-transition metal HEAs (3d-HEAs) and refractory HEAs (RHEAs) [8]. While 3d-HEAs still exhibit limitations for applications at elevated temperatures, refractory high-entropy alloys (RHEAs), which predominantly consist of refractory elements, have emerged as a promising alternative for Ni-based superalloys [9]. A prominent example of RHEA is HfNbTaTiZr, often referred to as the Senkov-alloy after its developer [10]. These refractory elements typically exhibit high melting points, and their incorporated alloys have been demonstrated to retain strength at higher temperatures [2]. During the exploration of various RHEA compositions, some alloys have been found to overcome the strength degradation above 0.6 of their melting point [2]. Furthermore, novel strengthening and

deformation mechanisms have been proposed for RHEAs, such as local chemical composition fluctuation and multiple dislocation pathways [11, 12]. These novel mechanisms have been demonstrated to result in exceptional mechanical properties in RHEAs.

Despite the extensive research conducted in this field, several questions and challenges still need to be solved. In contrast to the commonly face-centered cubic (FCC) 3d-HEAs, RHEAs typically exhibit body-centered cubic (BCC) crystal structures [6]. The high lattice friction stress in BCC crystals makes dislocation slip more difficult than in the closely packed FCC structure. Therefore, RHEAs typically exhibit brittle fracture, with some maintaining this characteristic even at elevated temperatures of up to 800 °C [13, 14].

Moreover, the arc-melting method is the most commonly used technique to fabricate RHEAs. However, the microstructure obtained from this solidification process often demonstrates microsegregation, such as dendrites. This inhomogeneity of chemical elements is likely due to the significant differences in melting points of the alloying elements and their complex interactions during solidification [2, 15]. There are also different opinions on the phase composition of the microsegregation. While most of the researchers consider this elemental segregation to be single-phase, based on the identification of a single group of peaks in X-ray diffractograms, some researchers define it as two phases with the same crystal structure and similar lattice constants [2, 16]. The microsegregation has been demonstrated to be thermally stable [17, 18]. To eliminate this segregation, a prolonged homogenization process is required, which may last up to 1000 hours [19]. This homogenization is particularly difficult for RHEAs, as the homogenization temperature is also expected to be high due to their elevated melting point.

Therefore, these challenges highlight the need for a more comprehensive study of RHEAs, which is the central focus of this dissertation.

1.2 High-pressure torsion

In metallic materials, common strengthening mechanisms are solid solution hardening, precipitation hardening, work hardening, and grain boundary hardening. While the former two hardening mechanisms can be achieved by optimizing alloying composition and heat treatment procedure, the latter two can be attained by implementing external mechanical processing, such as the severe plastic deformation (SPD) technique. Among the various SPD techniques, high-pressure torsion (HPT) is a well-established method, exhibiting advantages such as the ability to achieve a finer saturation grain size compared to other techniques [20].

The HPT technique can be classified into two types based on the applied constraints: unconstrained and constrained methods. Unconstrained processing often significantly reduces sample thickness due to the outward flow of material, a limitation which can be circumvented in constrained processing [21]. While achieving a perfectly constrained condition is challenging in practice, the quasi-constrained condition has emerged as a promising alternative [21]. A schematic illustration of the quasi-constrained HPT processing is shown in Fig. 1.2.

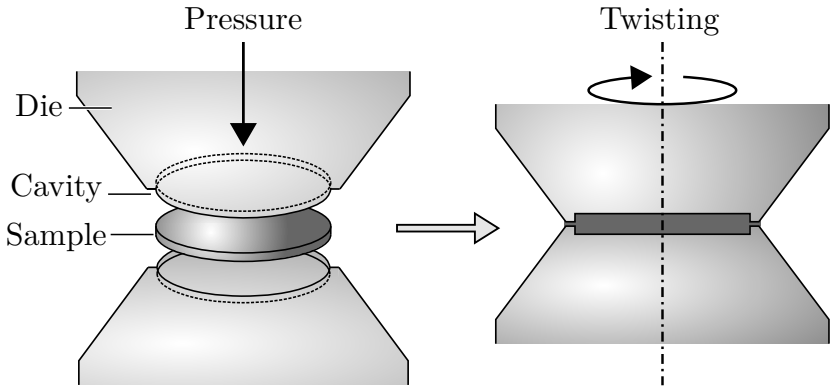

Fig. 1.2: Schematic illustration of the high-pressure torsion processing with a quasi-constrained geometry.

The disk-shaped sample is placed between two anvils containing a cavity that is slightly shallower than the initial sample thickness. A large hydraulic pressure (several GPa) is applied, confining the sample within the cavity with a limited outward flow of material. The concurrent torsion straining induced by the friction between the anvils and the sample forces the sample to deform while preventing it from being damaged due to the quasi-hydrostatic pressure. During the HPT, substantial amounts of crystal defects are introduced, such as dislocations, voids, and grain boundaries. Typical utilization of the HPT is to fabricate ultra-fine grained (UFG) materials with exceptionally high strength [22]. Furthermore, HPT has been found to induce superplasticity in some materials, demonstrating an elongation of over 600 % due to grain boundary diffusion [23]. This property is of great interest given its potential applications in industrial forming operations [20].

The application of HPT has also been extensively employed to investigate the behaviors of both 3d-HEAs and RHEAs, including the single-phase Cantor and the Senkov-alloys [24–26]. Common findings, like UFG microstructures, enhanced strength, and superplasticity, align with observations in conventional alloys. However, unique phenomena have also been observed, such as phase decomposition after subsequent heat treatment, which offers new insights into the character of being single-phase in HEAs.

Furthermore, nanocomposites have been successfully fabricated through HPT processing of two disks of Cantor and Senkov-alloys, revealing new findings such as chemical separation and deformation-induced amorphous microstructures [27]. Interestingly, HPT has also been utilized to fabricate HEAs through mechanical alloying of pure elemental powders [28]. Other examples of investigating HEAs using HPT have also been observed [29, 30].

In addition to the studies described above, HPT has been employed to investigate the forced formation of supersaturated solid solutions in immiscible systems, which has attracted considerable attention due to the potential for discovering novel materials with enhanced properties [31, 32]. The prospect of the forced formation of solid solutions in immiscible systems using HPT also raises an important question regarding the efficacy of HPT in eliminating elemental segregation and achieving chemical homogeneity in RHEAs.

These diverse applications and novel findings underscore HPT's potential in advancing the study of HEAs and uncovering new aspects of their physical properties. As such, HPT is employed in the present work.

1.3 Element selection and phase formation prediction

Given that HEAs can comprise almost all metallic elements, the combinations in which they can be arranged are almost limitless. In order to select a target chemical composition, it is necessary to rely on specific empirical phase formation rules, which are based on thermodynamic fundamentals. For an easier understanding, this section starts with an introduction to these rules and relevant thermodynamic parameters. Subsequently, it examines these parameters associated with the composition in the present work and assesses their alignment with the rules.

1.3.1 Empirical phase formation rules for high-entropy alloys

The Hume-Rothery rule is a well-known empirical rule for predicting the formation of solid solutions. This rule suggests that the formation of a solid solution is favored by four factors: similar atomic sizes, crystal structures, electronegativities, and valencies [33]. However, this rule is specified when the concentration of the solvent atom is much higher than that of the solute atom. For HEAs, in which no distinct primary alloying element

is present, several extended Hume-Rothery rules have been developed [34–37]. Those rules are proposed in combination with thermodynamic parameters.
In a heterogeneous system, the Gibbs free energy of mixing ΔG_{mix} at a given temperature T can be expressed as:

$$\Delta G_{\mathrm{mix}} = \Delta H_{\mathrm{mix}} - T\Delta S_{\mathrm{mix}}, \tag{1.1}$$

where ΔS_{mix} and ΔH_{mix} are the mixing entropy and mixing enthalpy, respectively. Derived from the Boltzmann equation, the mixing entropy ΔS_{mix} of a completely random mixture of n components can be calculated as:

$$\Delta S_{\mathrm{mix}} = -R\sum_{i=1}^{n} c_i \ln c_i, \tag{1.2}$$

where c_i is the atomic fraction of the i-th component and R is the gas constant.
When discussing HEAs, the first consideration that comes to mind is the need for a high mixing entropy. As the positive mixing enthalpy ΔH_{mix} potentially leads to a miscibility gap, a high mixing entropy could counteract this effect. The mixing entropy is the largest when the atomic fractions are the same, and the magnitude of this largest value increases with the number of components n. However, experimental results show that a higher entropy is not necessarily better, as it signifies the presence of more elements and, consequently, more atomic interactions [2]. Empirical observations suggest that ΔS_{mix} should be in a suitable range, but further researches reveal that this condition alone is also insufficient [34].
For this reason, Zhang et al. introduced two more factors in addition to ΔS_{mix} in their empirical rule for predicting phase formation in HEAs: the mixing entropy ΔH_{mix} and the factor of atomic size mismatch δ [34]. The mixing enthalpy in multi-component systems can be expressed as follows:

$$\Delta H_{\mathrm{mix}} = \sum_{i=1, i\neq j}^{n} 4\Delta H_{ij} c_i c_j, \tag{1.3}$$

where n is the number of components in the system, and c_i and c_j are the molar fractions of elements i and j, respectively. The values of ΔH_{ij} are the mixing enthalpies of binary liquid alloys at equimolar composition, which are calculated using Miedema's model and can be found in [38]. The multiplier "4" compensates for the product of $c_i c_j$, which is $\frac{1}{4}$ in an equimolar binary system [39].

The atomic size mismatch δ can be written as:

$$\delta = \sqrt{\sum_{i=1}^{n} c_i \left(1 - \frac{r_i}{\bar{r}}\right)^2} \times 100\,\%, \tag{1.4}$$

where r_i is the atomic radius of the i-th element and $\bar{r} = \sum_{i=1}^{n} c_i r_i$ is the average atomic radius. According to Zhang et al., a single-phase solid solution is predicted when the three parameters meet the requirement simultaneously: $\delta < 6.5\,\%$, $12 \leq \Delta S_{\mathrm{mix}} \leq 17.5\,\mathrm{J/(K{\cdot}mol)}$ and $-15 \leq \Delta H_{\mathrm{mix}} \leq 5\,\mathrm{kJ/mol}$ [34].

Based on the work of Zhang et al., Yang and Zhang proposed a more refined rule by introducing another factor Ω [35]:

$$\Omega = \frac{T_{\mathrm{m}} \Delta S_{\mathrm{mix}}}{|\Delta H_{\mathrm{mix}}|}, \tag{1.5}$$

where the average melting temperature T_{m} is calculated as the weighted average of the melting temperature of each element $T_{\mathrm{m},\,i}$:

$$T_{\mathrm{m}} = \sum_{i=1}^{n} c_i T_{\mathrm{m},\,i}. \tag{1.6}$$

Although T_{m} provides an approximate estimation of the actual melting temperature, Ω still indicates the dominance of the entropy effect over that of enthalpy during solidification, as a positive mixing enthalpy leads to a miscibility gap. According to Yang and Zhang, $\Omega \geq 1.1$ and $\delta \leq 6.6\,\%$ should be satisfied simultaneously.

A similar statistical analysis conducted by Guo and Liu [36] suggested that solid solution forms when $\delta \leq 8.5\,\%$, $11 \leq \Delta S_{\mathrm{mix}} \leq 19.5\ \mathrm{J/(K{\cdot}mol)}$ and $-22 \leq \Delta H_{\mathrm{mix}} \leq 7\ \mathrm{kJ/mol}$. It is also found that the Pauling electronegativity difference does not play a significant role in predicting phase formation.

Poletti and Battezzati introduced their criteria with additional considerations on electronic and thermodynamic factors [37]. Instead of the conventional Pauling-electronegativity χ_{Pauling}, they utilized a relatively new variable χ_{Allen} defined by Allen, see [40]. The electronegativity mismatch factor can be written as follows:

$$\Delta\chi_{\mathrm{Allen}} = \sum_{i=1}^{n} c_i \left(1 - \frac{\chi_i}{\bar{\chi}}\right) \times 100\,\%, \tag{1.7}$$

where $\bar{\chi} = \sum_{i=1}^{n} c_i \chi_i$ is the average Allen-electronegativity. In their thermodynamic approach, a new parameter μ is defined:

$$\mu = \frac{T_\mathrm{m}}{T_\mathrm{SC}}, \tag{1.8}$$

where T_SC is the critical temperature at which the alloy composition aligns with the spinodal point. For an equimolar binary system, a conceptual illustration of this principle is shown in Fig. 1.3. T_SC is utilized as an estimation of the critical temperature for the

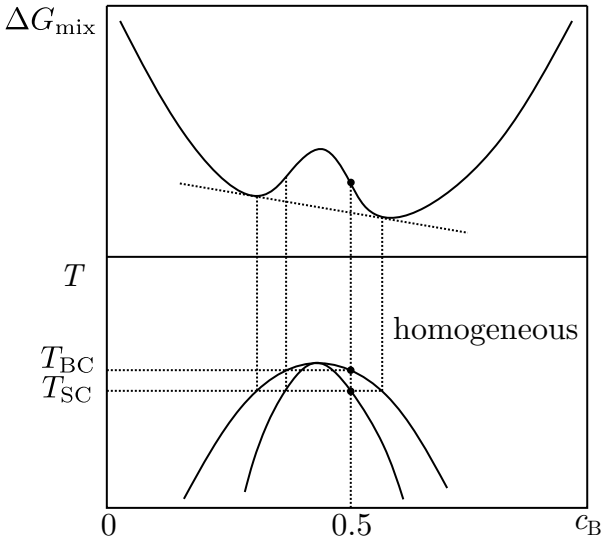

Fig. 1.3: Conceptual illustration of the spinodal point T_SC utilized in the estimate of the binodal point T_BC within an equimolar binary system A-B.

binodal point T_BC, above which the system is homogeneous. The parameter μ is similar to Ω, as a large value of μ indicates that a homogeneous solution is stable at a significantly lower temperature than the melting point T_m. At the spinodal point

$$\frac{\partial^2 \Delta G_\mathrm{mix}}{\partial^2 c_\mathrm{B}} = 0. \tag{1.9}$$

Poletti and Battezzati generalized this principle to multi-component systems by determining the critical temperature T_SC at which the determinant of the Hessian matrix H is zero. The Hessian matrix is defined as follows [37]:

$$H(T, c_i, \ldots c_{n-1}) = \begin{bmatrix} G_{ii} & \ldots & G_{i,n-1} \\ \vdots & \ddots & \vdots \\ \vdots & \ldots & G_{n-1,n-1} \end{bmatrix}, \tag{1.10}$$

where G_{ii} and G_{ij} represent the second partial derivatives of ΔG_{mix} of the n components, respectively:

$$\begin{aligned} G_{ii} &= \frac{\partial^2 \Delta G_{\text{mix}}}{\partial^2 c_i} = RT\left(\frac{1}{c_i} + \frac{1}{(1-\sum_i^{n-1} c_i)}\right) - 8\Delta H_{in}, \\ G_{ij} &= \frac{\partial^2 \Delta G_{\text{mix}}}{\partial c_i \partial c_j} = RT\left(\frac{1}{(1-\sum_i^{n-1} c_i)}\right) + 4(\Delta H_{ij} - \Delta H_{in} - \Delta H_{jn}). \end{aligned} \tag{1.11}$$

The contribution from G_{in} is disregarded since $\sum_{i=1}^{n} c_i = 1$, and the chemical potential of the n-th component is dependent on that of the other $n-1$ components, according to the Gibbs-Duhem equation. Poletti and Battezzati suggested that a single-phase solid solution would form when $3\,\% < \Delta\chi_{\text{Allen}} < 6\,\%$, $\delta < 6\,\%$, $\mu > 1.5$ [37].
The empirical rules described in this section are summarized in Tab. 1.1.

Tab. 1.1: Summary of the empirical phase formation rules.

Source	Criterion for single-phase solid solution
[34]	$12 \leq \Delta S_{\text{mix}} \leq 17.5$ J/(K·mol)
	$-15 \leq \Delta H_{\text{mix}} \leq 5$ kJ/mol
	$\delta < 6.5\,\%$
[35]	$\Omega \geq 1.1$
	$\delta \leq 6.6\,\%$
[36]	$11 \leq \Delta S_{\text{mix}} \leq 19.5$ J/(K·mol)
	$-22 \leq \Delta H_{\text{mix}} \leq 7$ kJ/mol
	$\delta \leq 8.5\,\%$
[37]	$3\,\% < \Delta\chi_{\text{Allen}} < 6\,\%$
	$\delta < 6\,\%$
	$\mu > 1.5$

1.3.2 Element selection

The rules described earlier clearly suggest selecting elements with similar physical and chemical properties to avoid intermetallics formation and to obtain a single-phase solid solution. This suggestion is associated with selecting elements adjacent to each other in the periodic table. In addition, the "cocktail effect" concept in HEAs indicates a synergistic mixture where the final outcome could be greater than the simple sum of the individual components [41].
Fig. 1.4 displays a portion of the periodic table that includes such elements. As previously mentioned, limitations in using Ni-base alloys at temperatures above 800 °C are attributed to their low melting temperature. To address this issue, Mo, Nb, and

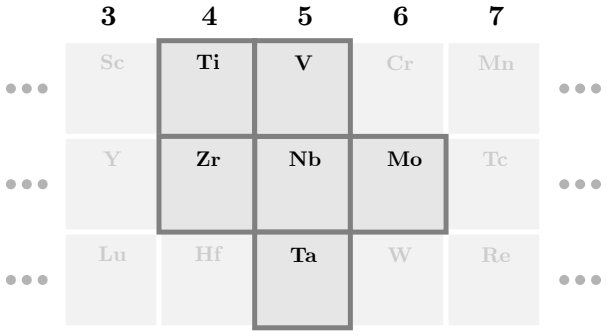

Fig. 1.4: The selected elements in the periodic table.

Ta, which have high melting temperatures, are selected for this study. Ti-base alloys are widely recognized for their excellent mechanical properties and low density, making them popular in the aerospace industry. For this reason, Ti is included in the study. Additionally, V and Zr are selected due to their significantly different atomic radii (see Tab. 1.2), which could lead to considerable lattice distortion and potentially enhanced mechanical properties. The effect of V and Zr has also been proved in literature [42, 43]. As a result, the chemical composition MoNbTaTiVZr is selected.
The physical properties of the six pure elements in the alloy are summarized in Tab. 1.2. Based on these properties, the thermodynamic parameters for the RHEA MoNbTaTiVZr can be calculated, as listed in Tab. 1.3.

Tab. 1.2: Physical properties of the pure elements in the senary RHEA MoNbTaTiVZr.

	Mo	Nb	Ta	Ti	V	Zr
$T_{\mathrm{m,A}}$ (K) [44]	2895	2750	3293	1946	2202	2128
ρ_{A} (g/cm^3) [44]	10.22	8.58	16.66	4.51	6.09	6.51
M_{A} (g/mol) [45]	95.951	92.906	180.947	47.867	50.942	91.224
r_{A} (Å) [44]	1.40	1.47	1.47	1.46	1.35	1.60
$\chi_{\mathrm{Allen,A}}$ [40]	1.47	1.41	1.34	1.38	1.53	1.32

Tab. 1.3: Calculated parameters of the equimolar RHEA MoNbTaTiVZr.

ΔS_{mix}	ΔH_{mix}	Ω	δ	$\Delta\chi_{\mathrm{Allen}}$	T_{m}	T_{SC}	μ
J/(K·mol)	kJ/mol	-	%	%	K	K	-
14.897	-2.111	17.892	5.27	7.29	2535.7	579.5	4.38

Upon evaluating these parameters, it appears that the RHEA MoNbTaTiVZr conforms to all the conditions for single-phase formation, except for the electronegativity mismatch factor $\Delta\chi_{\mathrm{Allen}}$. The alloy under consideration exhibits a value of 7.29 %, exceeding the range from zero to 6 %. While the most considerable contribution of the mismatch

appears to result from the element V (8.5 % larger than the average), it is deliberately included due to the potential for lattice distortion. It should also be noted that the range of $\Delta\chi_{\text{Allen}}$ proposed in [37] for single-phase solid solution is a conservative estimation, covering the interval where intermetallics are absolutely absent. This interval could extend from 6 % to 8.5 % if considering the full spectrum of solid solution occurrences, thereby encompassing the value of 7.29 % for the present RHEA composition.
As such, the selected composition MoNbTaTiVZr is excepted to form a single-phase solid solution and exhibit outstanding mechanical properties at elevated temperatures.

1.4 Outline of the work

This dissertation consists of three sections for investigating the RHEA MoNbTaTiVZr, including its microstructure, mechanical properties, and HPT processing. Before diving into the results and discussion, Chapter 2 provides a brief overview of the experimental and simulation methods employed, including sample preparation, characterization, and relevant thermodynamic simulation procedures.
The subsequent three chapters focus on the results and associated discussions. A conceptual diagram outlining the structure is shown in Fig. 1.5.

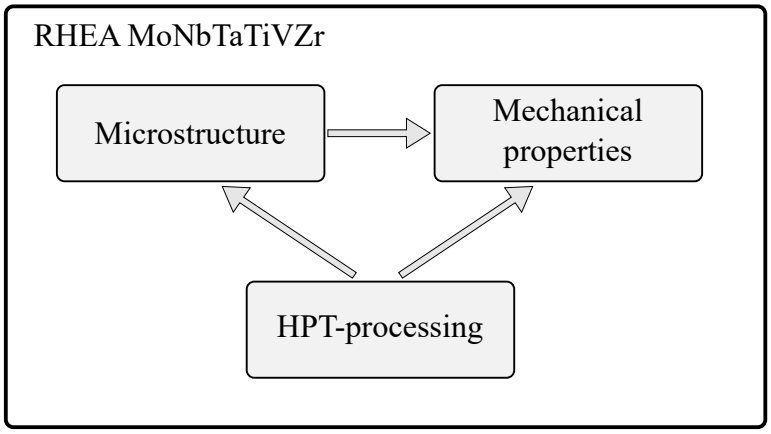

Fig. 1.5: Conceptional diagram for the present dissertation.

The section on results and discussion begins with an exploration of the microstructure in Chapter 3, followed by an investigation of the mechanical properties in Chapter 4. The aim is to understand the correlation between these two facets comprehensively. This examination of the initial state prior to HPT provides a foundation for comprehending the evolution of the microstructure and mechanical properties during the HPT, which is the focus of Chapter 5. As the dissertation exhibits a progressive structure, each chapter is wrapped up with a concise summary.

Finally, Chapter 6 presents the conclusions drawn from this dissertation, along with potential directions for future research.

Chapter 2

Experimental and simulation procedures

This chapter details the equipment and methodologies employed for the fabrication and characterization of materials in the present dissertation. It also briefly introduces the principles of thermodynamic simulation, including both equilibrium and non-equilibrium models.

2.1 Sample preparation

This section presents the basic construction of the arc furnace used in this study, along with the characteristics of a representative ingot produced using this method. Additionally, it provides an overview of the sample preparation for HPT and the parameters involved in this technique. Furthermore, a concise list of the heat treatment apparatuses and their respective advantages and disadvantages are included.

2.1.1 Vacuum arc melting

Most of the RHEAs are fabricated using the vacuum arc melting method. This method is also utilized in this dissertation.

The process is conducted using the compact furnace MAM-1 (Edmund Bühler GmbH, Bodelshausen, Germany). An overview of the furnace is shown in Fig. 2.1a. The furnace's melting chamber exhibits a modest capacity of about five liters, facilitating evacuation. Before the melting procedure, this chamber is evacuated and backfilled with high-purity Ar (99.999 %) five times. Pure raw materials in different forms (wire, pellet, foils, powder, and granule), all with purity levels exceeding 99.5 %, are remelted on a

water-cooled copper hearth (see Fig. 2.1b). A Ti-getter is used to remove the remaining oxygen in the melting chamber. To ensure chemical homogeneity, the ingot is flipped using the manipulator and remelted at least ten times. During the last remelting process, the ingot is kept in the liquid state for about two minutes. A button-shaped ingot with dimensions of about $14 \times 14 \times 8\,\mathrm{mm}$, manufactured from the process described above, is shown in Fig. 2.1c.

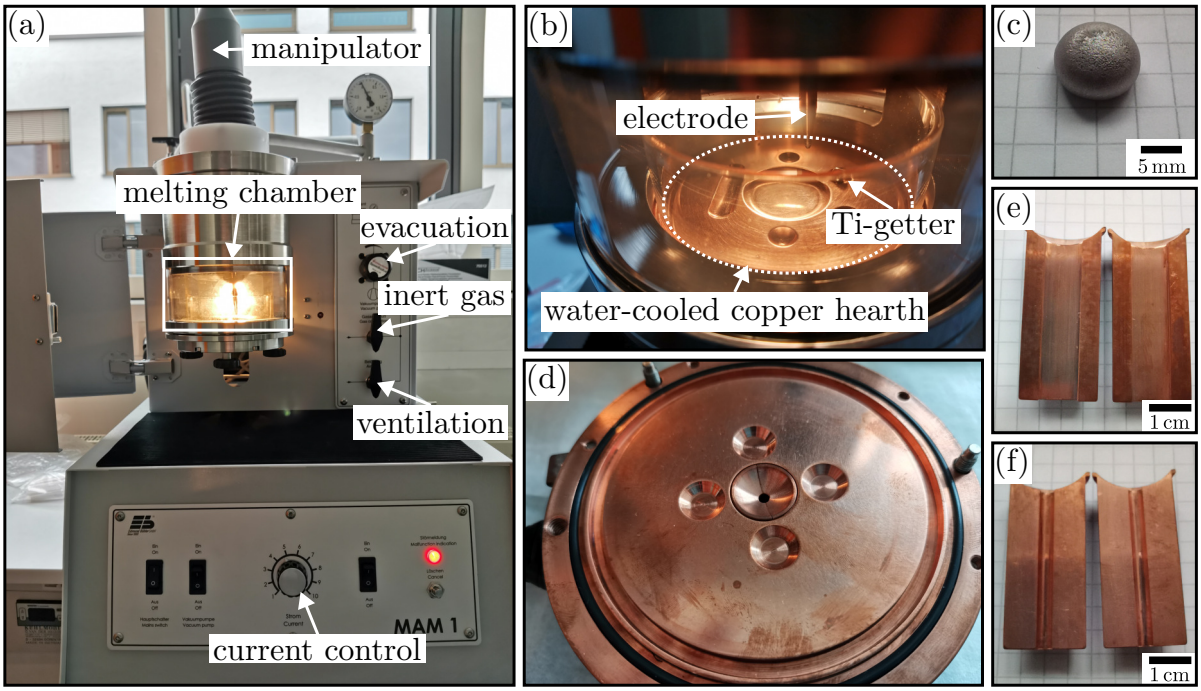

Fig. 2.1: (a) Overview of the vacuum arc melting furnace MAM-1 (Edmund Bühler GmbH). (b) The melting chamber. (c) A button-shaped ingot. (d) The copper hearth for suction casting. (e-f) Copper hearth and molds for suction casting.

The furnace is equipped with suction casting devices, such as the copper hearth and molds shown in Figs. 2.1d-f. However, in order to perform the suction casting, the sample needs to be heated to a much higher temperature than its melting point. Although the maximum temperature for melting in this furnace is about 3500 °C, the melt near the molds exhibits a much lower temperature due to the constantly cooled copper hearth. Through practice, it is found that only alloys with melting points below 1800 °C could be prepared using this method. Such a critical temperature is too low for the present RHEA, which possesses a melting point higher than 2000 °C (see Tab. 1.3). Hence, the as-cast samples in this work are all initially button-shaped ingots.

It should be noted that the ingot exhibits a slight inhomogeneity in the direction perpendicular to the copper hearth. An examination of the cross section of the ingot is performed using the optical microscopy (OM), as described in Sec. 2.2.2. Fig. 2.2a

shows the cross section A-A of an ingot, with enlarged representations of the top and bottom shown in Figs. 2.2b and 2.2c, respectively. For easier clarification, corresponding schematic illustrations and descriptive texts are included alongside the OM images in the subfigures.

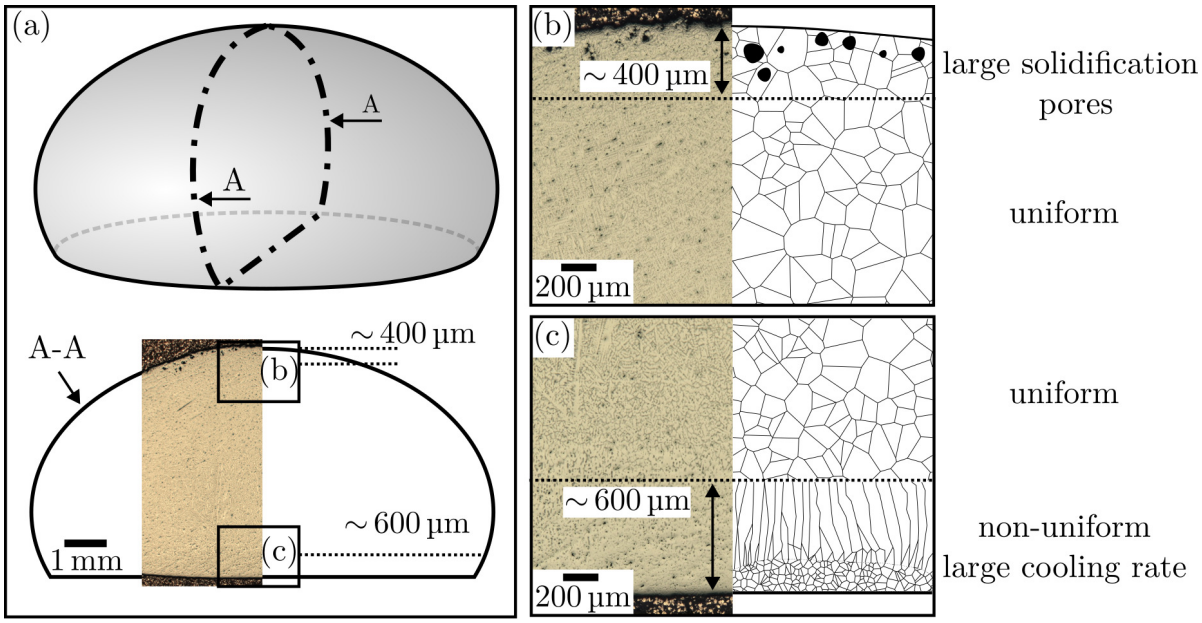

Fig. 2.2: Inhomogeneity in the button-shaped ingot. (a) Schematic representation of the ingot, with the cross-section A-A partially overlaid with optical microscopy (OM) images. Detailed views of the top (b) and bottom (c) of the ingot, showing enlarged OM images along with schematic illustrations of the grain structure.

The observed inhomogeneity can be explained by referring to the fundamentals of heat transfer and physical metallurgy. Due to its direct contact with the water-cooled copper hearth, the bottom of the ingot is subject to the fastest cooling during solidification, leading to substantial melt undercooling. This results in an extensive grain nucleation and the formation of the smallest grain size at the bottom part. The primary mode of heat transfer in this part is thermal conduction. At about 200 µm from the bottom, columnar crystals start to form as the cooling rate decreases with increasing distance from the copper crucible. This decrease of cooling rate is attributed to the relatively lower thermal conductivity of the ingot compared to the copper hearth. From approximately 600 µm above the bottom, convection and radiation play a more significant role in cooling, as the melting chamber's atmosphere and environment also contribute to the cooling. The cooling rate thus exhibits minor variation from about 600 µm to the top of the ingot, leading to a nearly uniform grain nucleation rate in this region. Consequently, a large, predominantly region with uniform grain size forms in the central portion of the ingot, as marked with "uniform" right to Figs. 2.2b-c. Solidification also induces a volume

shrinkage in the melt, leading to pores forming within the ingot. These pores primarily accumulate at the top of the ingot due to the gravitational effect. As shown in Fig. 2.2b, the region containing large solidification pores is about 400 µm thick.

In practice, the inhomogeneous region at the bottom of the ingot could be minimized by optimizing the cooling procedure, such as gradually reducing the arc's current. The thickness of the region containing pores at the top could be reduced by setting an optimal pressure of the Ar atmosphere. Note that the grain distribution in Figs. 2.2b-c is generated by Voronoi-tessellation. To visually emphasize the inhomogeneity, the grains are magnified and may not accurately represent the actual condition.

Due to the ingot's limited geometry, different cutting strategies are proposed to maintain sample consistency in subsequent experiments, see Fig. 2.3. These strategies are designed to ensure that synchrotron high-energy X-ray diffraction (HEXRD), compression testing, and HPT are performed only in the homogeneous regions of the sample.

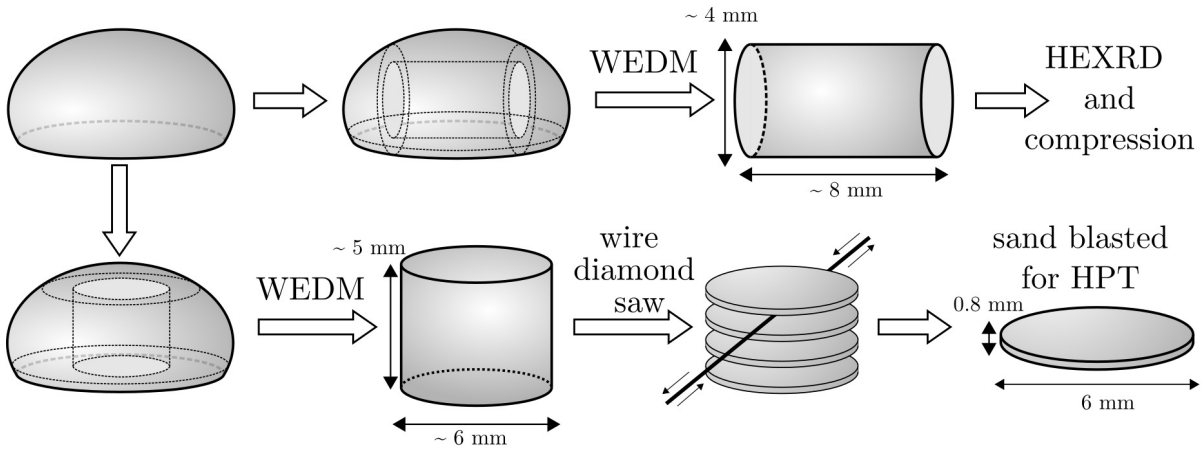

Fig. 2.3: Flow chart of the sample preparation for subsequent experiments.

For HEXRD and compression testing, the ingot is sectioned horizontally into cylinders with dimensions of approximately 4 mm in diameter and 8 mm in height using the wire electrical discharge machining (WEDM). For HPT samples, the ingot is firstly cut into a cylinder of about 6 mm in diameter and 5 mm in height using WEDM. Subsequently, this cylinder is sliced into disks with a radius of 6 mm, and a thickness of 0.8 mm using a wire diamond saw.

2.1.2 High-pressure torsion

The HPT experiments are carried out at the Erich Schmid Institute of Materials Science (ESI) in Austria.

Prior to the HPT, the disks are sandblasted to obtain greater friction and thus avoid slippage during the twisting. The disks are subjected to HPT in a conventional Bridgman-apparatus (see Fig. 1.2) under a quasi-hydrostatic pressure of 7 GPa, and subsequently undergo varied numbers of revolution N: 0.25, 2, 4, 10, 20, 30, 40. The samples after HPT are denoted as $N0.25$, $N2$, $N4$, $N10$, N20, $N30$ and $N40$, respectively. A processing rate of 0.2 revolutions per minute is selected to prevent excessive heat generation. To allow for the required shear strain, the cavity of the HPT anvils (0.6 mm) is smaller than the initial thickness of disks (0.8 mm). However, this height difference, combined with the high compression pressure, suggests that the untwisted sample also undergoes deformation during compression. Hence, a disk that is merely compressed and not twisted, denoted as $N0$ or as-compressed, is utilized for comparison.
A schematic illustration of a sectioned HPT-disk, prepared for detailed characterization, is shown in Fig. 2.4. Three directions are defined to simplify the positioning of the surface during characterization: axial, radial, and tangential directions.

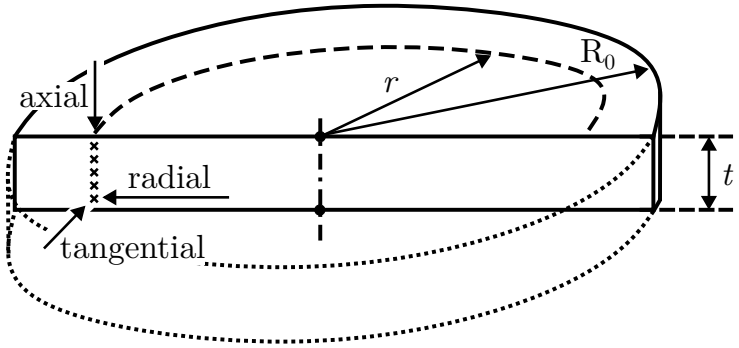

Fig. 2.4: A sketch showing the sectioned HPT-disk used for characterization.

Fundamentals of solid mechanics indicate that deformation along the radial direction during torsion straining is inhomogeneous. Considering a twisted rod with a length of l, the shear strain γ at the position r of its cross section can be described as:

$$\gamma = \frac{r\phi}{l}, \tag{2.1}$$

where ϕ is the turn angle in radians. Assuming a pure torsion in HPT, ϕ becomes $2\pi N$ when an HPT-disk undergoes N revolutions. Then Eq. 2.1 is adapted as:

$$\gamma = \frac{2\pi N r}{t},\ 0 \leq r \leq \mathrm{R}_0, \tag{2.2}$$

where R_0 and t are the disk's radius and thickness, respectively. For facilitating a comparison between HPT and other plastic deformation processes, the von Mises equivalent

strain ε is employed. Following the von Mises flow criterion, ε is obtained by dividing γ by $\sqrt{3}$ [22]:

$$\varepsilon = \frac{\gamma}{\sqrt{3}} = \frac{2\pi N r}{\sqrt{3}\,t},\ 0 \leq r \leq \mathrm{R}_0. \tag{2.3}$$

For consistency in this work, the equivalent strain ε is used to describe the applied strain by HPT. In practice, it should be noted that uncertainties in sample dimensions are frequently observed, such as imprecise r values resulting from grinding and polishing during metallographic preparation and variations of t along the radius. Furthermore, a reduction of thickness can be found after a large number of revolutions in HPT, even though the quasi-constrained geometry is employed in the current dissertation. Hence, the strain values for HPT are shown as approximate values along with "$\sim$". While R_0 is a fixed value of 3 mm, the thicknesses of the HPT-disks in this work after HPT are listed in Tab. 2.1.

Tab. 2.1: The mean thickness of HPT-disks after processing t (in mm).

	$N0$	$N0.25$	$N2$	$N4$	$N10$	$N20$	$N30$	$N40$
t (mm)	0.615	0.605	0.601	0.595	0.591	0.581	0.575	0.55

2.1.3 Heat treatment apparatuses

Vacuum furnace

A vacuum inert gas furnace (MAYTEC GmbH, Singen, Germany) is employed for heat treatment, with a curved MoW plate serving as the heat radiator. Temperature is measured using a W/Re-alloy thermocouple (type C) with the furnace capable of operating within a temperature range of 400 to 2000 °C. Before heat treatment, the furnace chamber undergoes a cycle of evacuation to about 2 Pa and backfilling with Ar, which is repeated three times. Samples are placed in a ZrO_2 crucible during heat treatment. A Zr-getter is positioned in another crucible to circumvent potential oxidation due to inadequate vacuum quality.

It should be noted that quenching is very difficult in this vacuum furnace. Therefore, in the present dissertation, samples specified as heat treated using vacuum furnace are all furnace cooled.

Quenching dilatometer

In addition to the vacuum inert gas furnace, a dilatometer DIL805 (TA Instruments, New Castle, USA) is used for heat treatment. The instrument can be operated in three modes, Quench (A), Compression (D), and Tensile (T), depending on the test conditions required. Within the scope of this dissertation, both quenching and compression modes are utilized. Details about the compression mode in relation to mechanical properties will be described in Section 2.3.3.

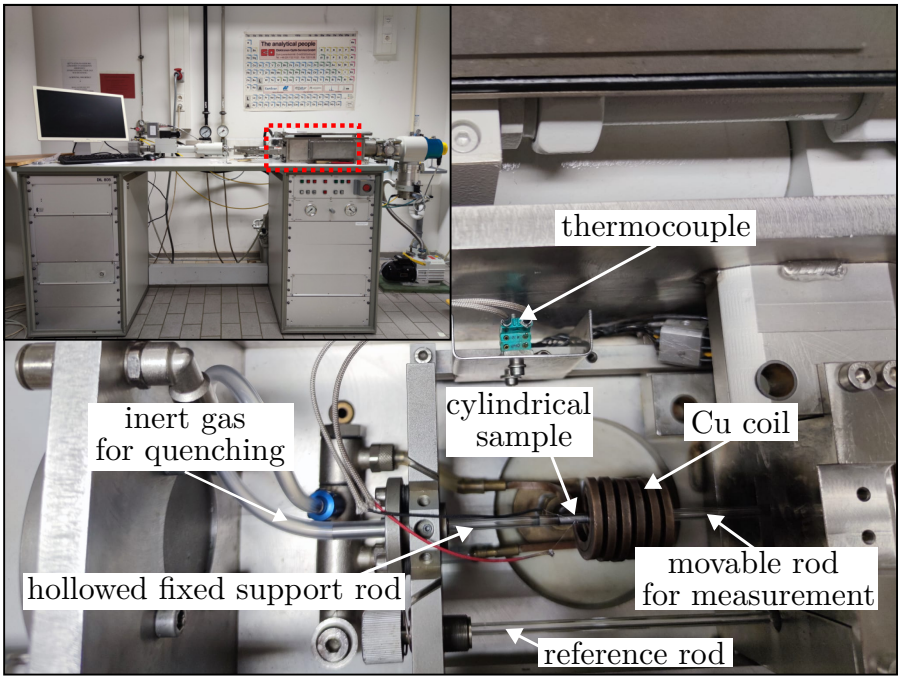

Fig. 2.5: Setup of the dilatometer DIL805 operated in quenching mode. The inset shows an overview of the instrument.

Fig. 2.5 shows the setup of the dilatometer operated in quenching mode (DIL805A). A cylindrical sample, with a maximum length of 10 mm, is placed between two quartz glass rods and held by a slight spring force. The fixed hollow rod on one side is linked with the cooling nitrogen gas, while the movable solid rod on the other side is connected to a displacement transducer. The sample's temperature is measured using a Pt/Rh thermocouple (type S) welded to the sample surface. The displacement and temperature resolutions in the dilatometer are 0.05 µm and 0.05 K, respectively.
The dilatometer is equipped with a turbomolecular pump and exhibits a better vacuum quality (5×10^{-2} Pa) than in the vacuum furnace. While quenching is feasible in the dilatometer, the maximum operating temperature for a heat treatment exceeding 2 hours is limited to 1200 °C. This is due to a recurring issue where the welded thermocouple breaks under such conditions in practice.

2.2 Microstructure characterization

The microstructure characterization involves the analysis of phase composition and microscopy. Phase composition is studied using X-ray diffraction, utilizing different beam sources, including conventional CuKα and synchrotron high energy X-ray sources. For microscopy investigations, a range of techniques, such as light optical, scanning electron, and transmission electron microscopy, are employed.

2.2.1 Phase composition analysis

The varied beam sources exhibit different wavelengths λ. For easier comparison, the diffraction intensity is plotted against the magnitude of the wave vector Q:

$$Q = \frac{4\pi \sin\theta}{\lambda}, \tag{2.4}$$

instead of the diffraction angle θ.

Laboratory X-ray diffraction

Laboratory XRD is carried out with a Bruker diffractometer D8 with Bragg-Brentano geometry (reflective). Cu is used as a target material hit by electrons accelerated at 30 kV to obtain the X-rays with a wavelength of 1.5406 Å.

Synchrotron high-energy XRD

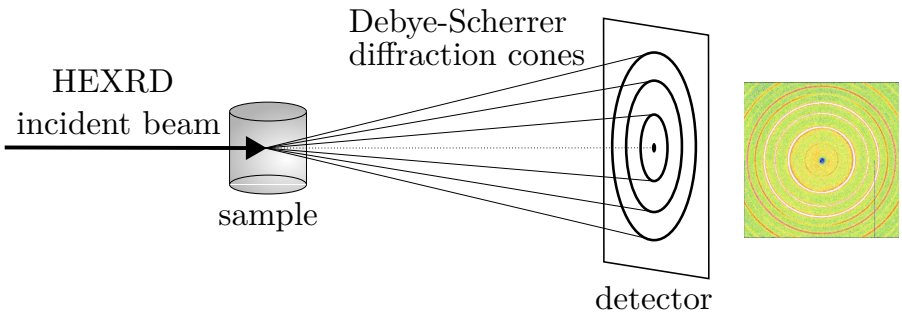

Fig. 2.6: The synchrotron high-energy XRD (HEXRD) experiment and an example of a two-dimensional pattern obtained from HEXRD.

HEXRD experiments are conducted at the High Energy Materials Science (HEMS) beamline at PETRA III at DESY in Hamburg, Germany. The diffraction test is carried out in transmission mode (Fig. 2.6) with two beams having different wavelengths λ (0.124 Å and 0.14235 Å). The photon energies are about 100 keV and 87 keV, respectively. The

beam with a wavelength of 0.14235 Å contains about 10 % of a second wavelength due to the quality of the monochromator. The beam size is set as 0.7×0.7 mm using a slit aperture, and the diffracted beam is captured by a PerkinElmer XRD 1622 flat panel detector positioned about 1400 mm away from the sample. The measurement is calibrated using a standard LaB_6 powder (NIST SRM 660a). The two-dimensional results are integrated into diffractograms using the software Fit2D [46].

Rietveld refinement

The Rietveld refinement of diffractograms obtained from HEXRD is performed in the software MAUD [47]. This work does not focus on the texture and residual stress in the sample. Therefore, a simplified material model is used, which accounts for a uniform distribution of strain and coherent scattering size.
The material information for each phase in the refinement requires initial values. The crystal structures and the approximate lattice constants of each phase are obtained by indexing the XRD/HEXRD spectra. The approximate chemical composition of the phases is acquired by the elemental analysis described in Section 2.2.2. As no peaks of ordered solid solutions are found in the XRD spectra, e.g. (100), it is assumed that the atoms of each element are equally distributed on the equivalent positions in the crystal. The initial strain and coherent scattering size are set to 6×10^{-4} and 1000 Å, respectively. The instrument broadening is obtained by fitting the diffractogram of the standard LaB_6, where both the size and the strain are set to 0, as described in [47].

2.2.2 Microscopy

In this work, optical and electron microscopes are employed for microscopic characterization. Except for focused ion beam and transmission electron microscopy, the samples are embedded and ground using SiC abrasive papers with grit sizes ranging from 320 to 1000. They are subsequently polished with 3 and 1 µm diamond suspensions, followed by an oxide polishing suspension with a grain size of 0.25 µm and a pH-value of about 9 - 10.

Light optical microscopy

Characterization using optical microscopy (OM) is performed with the reflecting light microscope Leitz Aristomet (Leica Microsystems GmbH, Wetzlar, Germany). The bright field and interference modes of imaging allow a high-contrast visualization of the microstructure.

Scanning electron microscopy

Two scanning electron microscopes are used, including JSM6490 and JSM7600F (JEOL ltd., Tokyo, Japan). The microscope JSM6490 utilizes a tungsten filament as an electron source and is equipped with a secondary electron (SE) detector, while the microscope JSM7600F works with a field emission electron source equipped with a backscattered electron (BSE) detector. The operation voltages for both microscopes are 20 kV.

Energy-dispersive X-ray spectroscopy

Both electron microscopes are equipped with energy-dispersive X-ray spectroscopy (EDS) detector systems. For consistency, the quantitative results of EDS in this work are acquired from the microscope JSM6490 equipped with INCA PentaFETx3 (Oxford Instruments plc, Abingdon, UK). The quantitative results are calibrated using a Cu-foil.

Electron backscattered diffraction

The electron backscatter diffraction (EBSD) results in this work are obtained from the microscope JSM7600F, which is equipped with an Oxford-SYMMETRY detector. The integrated advanced software system Aztech is used, which can analyze EBSD and EDS results simultaneously to separate phases with similar crystal structures. Since there are no standard files in the NIST-database for RHEAs, the HKL-diffraction data is generated by the software TWIST. The assumptions on material information during generation are similar to that in the Rietveld refinement described in Section 2.2.1.

Transmission electron microscopy

In the present dissertation, only HPT-disks are characterized using transmission electron microscopy (TEM). TEM experiments and sample preparation are carried out at the Zentrum für Grenzflächendominierte Höchstleistungswerkstoffe in Bochum.

The TEM investigations are performed using a JEM-ARM200F microscope (JEOL ltd., Tokyo, Japan) operated at an acceleration voltage of 200 kV. Samples are prepared using the focused ion beam (FIB) method in an FEI Helios G4 CX at 30 kV. Specimens of dimensions 8×8×1 µm are extracted from the HPT-disks in the radial direction through Ga^+ ion milling. A 3 µm thick carbon protective layer is deposited prior to thinning. To minimize beam damage during the final stage, the acceleration voltage is reduced to 8 kV. A sketch illustrating the TEM specimen prepared by FIB is shown in Fig. 2.7.

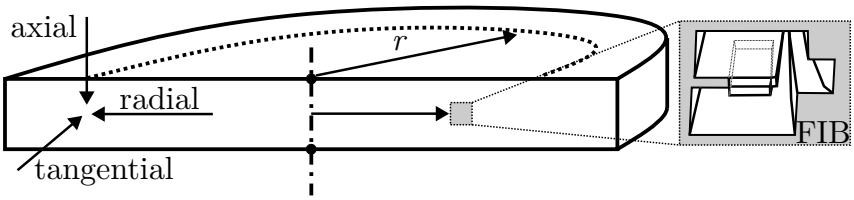

Fig. 2.7: A sketch illustrating the TEM specimen prepared by FIB, after [48].

2.3 Mechanical properties

The characterization of mechanical properties involves the evaluation of microhardness under different test conditions and analyzing material behavior under compression tests conducted at varied temperatures. Two methods are used for microhardness testing, distinguished by the specific equipment and the applied indentation loads: conventional microhardness tests and ultra-microhardness (UMH) measurements.
In this dissertation, UMH tests are specifically employed to probe local hardness. Unless explicitly stated, the term "microhardness" is generally used to refer to results from conventional microhardness tests.

2.3.1 Microhardness

Conventional microhardness tests are conducted using a micro-DUROMAT 4000E tester (Reichert-Jung Inc., Buffalo, USA) with an applied load of 100 g and a dwell time of 10 s. The tester employs a standard Vickers-pyramid indenter, characterized by a square pyramid with opposite faces at an angle of 136°. The Vickers microhardness (HV) value H can be calculated using the following formula [49]:

$$H = \frac{2P}{D^2}\sin\frac{136^\circ}{2} = 1.86\frac{P}{D^2}, \tag{2.5}$$

where P represents the indentation force in kilograms, and D is the average diagonal length of the indentation impression in millimeters. The reported values are obtained by averaging the results of five indents from the polished surface. For consistency, all microhardness measurements in this work are conducted under the same condition.

2.3.2 Ultra-microhardness

UMH measurements are carried out using a UMHT-1 tester (Kammrath & Weiss GmbH, Schwerte, Germany) built into the microscope JSM6490. Similar to conventional microhardness tests, the UMHT-1's indenter also employs a standard Vickers-pyramid geom-

etry. The tests are conducted with an applied load of about 2×10^{-3} g, a dwell time of 10 s, and a loading velocity of 0.25×10^{-3} g/s. The diagonal lengths of the indents are measured using the software ImageJ [50]. The UMH values are calculated similarly to conventional microhardness using Eq. 2.5. The reported UMH values are also the average of five test results.

2.3.3 Compression test

The quenching dilatometer (Fig. 2.5) can be rebuilt and converted to the compression mode, see Fig. 2.8. The maximum force that can be detected by the sensor used is 20 kN. The samples are cylinders with a diameter of 4 mm and a length of 8 mm cut by WEDM (see Fig.2.3). Before the compression test, the contact ends of samples are ground with 1000- and 2000-grit SiC abrasive paper to minimize their friction with Si_3N_4 stamps. Al_2O_3 rods are used for displacement measurement.

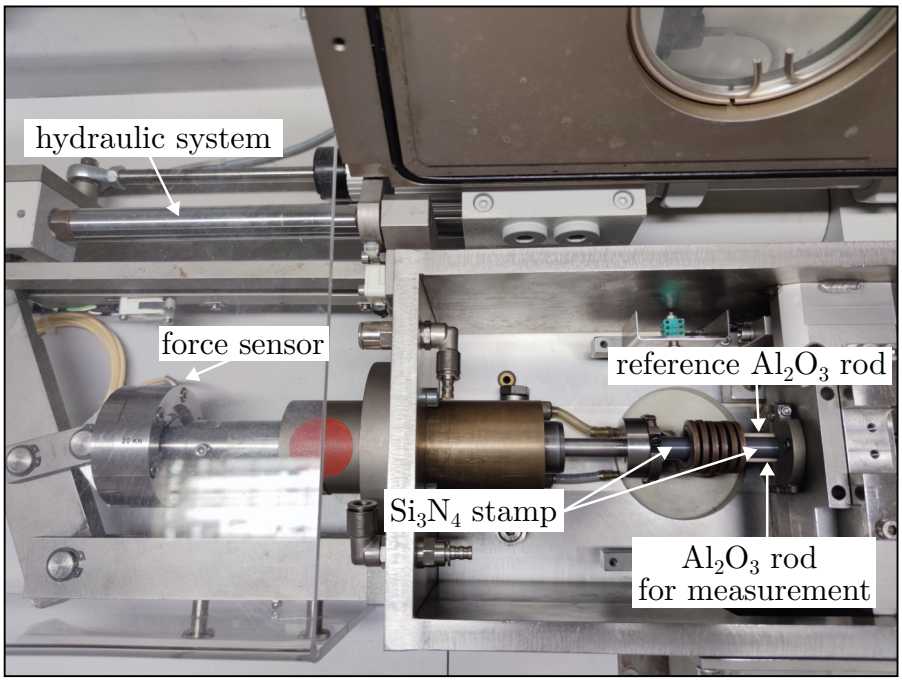

Fig. 2.8: Setup of the dilatometer DIL805 operated in compression mode.

The deformation dilatometer can be operated at both room temperature and elevated temperatures. For the compression at elevated temperatures, the samples are firstly heated to the desired temperature with a heating rate of 1 K/s and held at the desired temperature for 1 min. The compression test is displacement-controlled with a rate of 0.01 mm/s. The calculated strain rate is approximately 1.25×10^{-3}, thus making the test quasi-static. Same as in the quenching mode of the dilatometer, the minimum detectable

length and temperature variations in DIL805D are 0.05 µm and 0.05 K, respectively. The experimental procedure, as well as the analysis of the compressive stress-strain curve are planned to meet the standard DIN 50106.

2.4 Thermodynamic simulation

To describe the whole phase diagram of HEAs, conventional methods are inadequate as HEAs often comprise multiple principal elements. Consequently, n-dimensional graphs are required, which are difficult to depict. A commonly used approach by researchers to analyze the phase composition of HEAs at different temperatures is through the CALPHAD (CALculation of PHAse Diagrams)-method. The CALPHAD-method has been demonstrated to be an effective tool for predicting the phase formation of HEAs [6].
In the present study, the commercial software Thermo-Calc (2017a-version) is utilized along with the TCHEA1 database, which is specifically developed for HEAs [51]. This database is based on experimental data, theoretical values obtained from first-principles calculations, and binary and ternary system phase diagrams extrapolations. Consequently, it allows the calculation of thermodynamically stable phase constituents for a specific HEA composition at varying temperatures.
Additionally, the CALPHAD-method can simulate the solidification process. By means of this, the elemental composition in the solid (crystal) and liquid (melt) phases can be calculated, thus enabling an analysis of the segregation during solidification. Two different models, equilibrium-solidification and Scheil-solidification, can be employed for this purpose. To facilitate an understanding of the difference between these two models, a schematic illustration of them in a binary system is shown in Fig. 2.9. This illustration considers the solidification process of a melt with a concentration of c_0 solutes.
The equilibrium-solidification assumes that the solutes in both solid and liquid phases are in equilibrium, allowing sufficient time for atomic diffusion. The solute concentration in the melt follows the liquidus line from c_0 to c_2 until the end of solidification, while that in the solidified crystal proceeds from c_1 at the onset of solidification along the solidus line to c_0. Consequently, the chemical composition in the solid after solidification is homogeneous, exhibiting the same concentration as the melt before solidification.
On the other hand, the Scheil-solidification is based on the Scheil-Gulliver model [54, 55]. In this model, the diffusion in the solid phase is completely suppressed, and equilibrium is only established in the melt and at the solid-liquid interface. Therefore, a concentration gradient can be seen in the solid phase, as indicated by the red points on the right side of Fig. 2.9. At the same time, this leads to the enrichment of the solute in the melt, with its

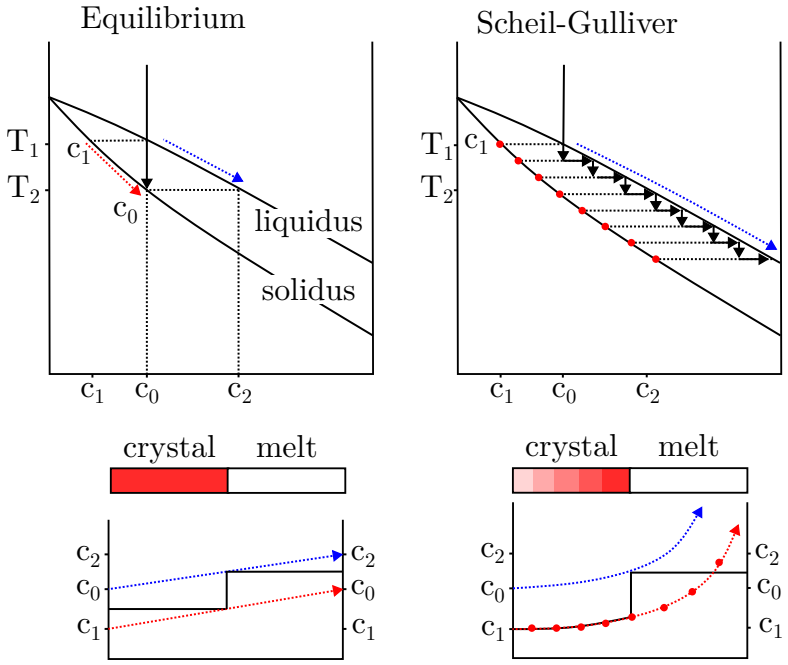

Fig. 2.9: Schematic illustration of the solidification path using equilibrium and Schei-Gulliver model. Adapted from [52, 53].

concentration evolving from c_0 along the liquidus line until it reaches the concentration of the pure solute. In a eutectic system, the melt concludes the enrichment at the eutectic point, resulting in eutectic solidification. It can also be noted that the Scheil-solidification exhibits a much longer solidification path than that in the equilibrium calculations.

Chapter 3

Microstructure

In this chapter, a thorough exploration of the microstructure of the RHEA MoNbTaTiVZr is conducted. The results set the foundation for understanding the mechanical properties discussed in Chapter 4, and they are also crucial for comprehending the initial state prior to the HPT processing, which is detailed in Chapter 5.
The chapter starts with a preliminary examination of the microstructure, where the discrepancies between the results of thermodynamic simulations and experimental outcomes are compared and discussed. Subsequently, the effect of the alloying element vanadium on the microstructure is systematically investigated. The effect is also studied in thermodynamic simulations, especially in solidification. The results of these simulations provide an explanation for the unexpected microstructure and phase composition observed in the RHEA. Thereafter, the microstructure of four subgroup alloys of the RHEA is investigated to gain more insights into the microsegregation in the RHEA.

3.1 Preliminary examination of microstructure

3.1.1 Equilibrium phase composition

The predicted phase composition of the equimolar RHEA MoNbTaTiVZr, calculated using ThermoCalc, is shown in Fig. 3.1. The solidification starts at 2175 °C, and the proportion of the liquid phase (black) reduces until 1658 °C. Followed by this, a single-phase structure (BCC1, red) is present down to 1103 °C, and the coexistence of two BCC microstructures (BCC1 and BCC2) is predicted until 527 °C, after which the Laves phase occurs. Additionally, a hexagonal close-packed (HCP) phase occurs at 493 °C. The BCC2 phase vanishes below 480 °C, resulting in the coexistence of three phases (BCC1, Laves, and HCP) at room temperature.

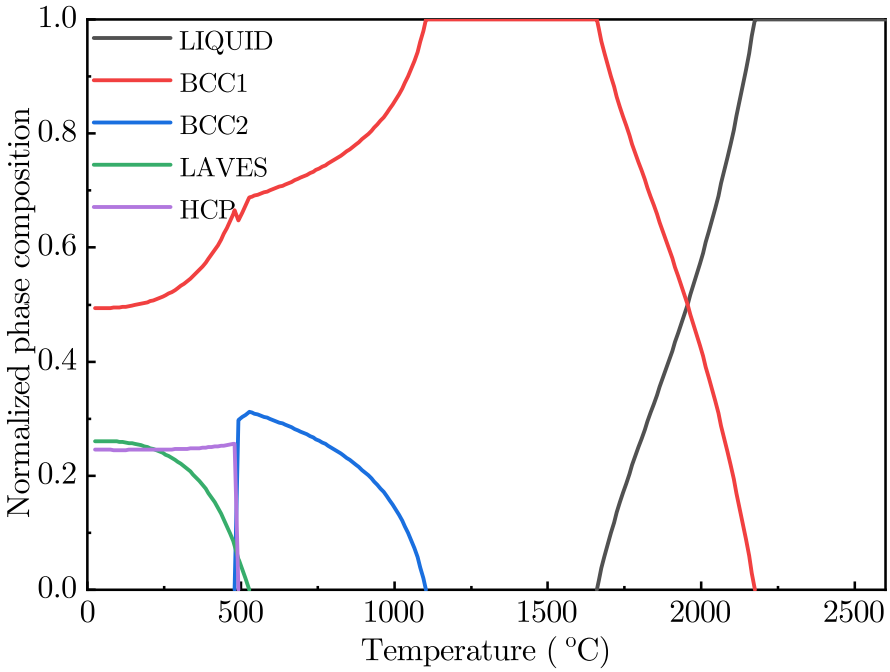

Fig. 3.1: Normalized equilibrium phase composition of RHEA MoNbTaTiVZr calculated via CALPHAD-method, after [56].

However, it should be noted that the phase composition prediction obtained using the CALPHAD-method represents the equilibrium state, which may be difficult to achieve in practice. HEAs fabricated using the arc-melting method experience a cooling rate of about 200 K/s, which deviates significantly from equilibrium [57]. Therefore, researchers typically focus on the high-temperature range of the predicted phase composition, corresponding to the non-equilibrium state. In fact, many researchers have presented merely the range above 600 °C for as-cast HEAs in their publications. Some researchers even predict the phase composition of their HEAs based solely on high-temperature data exceeding 1200 °C [58]. According to this strategy, it can be predicted that the present RHEA might exhibit either a single-phase BCC structure or a dual-phase BCC structure.

3.1.2 Experimental results

The SEM backscattered electron image and the HEXRD pattern of the as-cast RHEA are shown in Fig. 3.2a and b, respectively. The SEM micrograph reveals a dendritic microstructure with a minor region being interdendritic. A varied dendritic arm spacing of approximately 5 - 25 µm is observed. The HEXRD pattern shows a distinct set of peaks that can be indexed as the major BCC phase, as well as a secondary group of a minor BCC phase. The lattice constants of the major and minor BCC phases are 3.25 Å, and 3.47 Å, respectively. Based solely on the results of Fig. 3.2, it might be concluded

that the major BCC phase is identified as belonging to the dendritic region, while the secondary BCC phase to the interdendritic region. However, such an assumption leads to a volume fraction of the interdendritic region of about 14 % using Rietveld refinement, which is inconsistent with the result of about 35 % using the area calculation method. This discrepancy indicates the necessity for a further investigation to fully understand the phase composition.

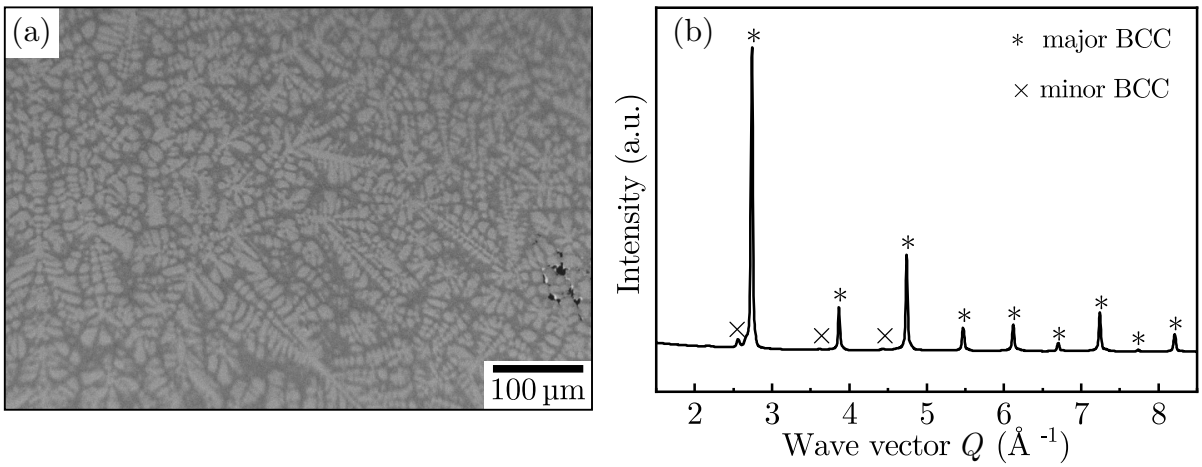

Fig. 3.2: (a) SEM backscattered electron image and (b) HEXRD pattern of RHEA MoNbTaTiVZr, partly after [56].

A specific region of the SEM micrograph is selected for analysis using EDS. The mapping results are shown in Fig. 3.3. The quantitative EDS results of the same region are listed in Tab. 3.1. The dendritic region of the alloy is enriched in Mo and Ta, while the interdendritic region displays enrichment in Nb, Ti, V and Zr. Zr exhibits the most significant microsegregation, leading to the dendritic region (8.8 %) being termed as Zr-depleted and the interdendritic region (43.8 %) as Zr-rich. However, within the Zr-rich interdendritic region, certain small areas exhibit a high concentration of V. A slight depletion of Zr near these areas is also observed. This phenomenon raises again an inquiry regarding the actual phase composition and identification in the HEXRD pattern.

Tab. 3.1: Quantitative EDS results (at. %) for the area shown in Fig. 3.3: D for dendritic, ID for interdendritic regions, and SUM for the entire area. Adapted from [48].

	Mo	Nb	Ta	Ti	V	Zr
D	21.1 ± 0.5	20.3 ± 0.1	21.3 ± 0.2	14.4 ± 0.2	14.3 ± 0.2	8.8 ± 0.2
ID	7.5 ± 2.2	12.2 ± 1.4	4.9 ± 1.5	17.6 ± 0.6	13.9 ± 1.8	43.8 ± 7.1
SUM	14.7 ± 0.1	14.9 ± 0.1	16.8 ± 0.1	17.8 ± <0.1	17.6 ± <0.1	18.2± 0.1

Apart from this, it should be noted that the mapping result of Nb is inconsistent with its quantitative EDS results. The dendritic region exhibits a higher Nb concentration

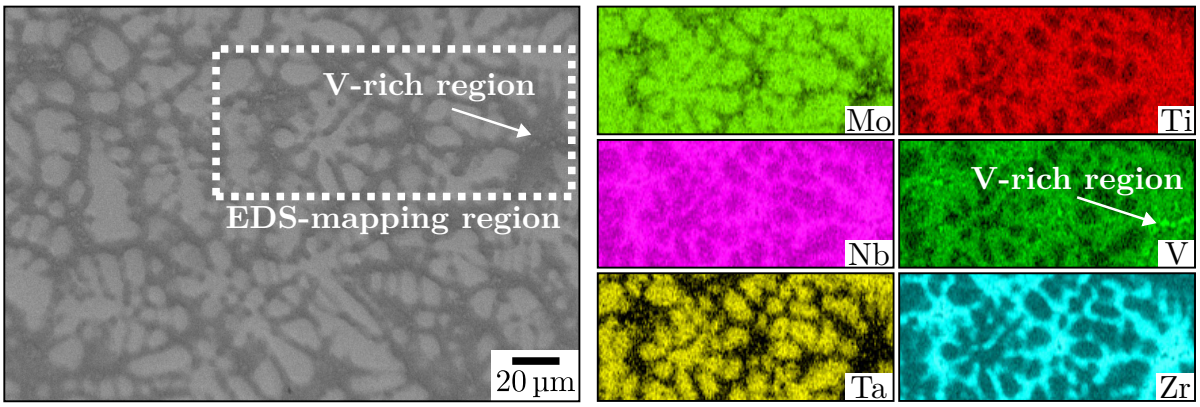

Fig. 3.3: SEM backscattered electron image used for EDS-mapping and the corresponding mapping results of RHEA MoNbTaTiVZr, after [56].

(20.3 %) than the interdendritic region (12.2 %). This discrepancy can be attributed to the mapping results being based on a single characteristic X-ray emission, while the quantitative results analyze the whole spectrum. The energies of the $L\alpha_1$ emission lines of Nb and Zr, which are used for mapping, are 2.042 and 2.166 keV, respectively [59]. The difference between them (124 eV) is slightly smaller compared to the energy resolution of the EDS detector (133 eV) in the present study. Generally, the resolution of a commercial EDS system is approximately 130 eV [60]. In addition, it is worthwhile to note that Nb does not exhibit a significant difference of intensity between the dendritic and interdendritic regions, in contrast to Ta (8.146 keV). Therefore, it is reasonable to conclude that the significant segregation of Zr leads to incorrect mapping of Nb.

The presence of the V-rich regions is unusual and suggests the existence of an additional phase. Consequently, the configuration of the detector in SEM is adjusted to combine backscattered with secondary electrons, anticipating that this would yield additional information. For an easier comparison, the same region used for EDS-mapping is shown in Fig. 3.4. It is clear that the V-rich regions correspond to a group of inclusions. These inclusions show a high contrast due to the small height difference compared to the interdendritic region where they are situated. This height difference is more apparent than that in Fig. 3.3 because of the secondary electron signals. The difference results from the varying resistance against grinding and polishing during metallographic preparation, indicating distinct physical properties and thus confirming the existence of an additional phase.

The EBSD results are shown in Fig. 3.5. The band contrast (Fig. 3.5a) and the grain boundary (Fig. 3.5b) reveal that the as-cast state exhibits a coarse grain size larger than 100 µm. The inverse pole figure (IPF) results in Figs. 3.5c and d indicate that adjacent dendritic and interdendritic regions are located within the same grain, with the

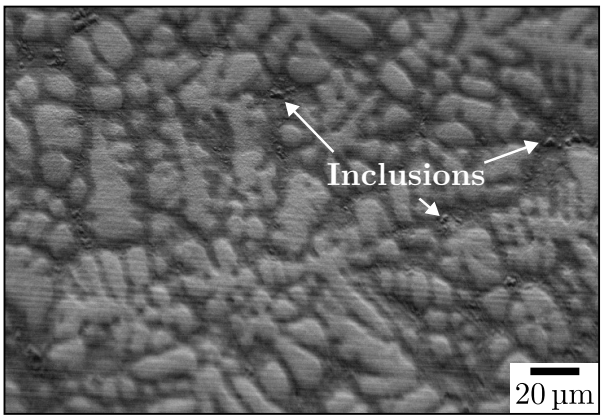

Fig. 3.4: SEM micrograph of the EDS-mapped region in RHEA MoNbTaTiVZr, obtained using a combined backscattered and secondary electron configuration.

grain boundary situating in the interdendritic region. Note that the orientation misfit threshold for the present EBSD results is set at 8° instead of the conventional value (15°) for high angle grain boundaries, and subsequent investigation in the software reveals a difference of less than 3°. Inclusions are observed on both grain boundaries and inside the grains (white arrows) in the composite image of the IPF and SEM micrograph shown in Fig. 3.5e. Fig. 3.5f shows the phase identification results obtained using the combined EBSD + EDS measurement, as the identification using EBSD alone requires a difference of lattice constants above 10 % for the same crystal structure.

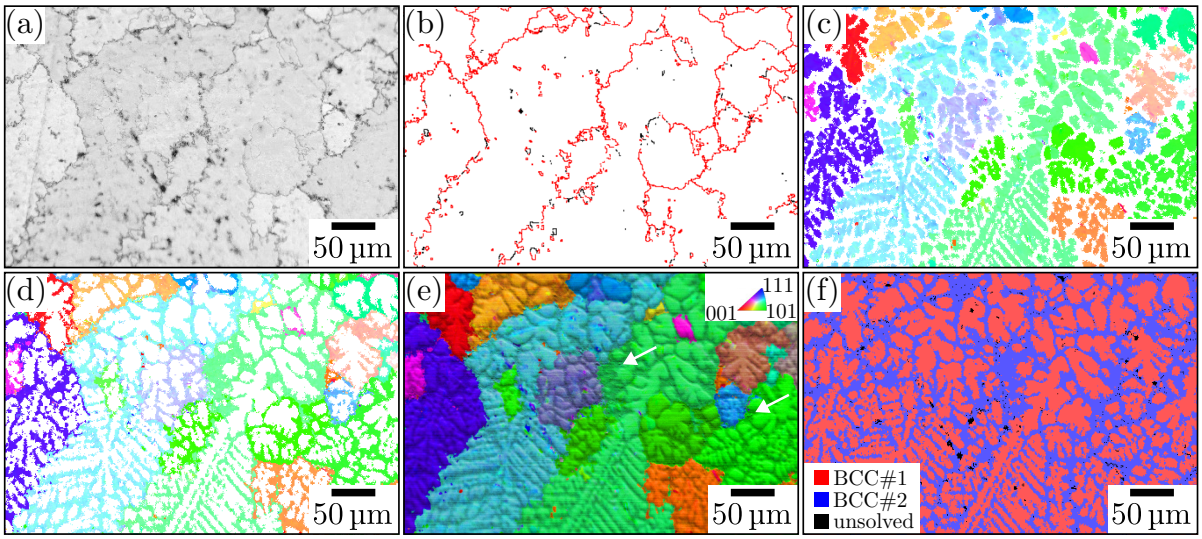

Fig. 3.5: EBSD results for RHEA MoNbTaTiVZr. (a) Band contrast, (b) grain boundary, (c) inverse pole figure (IPF) of the dendritic region, (d) IPF of the interdendritic region, (e) composite image of IPF and SEM micrograph, and (f) phase identification results. Adapted from [56].

3.1.3 Motivation for investigating vanadium addition

The previously described findings suggest that the RHEA MoNbTaTiVZr might consist of three phases, which is inconsistent with the ThermoCalc results shown in Fig. 3.1. Furthermore, the empirical rules for predicting phases in HEAs appear insufficient to accurately explain the phase composition (see Tabs. 1.1 and 1.3). The findings differ from those of Mu et al. [61], who claimed the same alloy composition to be single-phase based on light optical microscopy and XRD using CuKα radiation. Nevertheless, their analysis did not thoroughly investigate the interdendritic region. Additionally, they omitted a significant range of the diffractograms below a diffraction angle of 37.5° (corresponding to a wave vector of approximately 2.6 Å^{-1}).
Even though the results shown in Fig. 3.5f provide a possibility for the phase identification of two BCC phases, the combined measuring system relies more on the EDS results than on the actual lattice constant difference. The V-rich inclusions are also identified as the same phase present in the interdendritic regions. Moreover, a large asymmetry is observed left to the (110)-peak of the major BCC phase if the logarithmic scale of the diffracted intensity is plotted, see Fig. 3.6a.

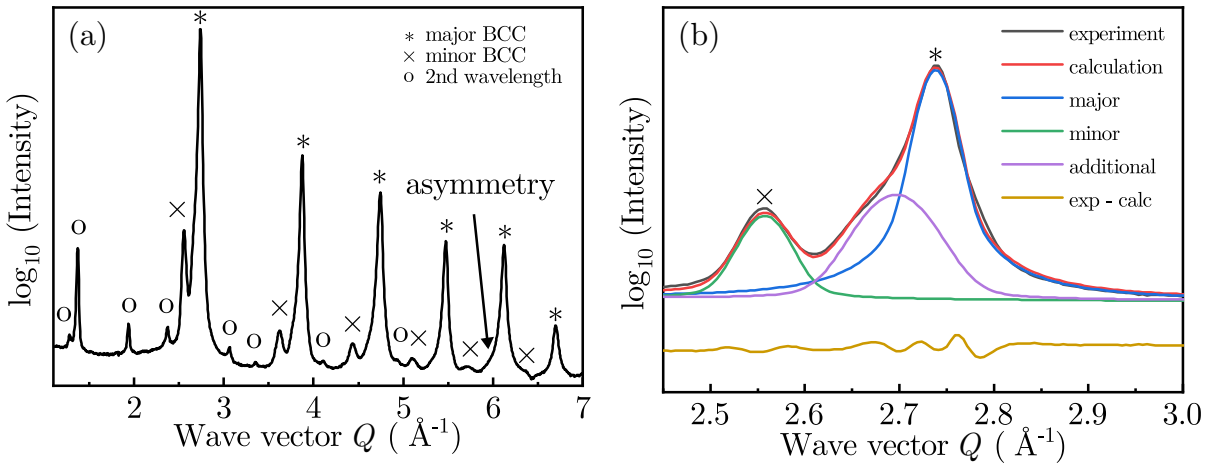

Fig. 3.6: Asymmetry in the HEXRD pattern of MoNbTaTiVZr. (a) Plot representing the logarithmic scale of diffracted intensity. (b) Illustration of the asymmetry in Rietveld refinement. After [48].

The logarithmic plot reveals the details of phases exhibiting weak diffraction intensity. The peak asymmetry leads to a large difference between the calculated and experimental diffractogram in Rietveld refinement. This difference can only be compensated by adding an additional set of peaks, as shown in Fig. 3.6b. Note that the synchrotron X-ray beam contains a second wavelength (marked with "o"), as described in Section 2.2.1. Therefore, a careful investigation on the occurrence of the inclusions is necessary for

a better understanding of the actual phase composition. As the inclusions are rich in vanadium, an investigation of the effect of vanadium addition is required. Previous research studies of the RHEA MoNbTaTiZr, in which vanadium was absent, did not show the presence of these V-rich inclusions [62, 63].

3.2 Effect of vanadium addition

To investigate the effect of vanadium addition (V-addition), a series of RHEAs MoNbTaTiV_xZr with varying x (x = 0, 0.1, 0.2, 0.4, 0.6, 0.8) are fabricated using the arc-melting method, in addition to the previously described senary equimolar RHEA ($x = 1$). For a systematic study and an easier comparison, results of the senary equimolar RHEA under the same condition are also shown. According to the V-addition x, samples are denoted as V_x. The nominal elemental concentrations of each RHEA are listed in Tab. 3.2.

Tab. 3.2: Nominal alloying elements concentration (at. %) in RHEAs MoNbTaTiV_xZr (V_x).

	V_0	$V_{0.1}$	$V_{0.2}$	$V_{0.4}$	$V_{0.6}$	$V_{0.8}$	V_1
Vanadium	0	1.96	3.85	7.41	10.71	13.79	16.67
Other elements (each)	20	19.61	19.23	18.52	17.86	17.24	16.67

3.2.1 Effect of V on microstructure

The SEM micrographs of RHEAs V_x are shown in Figs. 3.7a-g. Their insets depict the enlarged view of the interdendritic region where V-inclusions are situated. Similar to Fig. 3.4, the detector configuration is optimized for enhanced contrast of V-inclusions, while still enabling differentiation between dendritic and interdendritic regions.
The dendritic microstructure is present despite the varying V-addition x. As expected, the insets reveal the absence of irregularly shaped V-inclusions when x is reduced to 0.4, and their emergence when $x \geq 0.6$. The EDS-mapping results of V_1 in Fig. 3.7g confirm the enrichment of V in the inclusions. In addition, the depletion of Zr in them is also observed. These findings are consistent with the previously described results (see Fig. 3.3). For comparison, the mapping results of $V_{0.1}$ are shown in Fig. 3.7h. Note that the magnification of the inset of Fig. 3.7g (V_1) is enlarged for an enhanced mapping contrast of the V-inclusions.
Figs. 3.8a and b show the quantitative EDS results for the dendritic and interdendritic regions of V_x, respectively. Evidently, Zr enrichment in the interdendritic region and

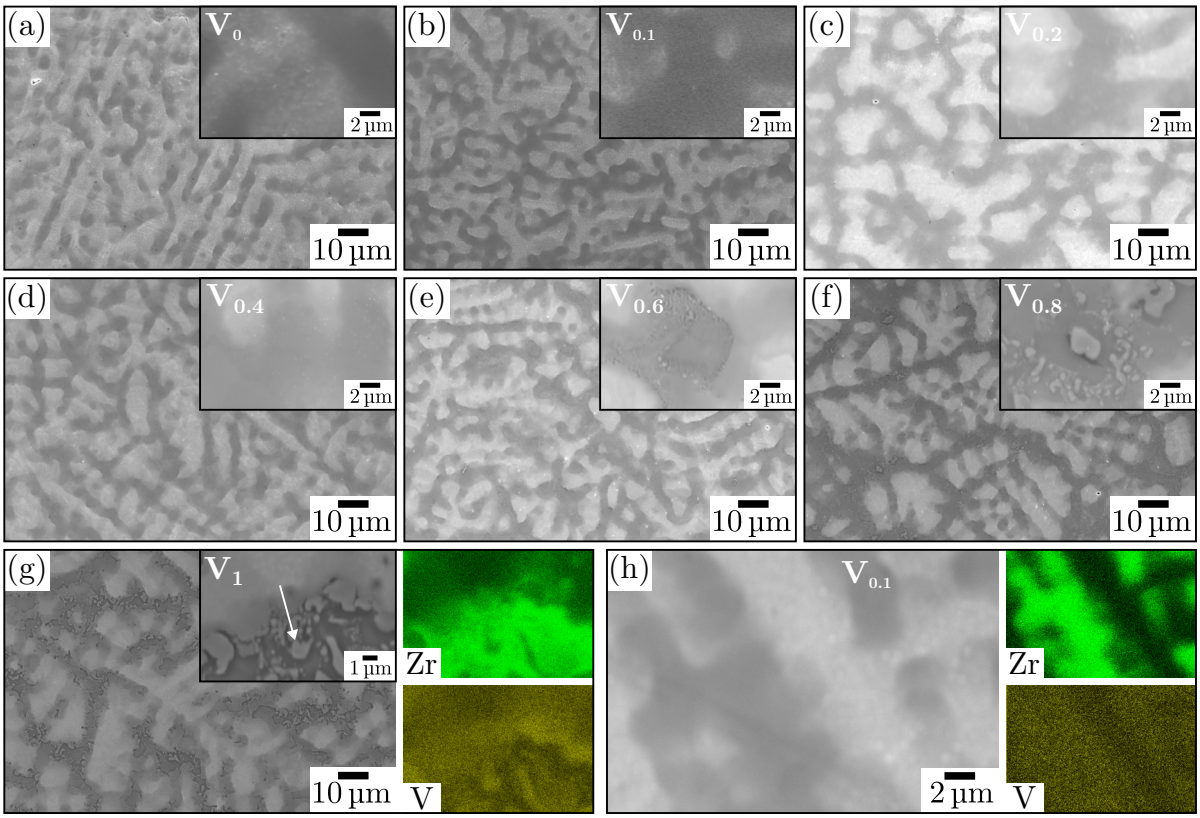

Fig. 3.7: SEM micrographs of RHEAs MoNbTaTiV_xZr (V_x) with different V-addition. (a) V_0, (b) $V_{0.1}$, (c) $V_{0.2}$, (d) $V_{0.4}$, (e) $V_{0.6}$, (f) $V_{0.8}$ and (g) V_1. V and Zr mapping of (g) V_1 and (h) $V_{0.1}$.

depletion in the dendritic region remain consistent across all alloys V_x. The anomalously large error bar for Zr in the interdendritic region may be attributed to the Zr depletion in V-inclusions. As the value of x increases, the concentration of V (purple) also increases in both the dendritic and interdendritic regions. In the interdendritic region, the slope of the increase is slightly steeper up to $x = 0.6$. Beyond this, further increases in x seem to lead to saturation of the V concentration. Meanwhile, the slope of the V concentration increase in the dendritic region remains almost constant. For the other four alloying elements, no significant variations in concentration are observed, although most exhibit a moderate downward trend due to V-addition.

HEXRD patterns of the RHEAs V_x are shown in Fig. 3.9. The peaks of the minor phase should be attributed to the V-inclusions, as SEM results indicate their occurrence from $x = 0.6$ onwards. In alloys V_0 - $V_{0.4}$, where only dendritic and interdendritic regions are present, an additional group of peaks with weaker intensities than those of the major phase can be found. This group of peaks corresponds to the peak asymmetry mentioned earlier (see Fig. 3.6). As these peaks are positioned to the left of those of the major BCC phase, they are also identified as BCC structure. These peaks are believed to originate

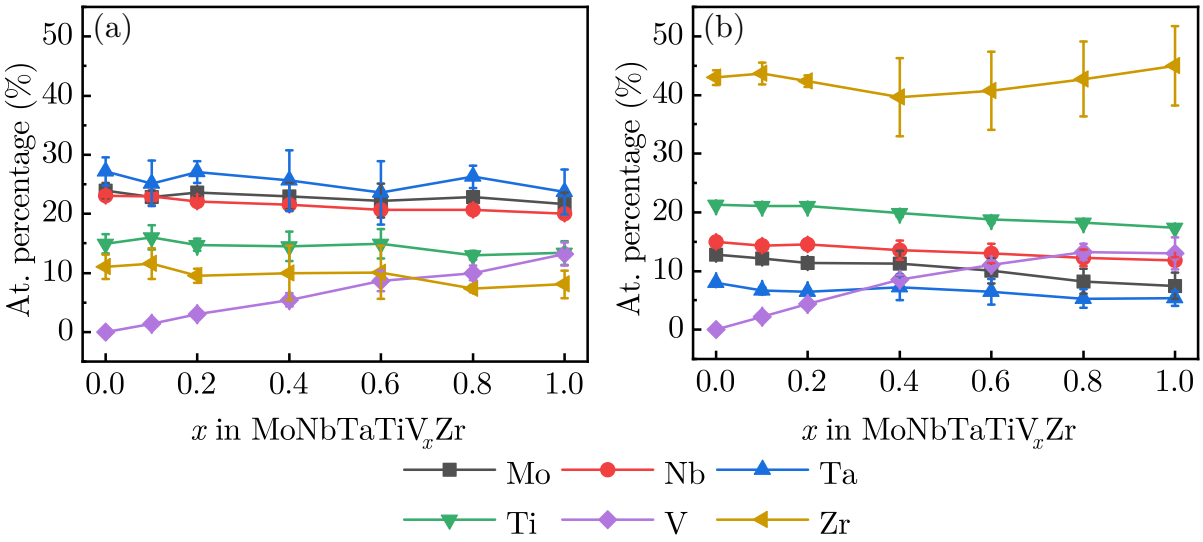

Fig. 3.8: Effect of V-addition on the chemical composition in the (a) dendritic and (b) interdendritic regions. Averaged from five point analyses using EDS.

from the interdendritic region, which exhibits a lower volume fraction compared to the dendritic region. The findings enable a correct phase identification, as indicated by the solid arrows in Fig. 3.9.

The evolution of lattice constants and the volume fraction of V-inclusions, as determined by Rietveld refinement, are shown in Fig. 3.10. For the dendritic and interdendritic regions, their lattice constants both exhibit a decreasing trend. In particular, the lattice constant of the dendritic region shows a uniform decrease, while that of the interdendritic region declines gradually from $V_{0.4}$ to $V_{0.8}$ before dropping drastically to V_1. In contrast, the lattice constant of the V-inclusions remains nearly constant upon their appearance at $x = 0.6$, and their volume fraction is likely to saturate at V_1. Note that the error bars of the lattice constants of the dendritic and interdendritic regions are too small to be depicted in the figure. Additionally, the volume fraction of the V-inclusions provides only a qualitative estimate, as the precise chemical composition necessary for an accurate determination of the structure factor in Rietveld refinement is lacking.

The equivalent atomic radius r_e of a BCC crystal structure with a lattice constant of a can be roughly estimated as:

$$r_e = \frac{\sqrt{3}a}{4}. \tag{3.1}$$

The lattice constants of the dendritic and interdendritic regions of alloy V_0 are approximately 3.28 and 3.36 Å, respectively. The corresponding radii are 1.42 and 1.45 Å. According to the classical Hume-Rothery rules [33], the formation of a substitutional solid

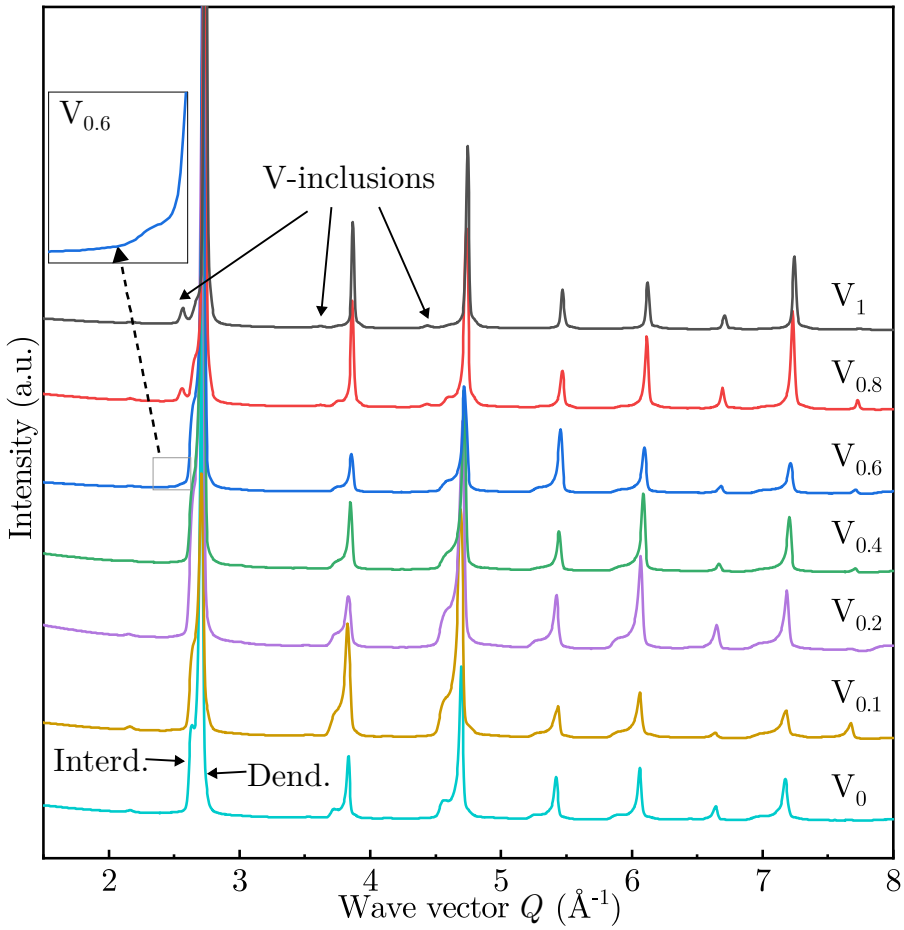

Fig. 3.9: HEXRD patterns of RHEAs MoNbTaTiV$_x$Zr (V$_x$) with different V-addition.

solution is likely since the radius of the solute atom vanadium (1.35 Å) varies by less than 15 % from that of the solvent. Thus, the dissolution of vanadium into the crystal lattice should result in a smaller lattice constant and a peak shift towards a larger wave vector. With increasing V-addition x, the peaks of both dendritic and interdendritic regions shift to larger wave vectors. However, vanadium seems to dissolve more readily in the interdendritic than in the dendritic region, as also confirmed by the EDS-mapping of the RHEA V$_{0.1}$ (see Fig.3.7h). Consequently, the two distinguishable groups of peaks in alloy V$_0$ merge into an indistinguishable set in alloy V$_1$.

As previously mentioned, the empirical rules for predicting phases in HEAs appear to be inapplicable for the alloy V$_1$, except for the Allen-electronegativity mismatch factor $\Delta\chi_{\text{Allen}}$. Given the significant contribution of vanadium to the increase in $\Delta\chi_{\text{Allen}}$, it would be expected that single-phase alloys could form in alloys V$_x$ with a gradual reduction in V-addition. However, these rules seem inadequate in explaining the phase composition for all of the alloys V$_x$. The calculated thermodynamic parameters for alloys V$_x$, which are used for the empirical rules, are listed in Tab. 3.3. By entirely exclud-

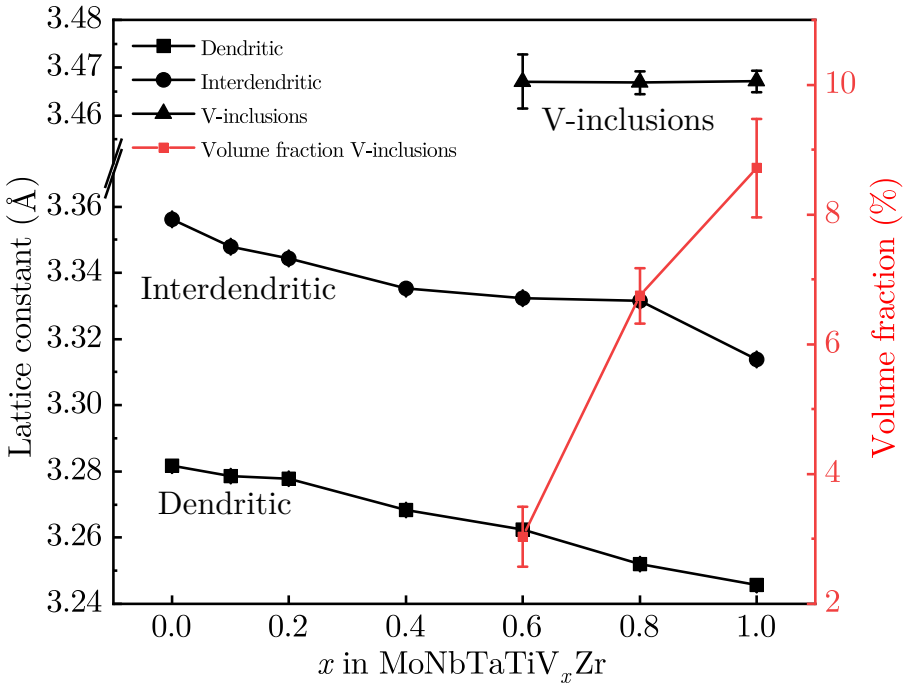

Fig. 3.10: Lattice constants and volume fraction of V-inclusions obtained from Rietveld refinement of diffractograms.

ing vanadium, all the parameters of alloy V_0 suggest the formation of a single-phase alloy. Nevertheless, the observed results show a dual-phase dendritic microstructure. The V-addition results in an increase of $\Delta\chi_{\text{Allen}}$ from 5.31 % (V_0) to 6.34 % ($V_{0.4}$) and 7.29 % (V_1). As described in Section 1.3, single-phase solid solution should be present for $\Delta\chi_{\text{Allen}} < 6\,\%$. This might be related to the emergence of V-inclusions, although the prediction is not precise, as V-inclusions are observed from $V_{0.6}$ onwards.

Tab. 3.3: Parameters of RHEAs MoNbTaTiV$_x$Zr (V_x) for empirical phase prediction rules.

	ΔS_{mix} J/(K·mol)	ΔH_{mix} kJ/mol	δ %	Ω -	$\Delta\chi_{\text{Allen}}$ %	μ -
V_1	14.89	-2.11	5.27	17.89	7.29	4.38
$V_{0.8}$	14.87	-2.07	5.18	18.31	7.05	4.22
$V_{0.6}$	14.78	-2.02	5.08	18.77	6.75	4.07
$V_{0.4}$	14.59	-1.95	4.98	19.26	6.38	3.91
$V_{0.2}$	14.22	-1.86	4.86	19.74	5.92	3.76
$V_{0.1}$	13.92	-1.81	4.79	19.9	5.64	3.68
V_0	13.38	-1.76	4.73	19.79	5.31	3.6

3.2.2 Effect of V in thermodynamic simulations

The previous section provides a comprehensive explanation of how V-addition influences the microstructure, which enables an accurate identification of the peak positions for individual phases in the diffraction pattern. Despite these findings, the formation of the unexpected V-inclusions still remains unexplained. This section aims to address this issue by investigating the effect of V-addition through thermodynamic simulations.

Equilibrium phase composition

Using the same method as in Section 3.1.1, the effect of V-addition on the predicted phase composition of RHEAs MoNbTaTiV_xZr is first examined, see Fig. 3.11. As also mentioned in Section 3.1.1, these results focus on the high-temperature range.

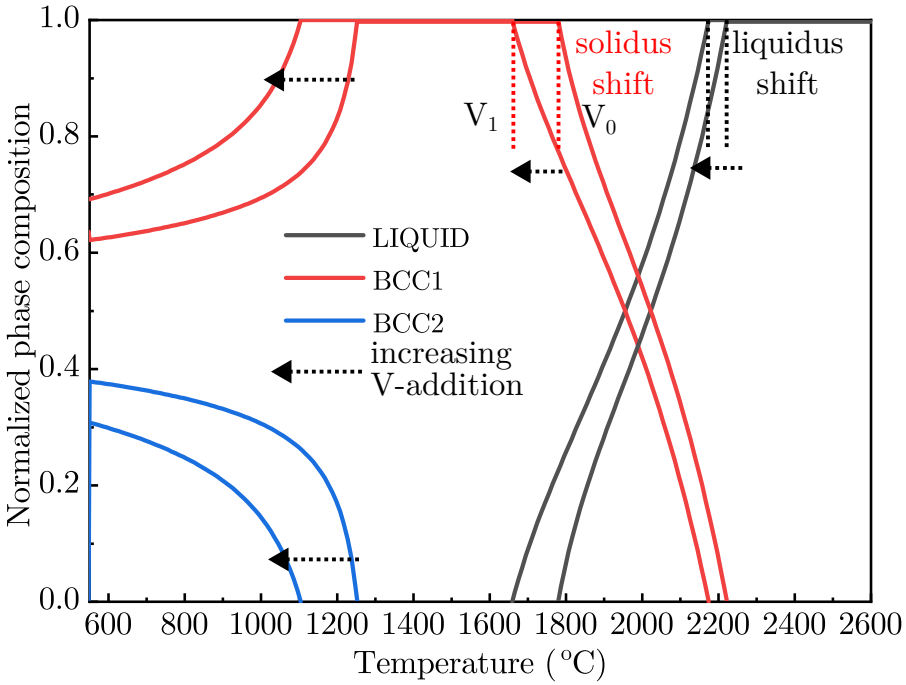

Fig. 3.11: Evolution of predicted equilibrium phase compositions for RHEAs MoNbTaTiV_xZr (V_x) with increasing V-addition, calculated using CALPHAD-method.

The predicted equilibrium phase composition shows minimal influence from V-addition, as the consistent presence of a single-phase BCC at elevated temperatures and the co-existence of two BCC phases (BCC1 and BCC2) at moderate temperatures are observed. This prediction is inconsistent with the results shown previously. However, by adding vanadium, the solidus and liquidus lines shift to lower temperatures. This is due to the lower melting point of vanadium (about 1900 °C) compared to that of the RHEAs. The shift of the solidus line (1780 to 1658; 122 °C) is more pronounced than that of

the liquidus line (2221 to 2175; 46 °C), and the lower boundary that forms single-phase BCC1 shifts from 1252 to 1104 °C. It is important to note that RHEAs containing alloying elements with large differences in melting points may result in microsegregation during solidification due to their varying effects on the stabilization of the liquid phase [2, 15]. Such a microsegregation is clearly shown in all RHEAs V_x.

Therefore, a detailed investigation of solidification is necessary, especially considering the longer solidification interval indicated by the larger shift of the solidus line compared to that of the liquidus line. The study focuses on the chemical composition in the liquid phase. The evolution of Zr and V concentrations is examined, as the formation of V-inclusions takes place in the interdendritic region, which exhibits a significant enrichment of Zr.

Solidification

The results of the solidification simulation are presented in Fig. 3.12. While Figs. 3.12a and b depict the results in equilibrium solidification, Figs. 3.12c and d are those obtained using the Scheil-Gulliver model [54, 55].

In the case of equilibrium solidification, an enrichment of Zr in the liquid phase is observed (Fig. 3.12a), which agrees well with the Zr enrichment found in the interdendritic region. However, no pronounced enrichment of V can be identified. The mole fraction of the liquid phase (Fig. 3.12b) shows a small shift of the endpoint of solidification as V-addition increases. In contrast, the results derived from Scheil-solidification, which assumes that the solid phase is "frozen" regarding diffusion, reveal a phenomenon that is more consistent with the experimental findings. A marked V enrichment in the melt becomes more pronounced with increasing V-addition. For alloy $V_{0.6}$ (blue), the V concentration is almost the same as that of Zr at the end of solidification (inset in Fig. 3.12c). Furthermore, a much longer solidification path is observed with increasing V content (Fig. 3.12d). The endpoint of solidification significantly shifts from 1600 °C to 1282 °C with increasing x up to $V_{0.6}$. Beyond this point, the shift becomes less pronounced, with V_1 reaching an endpoint of 1250 °C, indicating a near saturation of the effect. According to the V-Zr binary phase diagram [64], the maximum solubility of V in Zr is only about 20 at. % at 1265 °C. The eutectic point at 43 at. % and 1265 °C indicates a shift of the solidification path from the BCC + liquid region to the V_2Zr (Laves) + liquid region when the concentrations of V and Zr are equal (50 at. %). As such, the solidification simulation results suggest the emergence of an additional Laves phase from $x = 0.6$ onwards. However, instead of the expected Laves-phase V_2Zr, the experimental observations reveal the formation of a BCC phase. This discrepancy could be due to the fact that the

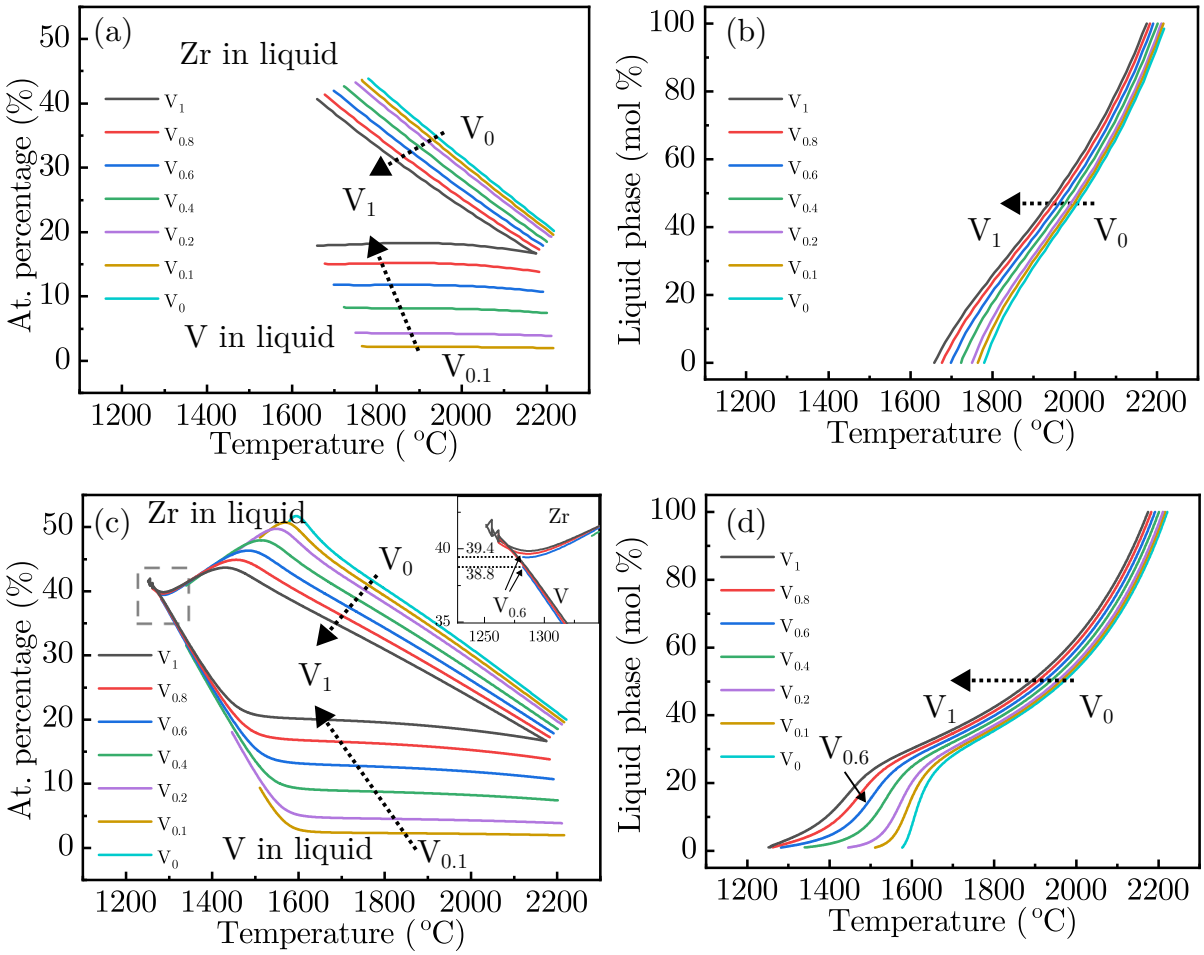

Fig. 3.12: CALPHAD results of RHEAs MoNbTaTiV$_x$Zr (V$_x$) considering the equilibrium (a-b) and Scheil (c-d) solidification, showing (a) and (c) the evolution of V and Zr concentrations in the liquid phase with increasing V-addition, and (b) and (d) the mole percentage of the liquid phase during solidification. The dashed arrow indicates their trends as the V-addition x increases.

liquid phase predicted by the Scheil-model (Fig. 3.12c) still contains about 20 at. % of the other four alloying elements at the end of solidification. Due to the high entropy of mixing, such a coexistence of multiple elements leads to the formation of solid solutions, which in this case are the BCC V-inclusions, with a small volume fraction, since the vanadium enrichment is most pronounced at the end of solidification.

Despite of the fact that solidification in practice should be a combination of these two extreme conditions, the results from Scheil-solidification are more likely to match with reality, as diffusion in HEAs is believed to be sluggish [5]. Although a recent study [65] claims that Zr exhibits a fast diffusion rate, assigning Zr to be diffusing fast in the Scheil-solidification still leads to similar conclusions, see Fig. 3.13. In addition, as the amount of the other four alloying elements increases from 20 to about 30 at. % (Fig. 3.13a), the

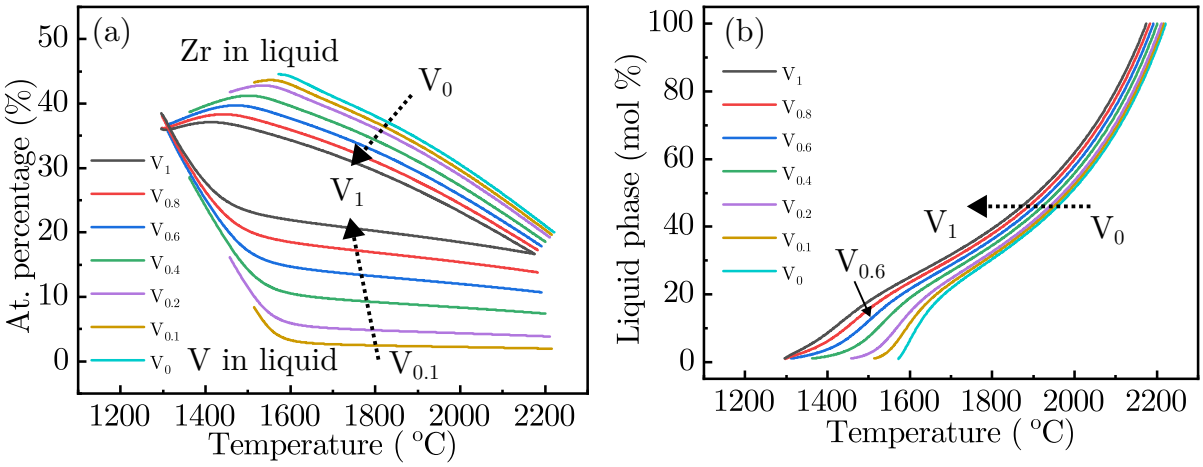

Fig. 3.13: Scheil-solidification simulation results assuming that the Zr diffuses fast. (a) Atomic percentages of Zr and V in liquid phase and (b) mole percentage of liquid phase during solidification.

mixing entropy rises. This further substantiates the formation of a solid solution instead of a Laves phase.

While empirical rules and phase predictions using the CALPHAD-method are inapplicable for predicting phase composition in alloys V_x, the solidification simulation results provide a plausible explanation for their microstructure and phase composition. This highlights the need for careful consideration of the solidification path in the design of HEAs, especially true for RHEAs that commonly exhibit microsegregation.

3.3 Subgroup alloys: insights into microsegregation

The results in the previous sections indicate that the expected single-phase RHEA MoNbTaTiVZr actually consists of three phases. The formation of the Zr-rich interdendritic region and V-inclusions could be explained by Scheil-solidification. Although such a phase composition appears to be a combined effect of V and Zr, it is preferable to preserve these two elements instead of completely discarding them. Their significantly different atomic radii compared to the other four elements can result in substantial solid solution hardening, thereby leading to enhanced mechanical properties.

In this section, the microstructures of four subgroup alloys of the RHEA are studied. This study encompasses two alloys formulated using the natural-mixing guided design approach, as well as the RHEAs MoNbTaTiV and MoNbTaTi.

On one side, the study of alloys designed with natural-mixing guidance examines the attempt to obtain a microsegregation-free alloy by merely adjusting the chemical composition. On the other side, the investigation of the microstructure of RHEAs MoNbTaTi

and MoNbTaTiV is aimed at confirming the complex interplay between the solid solution effects and the undesired microsegregation introduced by V and Zr.
Although the microstructures of the RHEAs, MoNbTaTi and MoNbTaTiV, have already been studied in the literature [66, 67], it is worthwhile examining if the microstructures are identical by using the fabrication method in the present work.

3.3.1 Natural-mixing guided composition alloys

In the pursuit of single-phase RHEAs, one effective approach is to alter the composition guided by the principles of natural-mixing [68]. The principle is to extract the chemical composition from regions in alloys that exhibit microsegregation. Alloys with such chemical compositions have been shown to form a segregation-free single-phase microstructure with outstanding mechanical properties. Applying this strategy to the present RHEA suggests that alloys with a chemical composition of the dendritic or the interdendritic region could be free of segregation. Hence, two alloys denoted as NM-D (Natural-Mixing Dendritic) and NM-ID (Natural-Mixing InterDendritic) with their composition shown in Tab. 3.4 are fabricated using the same method as before.

Tab. 3.4: Nominal alloying elements concentration (at. %) of alloys with natural-mixing guided chemical composition of dendritic region (NM-D) and interdendritic region (NM-ID).

	Mo	Nb	Ta	Ti	V	Zr
NM-D	20	20	20	15	15	10
NM-ID	7.5	12.5	5	15	15	45

Fig. 3.14 shows the SEM and EDS results for these two alloys. The microsegregation is still present, see Figs. 3.14a_1 and b_1. The enlarged view for alloy NM-D (Figs. 3.14a_2) indicates that the interdendritic region becomes smaller due to the decreased concentration of elements with low-melting points, i.e. Ti, V and Zr. Since the EDS point analysis is not precise for such small regions, EDS line scans with a scanning distance of 2 µm are employed. To aid in tracking the results, four specific positions, A, B, C, and D, are marked in both the micrographs and EDS results.
Despite the efforts, inclusions are still present in the alloy NM-D (Fig. 3.14a_2). The EDS results at positions A and B, where inclusions are present, show a clear enrichment of vanadium (Fig. 3.14a_3). In the alloy NM-ID, the V-rich regions appear to be larger (Fig. 3.14b_2). The EDS results at positions C and D also reveal an enrichment of vanadium. However, the enrichment of vanadium at position D appears to be much more significant than at position C. Moreover, the V-rich regions at position D exhibit a morphology similar to that observed in typical eutectic solidification.

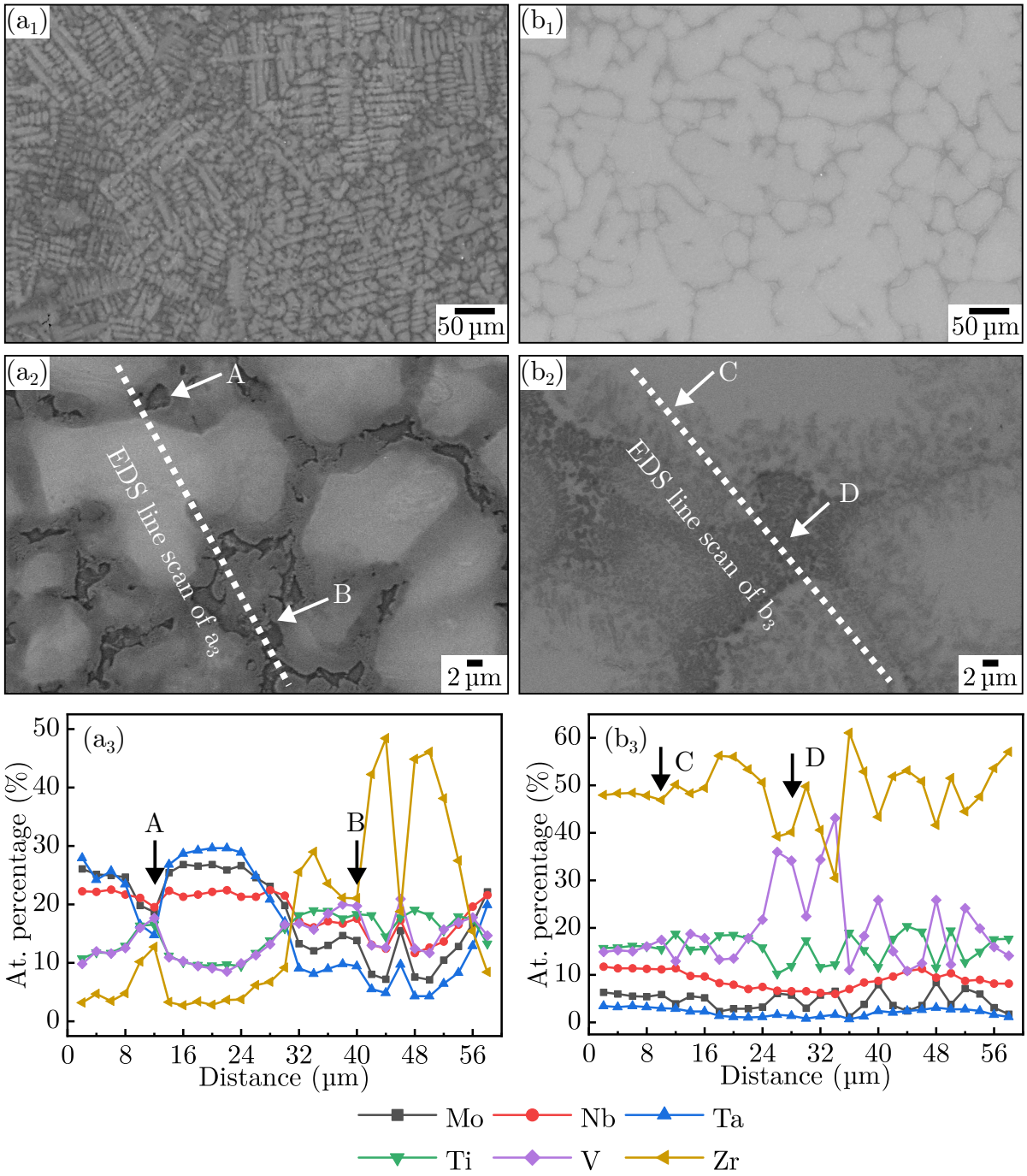

Fig. 3.14: SEM micrographs and EDS analysis of alloys with chemical composition of (a) dendritic region and (b) interdendritic region. Subscripts represent $_1$ for low magnification micrographs, $_2$ for high magnification micrographs used for EDS line scans, and $_3$ for EDS line scanning results by a distance of 2 µm. Four specific positions, A, B, C and D, are indicated by arrows in $_2$ and $_3$.

The XRD patterns of alloys NM-D and NM-ID are shown in comparison with that of their master alloy MoNbTaTiVZr, see the left panel of Fig. 3.15. For a clearer illustration of the peaks of minor phases, the logarithmic-scaled diffraction intensity is shown in the right panel. Note that the results are normalized for easier comparison.

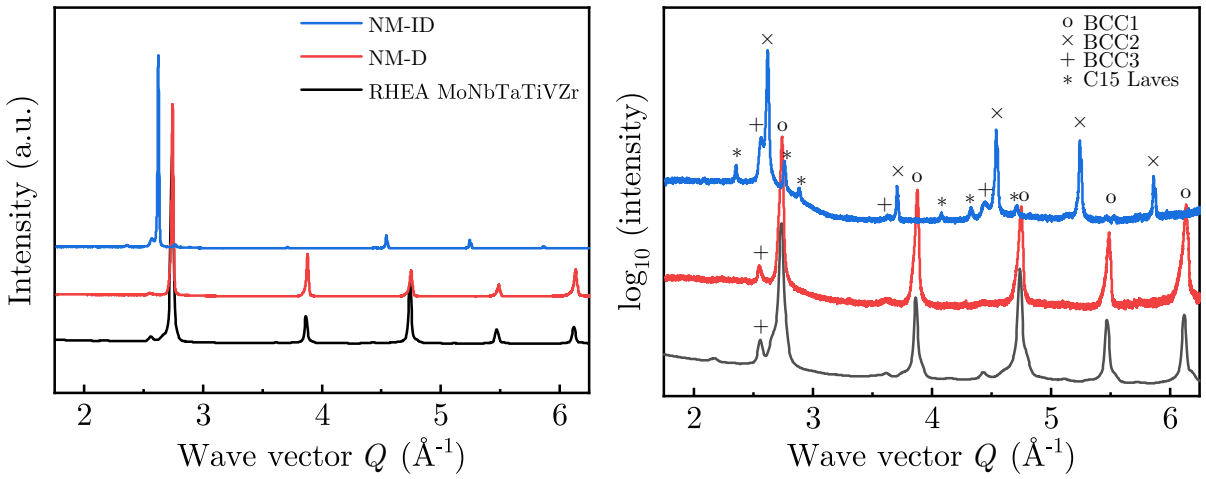

Fig. 3.15: XRD patterns of alloys with chemical composition of dendritic (NM-D) and interdendritic region (NM-ID) in comparison with their master alloy MoNbTaTiVZr.

The XRD pattern of alloy NM-D (red) is nearly identical to that of the master alloy. The asymmetry due to the interdendritic region appears to be insignificant near the (110)-peak but remains observable at larger wave vectors. This indicates a shift to larger wave vectors of the peaks of the interdendritic region and a decrease of the lattice constant. This is most likely due to the decreased concentration of the large atom Zr.
For the alloy NM-ID (blue), three phases are present, comprising two BCC phases and a C15 Laves (cubic) phase. The major BCC phase shows a shift to a smaller wave vector compared to the asymmetry (interdendritic) in the master alloy. Interestingly, the minor BCC phase's peaks nearly align with the position of the V-inclusions, suggesting a possible correspondence. The lattice constants of the phases in the three alloys are shown in Tab. 3.5. It is also noted that the lattice constant of the C15 Laves phase (7.55 Å) is slightly larger than that of the standard V_2Zr (7.44 Å) [69].

Tab. 3.5: Lattice constants (Å) of phases in alloys with chemical composition of dendritic region (NM-D) and interdendritic region (NM-ID) in comparison with their master alloy MoNbTaTiVZr.

Master alloy		NM-D		NM-ID	
dendritic	3.25	major BCC (BCC1)	3.24	major BCC (BCC2)	3.39
interdendritic	3.31	minor BCC (asymmetry)	3.27	minor BCC (BCC3)	3.46
V-inclusions	3.47	V-inclusions (BCC3)	3.48	C15 Laves	7.55

The previously described results demonstrate that the natural-mixing guided design strategy does not effectively create a segregation-free microstructure in the present RHEA. Nevertheless, the presence of the Laves phase in the alloy NM-ID might suggest an interesting phenomenon during its solidification. The simulation results for alloys NM-D and NM-ID are shown in Fig. 3.16. To facilitate a more comprehensive understanding, the equilibrium phase composition predictions (top) are also illustrated alongside the solidification simulations (bottom).

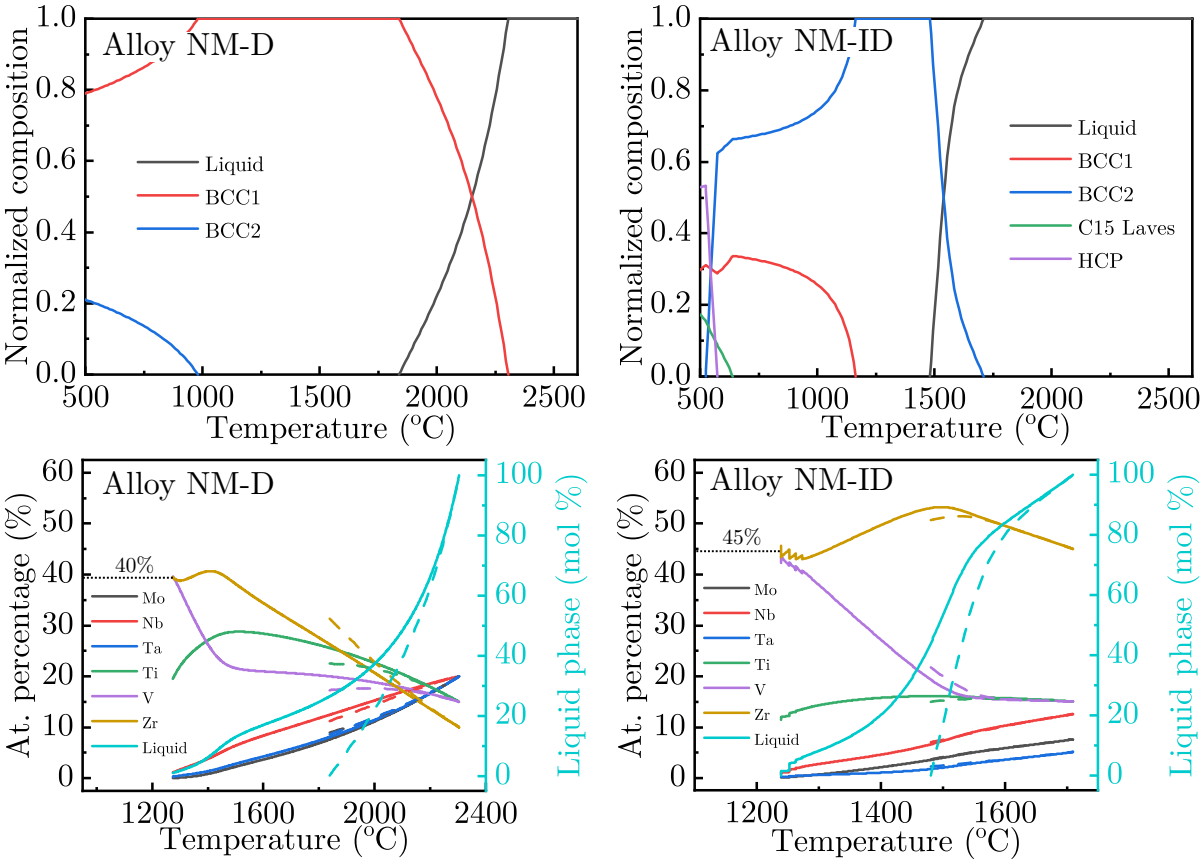

Fig. 3.16: Thermodynamic calculation results for alloys with chemical composition of dendritic (NM-D) and interdendritic region (NM-ID) of alloy MoNbTaTiVZr. Top: predicted equilibrium phase composition. Bottom: elemental composition in the liquid phase and the mole percentage of the liquid during solidification, including solid lines for Scheil-solidification and dashed lines for equilibrium solidification.

For the alloy NM-D, both the predicted phase composition and the elemental distribution during solidification are similar to that of the master alloy (see Figs. 3.1 and 3.12). In addition, Zr appears to be enriched significantly during solidification even when its initial concentration is reduced from 16.67 % to 10 %. Also alloy NM-ID shows an enrichment of Zr, with an initial concentration of 45 %. Furthermore, the sum of the concentrations of V and Zr at the end of solidification appears to be larger than 90 %. This value is

higher than that for the alloy NM-D (about 80 %), leading to a lower mixing entropy. As discussed in the solidification of the master alloy, the mixing entropy in this case may not be high enough for the formation of BCC V-rich inclusions. Instead, such a coexistence of V and Zr is likely to result in the formation of the intermetallic Laves phase.
Although single-phase homogeneous alloys could not be achieved through the natural-mixing strategy, the observations emphasize the accuracy and significance of solidification studies for RHEAs containing microsegregation.

3.3.2 Alloys excluding V/Zr

In the section studying the effect of V-addition, it has been shown that the results for RHEA MoNbTaTiZr (V-excluded) are consistent with that in the literature, while those for MoNbTaTiVZr (RHEA) are not. In addition, it is likely that the microsegregation is due to the combined effect of V and Zr. Although the subgroup alloys MoNbTaTiV (Zr-excluded) and MoNbTaTi (base) have been studied in the literature, it is worthwhile examining if the same microstructure can be achieved using the present fabrication method, and if it could also be explained by Scheil-solidification using ThermoCalc.

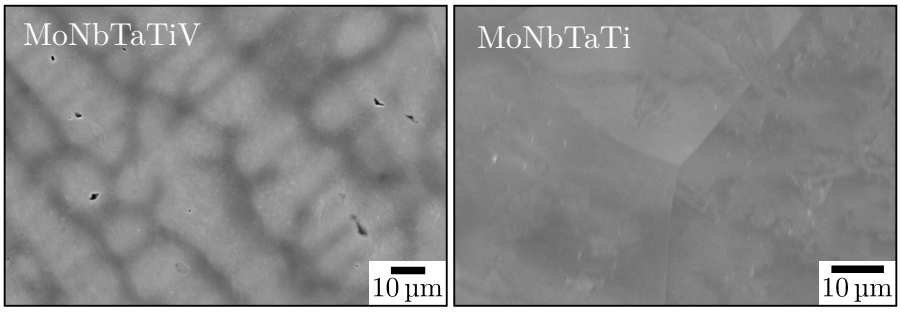

Fig. 3.17: SEM micrographs of RHEAs MoNbTaTiV and MoNbTaTi.

The SEM micrographs of RHEAs MoNbTaTiV and MoNbTaTi are shown in Fig. 3.17. While the microsegregation is still observed in alloy MoNbTaTiV, the RHEA MoNbTaTi exhibits a homogeneous microstructure. These observations are consistent with those reported in [66, 67]. Specifically, the interdendritic region of MoNbTaTiV exhibits segregation of V and Ti [66]. In the course of achieving a segregation-free composition for the present alloy system, it can be assumed that the segregation in the as-cast state can only be eliminated by removing both V and Zr.
The thermodynamic simulation results for the RHEAs MoNbTaTiV and MoNbTaTi are shown in Fig. 3.18. For the alloy MoNbTaTiV, the enrichment of V and Ti in the interdendritic region can be explained by the solidification of the alloy. Both of their concentrations increase during solidification. In contrast, the chemically homogeneous

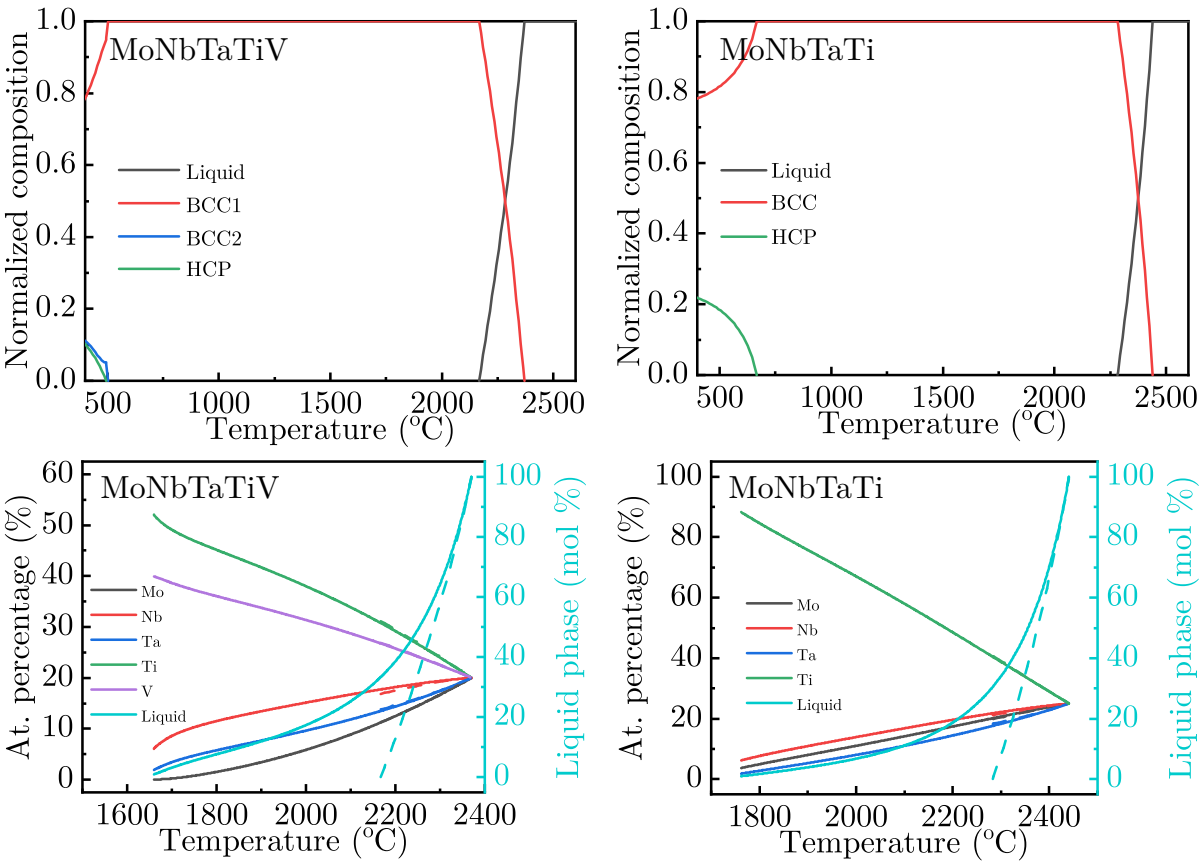

Fig. 3.18: Thermodynamic calculation results for MoNbTaTiV and MoNbTaTi. Top: predicted equilibrium phase composition. Bottom: elemental composition in the liquid phase and the mole percentage of the liquid during solidification, including solid lines for Scheil-solidification and dashed lines for equilibrium solidification.

RHEA MoNbTaTi exhibits an enrichment of Ti alone in the liquid phase, reaching up to 90 %.

However, it should be noted that the end points of solidification for alloys MoNbTaTiV and MoNbTaTi are approximately 1660 °C and 1762 °C, respectively. These temperatures are much higher than that of the RHEA MoNbTaTiVZr (1250 °C), suggesting a higher free Gibbs-energy change due to the contribution of excessive mixing entropy. In the literature studying the RHEA MoNbTaTiV, the alloy is even claimed to be single-phase in spite of an asymmetry in the XRD pattern [66].

An examination of the V-Ti binary phase diagram indicates that the liquidus line for 50 at. % V in Ti is about 1630 °C, while the solidus line is about 10 °C lower than the liquidus line [64]. Instead of the phase decomposition that has been discussed in the V-Zr phase diagram for the RHEA MoNbTaTiVZr, no miscibility gap appears in the V-Ti system until 890 °C. This demonstrates a significant temperature range below the solidus line with a homogeneous BCC microstructure. It is plausible that the dendritic

RHEA MoNbTaTiV possesses a dual-phase microstructure, with indistinguishable peaks in the XRD diagram, which may have led to an incorrect conclusion in [66]. These results highlight again the importance of solidification simulation during RHEAs design.
The melting point of pure titanium is 1673 °C [44]. As the segregation is not found in the alloy MoNbTaTi, it is assumed that there is a competition between the formation of a homogeneous microstructure due to mixing entropy and the segregation due to differences in the melting points of the alloying elements.

3.4 Concluding remarks

The senary equimolar RHEA MoNbTaTiVZr exhibits a dendritic microstructure with V-rich inclusions situated in the interdendritic region. The RHEA contains three BCC phases, and their identification in XRD patterns is achieved by investigating the effects of the addition of V. The formation of microsegregation and phases can be explained using Scheil-solidification simulation. The microsegregation appears to be the combined result of the presence of the alloying elements V and Zr. The natural-mixing guided design strategy proves to be ineffective for the present alloy system. Additionally, the investigation of subgroup alloys reveal a complex interplay between maintaining the presence of V and Zr in the alloy for solid-solution hardening and achieving a chemically homogeneous microstructure.

Chapter 4

Mechanical properties

This chapter presents a comprehensive analysis of the mechanical properties of the RHEA MoNbTaTiVZr. The investigation begins with a preliminary examination of its compression behavior at varied temperatures, followed by a comparison of the microhardness of the RHEA with that of the subgroup alloys to confirm the solid-solution hardening effect attributed to the presence of V and Zr. Subsequently, the influence of V-addition on mechanical properties is systematically investigated to understand the role that V-inclusions play in microhardness and hot compression tests. After that, fractography and deformation mechanism are studied to gain insights into the mechanical behavior of multi-phase RHEAs. Lastly, the thermal stability of the microstructure and the influence of heat treatment on mechanical properties are discussed.

4.1 Preliminary examination

4.1.1 Compression behavior at varied temperatures

Fig. 4.1 shows the compressive stress-strain curves of the RHEA MoNbTaTiVZr at room temperature (RT) and at elevated temperatures. The compression tests at RT and 600 °C do not result in fracture of the specimens, as the dilatometer reaches its maximum applicable force of 20 kN (about 1.6 GPa). The 0.2 %-offset yield strength $R_{\mathrm{p0.2}}$, the compressive strength R_{m} and the fracture strain ε_{f} are listed in Tab. 4.1.
The results demonstrate the outstanding mechanical properties of the RHEA up to at least 800 °C, which is critical for conventional superalloys such as Inconel-718. While Inconel-718 exhibits a strength of 600 MPa and a fracture strain below 10 % at such a high temperature [70], the RHEA exhibits a strength of about 1 GPa and a fracture

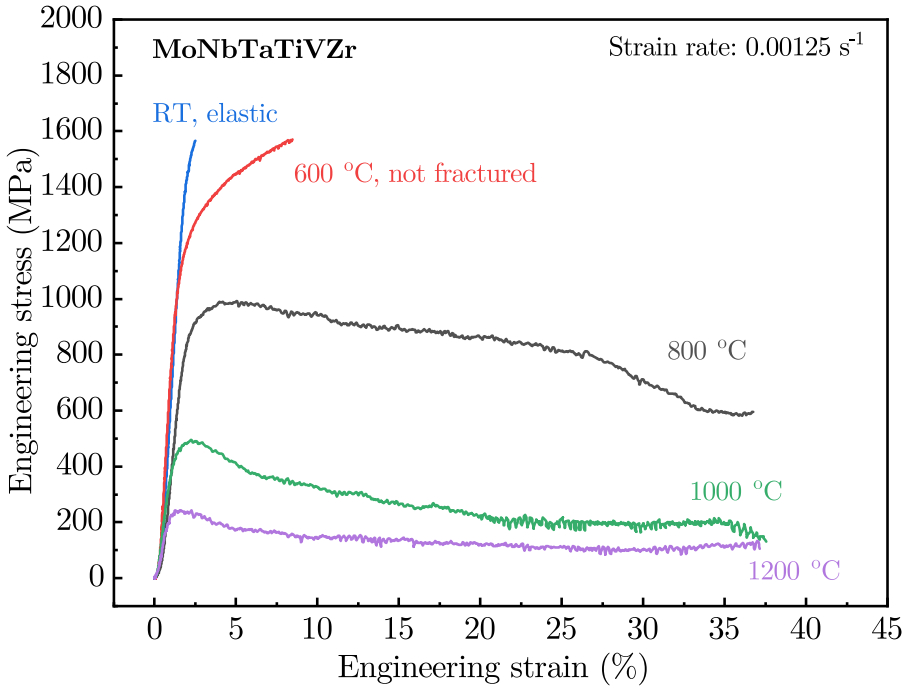

Fig. 4.1: Compressive stress-strain curves of RHEA MoNbTaTiVZr at room temperature (RT) and varied elevated temperatures.

Tab. 4.1: 0.2 %-offset yield strength $R_{p0.2}$, compressive strength R_m and fracture strain ε_f derived from analysis of compressive stress-strain curves of the RHEA MoNbTaTiVZr at varied temperatures.

Temperature °C	$R_{p0.2}$ MPa	R_m MPa	ε_f %
25 (RT)	1400	> 1600	-
600	1174	> 1600	> 8
800	874	992	> 37.5
1000	373	495	> 37.5
1200	200	245	> 37.5

strain over 37.5 %. This combination of high strength and ductility indicates that the RHEA is a promising material for high-temperature applications.

Despite the technical limitations, the yield strength at RT and at 600 °C are approximately 1.4 and 1.17 GPa, respectively. Furthermore, the alloy exhibits a fracture strain of at least 8 % at 600 °C. The high strength is maintained until the temperature is increased to 1000 °C, where noticeable softening is observed. This suggests that the RHEA can be easily deformed by hot working, making it highly promising for high-temperature applications up to 800 °C.

Due to the technical limitation in characterizing the RT compression behavior, the mechanical properties at RT are characterized via microhardness tests.

4.1.2 Microhardness and solid-solution hardening by V/Zr

The extent of solid-solution hardening in HEAs can be partially characterized by the atomic size mismatch δ (refer to Eq. 1.4). The microhardness values and atomic size mismatch factor of the RHEA MoNbTaTiVZr and its subgroup alloys are shown in Fig. 4.2.

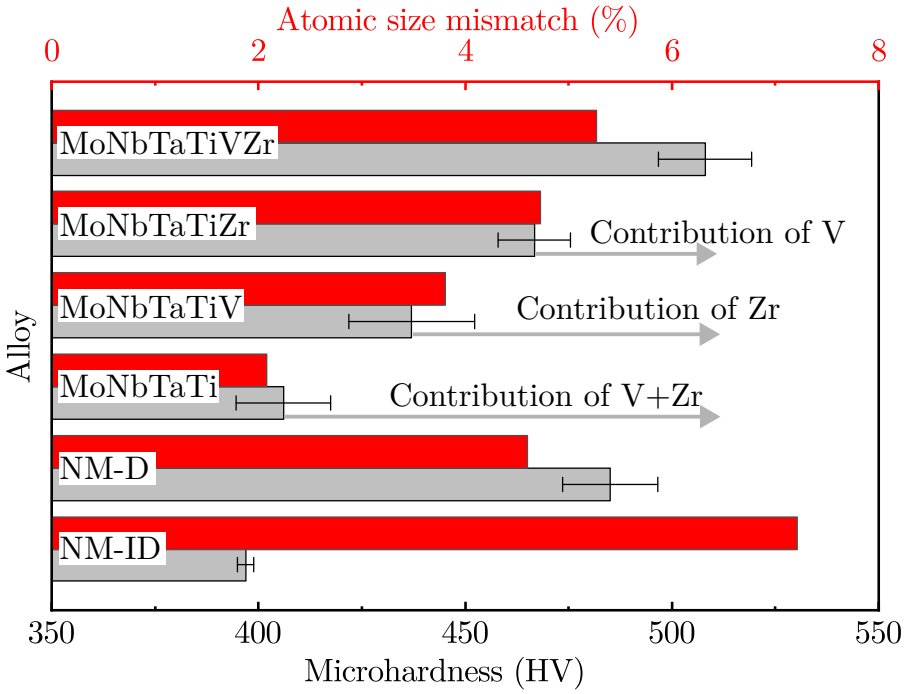

Fig. 4.2: Microhardness and atomic size mismatch of RHEA MoNbTaTiVZr and its subgroup alloys. NM-D and NM-ID stand for the natural-mixing-guided composition of the dendritic and interdendritic region of alloy MoNbTaTiVZr.

The addition of V and Zr to the alloy MoNbTaTi appears to contribute to microhardness, despite the presence of microsegregation. This effect is plausible as the alloying elements are dissolved in both the dendritic and interdendritic regions. Solid-solution hardening in both regions is present, leading to the enhanced microhardness. The increase in microhardness exhibits an almost correlational relationship with atomic size mismatch. However, a unique phenomenon can be observed for the alloy NM-ID, which exhibits a significant atomic size mismatch but a low microhardness. While this indicates the limitation of δ in assessing the solid solution hardening effect, it also points towards the necessity for a more nuanced study on the complex behavior of multi-phase RHEAs.

4.2 Effect of vanadium addition

As described in Chapter 3, the microstructure is tailored through V-addition. The dual-phase dendritic microstructure in the alloy MoNbTaTiZr evolves into a multi-phase dendritic microstructure with V-inclusions in the alloy MoNbTaTiVZr. Hence, this alteration could influence the mechanical properties as well.

Despite the modest increase in microhardness due to the contribution of V compared to that of Zr, the microstructure of the Zr-excluded RHEA MoNbTaTiV deviates significantly from that of the RHEA MoNbTaTiVZr. The alloy MoNbTaTiV exhibits a smaller interdendritic region and larger dendritic arm spacing than those of the alloy MoNbTaTiVZr (see Fig. 3.17 and Fig. 3.3). In contrast, the V-excluded RHEA MoNbTaTiZr possesses a similar microstructure except for the presence of the V-rich inclusions (see Fig. 3.7). Investigating the effect of V-addition enhances the understanding of the role that V-inclusions play in the mechanical properties and helps to establish a relationship between microstructure and mechanical performance. This could facilitate the exploration of the wide range of HEAs and provide insights into optimizing their performance for different applications.

4.2.1 Effect of V on microhardness

The microhardness results of the RHEAs MoNbTaTiV$_x$Zr (V$_x$) at RT are shown in Fig. 4.3. Microhardness increases from 465 HV (V$_0$) to about 500 HV (V$_{0.4}$), followed by an unexpected decrease to 485 HV (V$_{0.6}$), and subsequently rises again to around 500 HV (V$_1$). Notably, the drop in microhardness at V$_{0.6}$ is most likely due to the presence of V-inclusions.

To probe the hardness difference between the phases, the ultra-microhardness (UMH) test is employed. Fig. 4.4a displays UMH indents in the dendritic and interdendritic regions without inclusions, while Fig. 4.4b depicts an indent of the interdendritic region containing V-inclusions.

The edge of the indent in Fig. 4.4b demonstrates that the indenter slides towards the V-inclusions, as marked by arrows. Although it is difficult to obtain an accurate value due to the small size of the V-inclusions, these observations clearly indicate the softness of the inclusions compared to the interdendritic region. In addition, it is worthwhile to mention that the difference between the UMH values of dendritic and interdendritic regions in alloy V$_1$ is not significant. The dendritic region exhibits an UMH of about 467 HV, while the interdendritic region displays a slightly higher value of approximately

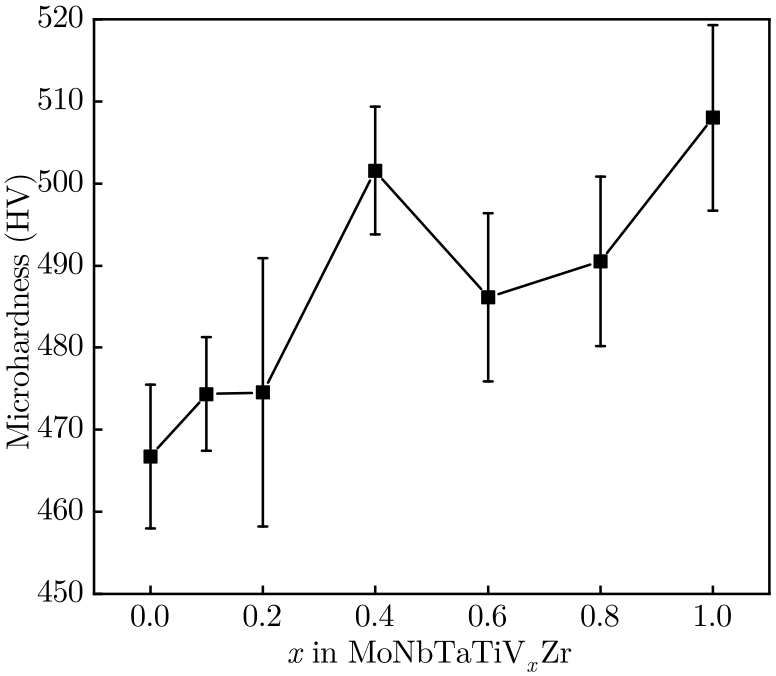

Fig. 4.3: Effect of V-addition on the microhardness of RHEAs MoNbTaTiV$_x$Zr.

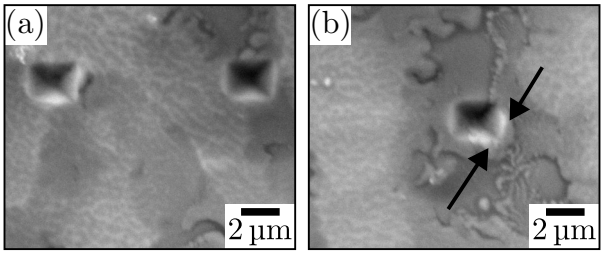

Fig. 4.4: Ultra-microhardness test results for RHEA MoNbTaTiVZr (V_1). (a) Indents in inclusion-free dendritic and interdendritic regions. (b) Indent in the interdendritic region containing V-inclusions.

517 HV. In literature studying alloy V_0, the interdendritic region is also claimed to be harder than the dendritic region [71].

The yield strength of a multi-phase alloy could be estimated by an addition of individual constituent phases' contributions, weighted by their respective volume fractions [72]. The microhardness often shows a linear relationship with yield strength [49]. This correlation is confirmed up to the sub-micron range regardless of the indentation size [73]. Hence, the microhardness H of RHEAs V_x can be approximated as:

$$H \approx f_{\mathrm{D}} H_{\mathrm{D}} + f_{\mathrm{ID}} H_{\mathrm{ID}} + f_{\mathrm{Inc}} H_{\mathrm{Inc}}, \tag{4.1}$$

where f is the volume fraction, and subscripts "D", "ID" and "Inc" stand for dendritic, interdendritic and inclusion, respectively.

It is reasonable to conclude that the presence of soft V-inclusions results in a decrease of microhardness in the alloy $V_{0.6}$. Afterwards, microhardness increases further as V dissolves into both the dendritic and interdendritic regions, causing larger solid solution strengthening, as is the case from V_0 to $V_{0.4}$. This microhardness increase counteracts the drop due to increasing volume fraction of soft V-inclusions, leading to a nearly constant microhardness from $V_{0.6}$ to $V_{0.8}$. Subsequently, V tends to dissolve more into the interdendritic region instead of forming inclusions, leading to a further increase in microhardness from $V_{0.8}$ to V_1, as also suggested by the lattice constant evolution of the interdendritic region (see Fig. 3.10).

4.2.2 Effect of V on hot compression behavior

The compressive stress-strain curves of alloys V_x at 800 °C are shown in Fig. 4.5. All alloys exhibit a strength larger than 900 MPa at 800 °C. The fracture mode of alloys V_0 - $V_{0.4}$ is brittle. Brittle fracture of alloy V_0 at RT has already been reported in [62, 63, 71], and it is still found at 800 °C in the present work. In contrast, an enhanced ductility with strain softening is observed for alloys $V_{0.6}$, $V_{0.8}$ and V_1, which still possess a high yield strength. This improved ductility is related to the V-inclusions. Additionally, serrated flow can be observed, which might be attributed to localized heterogeneous deformation [74].

Fig. 4.6 shows the trends of the 0.2 %-offset yield strength $R_{p0.2}$, ultimate compressive strength R_m and fracture strain ε_f as a function of increasing V-addition x, as derived from the compressive stress-strain curves.

The trends of both strength measures are similar to that of the microhardness shown previously. The solid solution strengthening in BCC RHEAs can be divided into athermal and thermally-activated components [75]. While the athermal component is related to the interaction of dislocation with lattice distortion, the thermally-activated component is associated with the local environment influenced by solutes atoms [76]. This atomic environment generates an energy barrier for the double-kink nucleation and propagation. Thermal energy can overcome this kink-related energy barrier [77], thereby leading to a reduction in strength at elevated temperatures. Therefore, the similar trends of the mechanical properties indicate a comparable strength reduction in all RHEAs V_x due to thermally-activated dislocation slip. This comparable strength reduction also suggests that the explanations for the microhardness changes can also be used to understand the variation of strength at 800 °C with increasing V-addition. In other words, the previously discussed factors such as solid solution strengthening caused by V, the presence of soft V-inclusions, and the balance of these two effects play a similar role. In addition, the

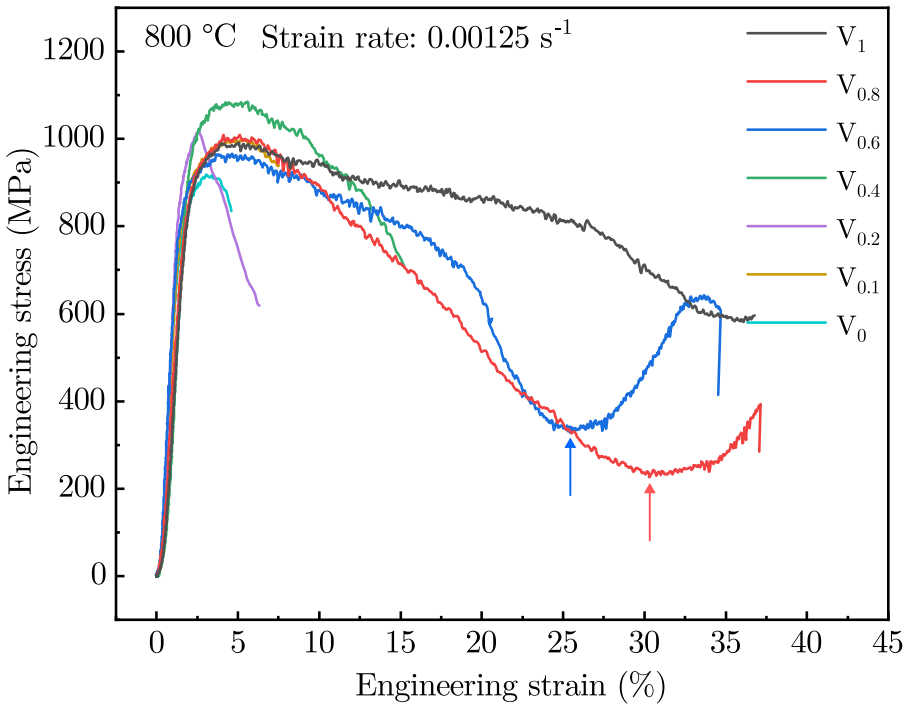

Fig. 4.5: Hot compression curves of RHEAs MoNbTaTiV$_x$Zr (V$_x$) at 800 °C. Points indicating fracture for alloys V$_{0.6}$ and V$_{0.8}$ are marked by arrows.

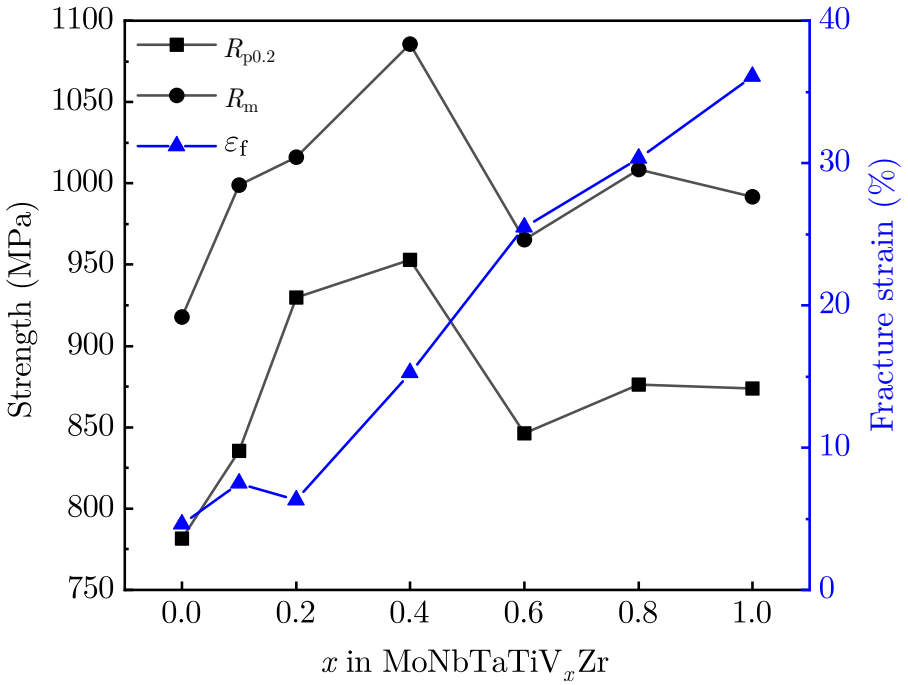

Fig. 4.6: 0.2 %-offset yield strength $R_{p0.2}$, ultimate strength R_m and fracture strain ε_f derived from analysis of compressive stress-strain curves at 800 °C.

similar trends also point to the thermal stability of the microstructure at 800 °C, at least during the hot compression tests.

In comparison to the strength measures, ductility shows an almost consistent increasing tendency. Note that ε_f of the brittle samples V_0 - $V_{0.4}$ are obtained at their fracture point, while that of the ductile samples $V_{0.6}$ - V_1 are defined as the lowest point in the plastic region of the stress-strain curves (marked by arrows in Fig. 4.5). Such a definition of ε_f for the ductile samples is plausible, since alloys $V_{0.6}$ and $V_{0.8}$ exhibit lower ductility compared to alloy V_1. When the strain surpasses the lowest point in the respective stress-strain curves, the samples $V_{0.6}$ and $V_{0.8}$ are already fractured with much less barreling as compared to alloy V_1. The fractured samples come into contact with the opposing punch. Due to their ductility, the fractured parts stick together, preventing the control software of the dilatometer to stop movement of the compression punches automatically as it does in the case of brittle samples. This explains why the stress increases after that point for alloys $V_{0.6}$ and $V_{0.8}$, as the punch compresses the two fractured surfaces. In the case of alloy V_1, the alloy exhibits sufficient ductility to prevent such a phenomenon to occur.

4.2.3 Effect of V on fractography and deformation mechanisms

The enhanced ductility in RHEAs V_x is most likely due to the presence of V-inclusions. However, the specific mechanism behind this improved ductility remains unclear. It is necessary to investigate the fracture appearance and the microstructure after plastic deformation.

Figs. 4.7a-d and 4.7e-h show fracture appearances of the brittle sample V_0 and ductile sample $V_{0.8}$, respectively.

Clear evidence of cleavage can be found in the brittle sample V_0 (indicated by white arrows in Figs. 4.7c and 4.7d). In contrast, a porous structure which is similar to dimples in tensile fracture is found for $V_{0.8}$, see Fig. 4.7g. It is reasonable to conclude that the shear stress during compression (oriented 45° to the compression direction) elongates the structure and results in the formation of dimple-like holes. The enlarged view of such a structure (Fig. 4.7h) indicates that the crack may contain inclusions (marked by red arrows). Note that the fracture surface of alloy V_1 could not be analyzed, as the sample did not fracture when it reached the maximum displacement of 3 mm possible in the dilatometer, which corresponds to a strain of approximately 37.5 % (see Fig. 4.6).

In order to investigate the mechanism of plastic deformation, the deformed sample V_1 is cut using a diamond wire saw (instead of WEDM which can induce thermal effects) and the resulting cross section is investigated using SEM and EDS, see Fig. 4.8. The

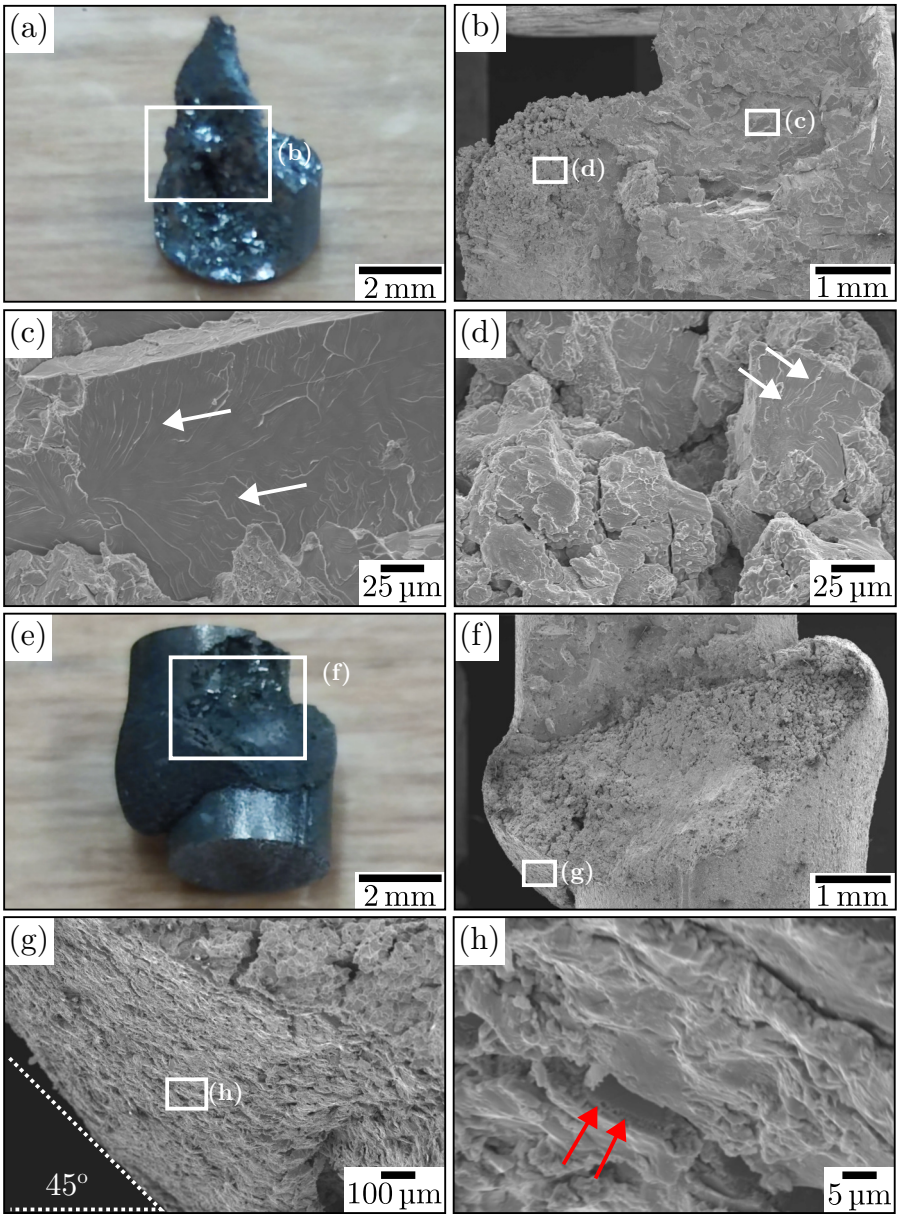

Fig. 4.7: Fractography of (a-d) brittle RHEA MoNbTaTiZr without V-addition (V_0) and (e-h) ductile RHEA $MoNbTaTiV_{0.8}Zr$ ($V_{0.8}$). White arrows in (c) and (d) indicate cleavage. Red arrows in (h) point out inclusions.

overview of the cross section (Fig. 4.8a) shows a non-uniform deformation with barreling of the specimen. This suggests that even after careful grinding of the sample ends, friction between the punch and the samples is still inevitable. However, such a non-uniform strain distribution enables an examination of microstructure evolution with increasing strain in a single sample. The strain distribution in a hot compression sample with barreling can be found in [78]. Fig. 4.8b provides a simplified sketch of this phenomenon. Three zones subjected to moderate (c), high (d) and negligible (e) strain are selected to conduct a systematic study.

At low magnification, the micrographs suggest a realignment of the dendritic microstructure. The dendritic regions in the zones with moderate and high strain are more likely to be perpendicular to the direction of compression (Figs. 4.8c_1 and d_1), while the dendritic region in the zone with negligible strain is more uniformly oriented. At higher magnification, the zone with moderate strain (Fig. 4.8c_2) indicates that the dendritic region is barely deformed. However, the inclusions are refined, specifically near a shear band, as shown in the more enlarged view (Fig. 4.8c_3). This suggests an inhomogeneous strain distribution in the phases. The micrographs captured from the high strain zone (Figs. 4.8d_2 and d_3) indicate a co-deformation of the dendritic region. It is also evident that almost all the inclusions distributed in the interdendritic region are refined. Although most of the fine inclusions have a small size ($< 200\,\mathrm{nm}$), some of them are still discernible in the V mapping result shown in Fig. 4.8d_2. The observed refinement can also be ruled out as being caused by thermal effects in the hot compression test, since the V-inclusions in the zone with negligible deformation (Fig. 4.8e_3) remain coarse and identical to those in the undeformed alloy as shown in Fig. 3.7g. Based on these observations, it is reasonable to conclude that strain localization occurs in the interdendritic region during plastic deformation. Such a strain localization results in plastic deformation dominated by the soft V-inclusions, which clarifies the strain softening observed in the compressive stress-strain curves (Fig. 4.5).

The refinement of the V-inclusions is also observed in EBSD investigations. Figs. 4.9a and b show results from two high-strain zones: zone a, which contains only microcracks, and zone b, which comprises two long cracks. To clearly distinguish the dendritic and the interdendritic regions, their SEM micrographs are also shown and are denoted with the subscript $_1$. The band contrast in Fig. 4.9a_2 indicates weak diffraction signals in the interdendritic region. This is due to a large density of crystal defects which can be attributed to the strain localization in the interdendritic region. This is consistent with the conclusion obtained from the study on the plastic deformation mechanism. The microcracks in Fig. 4.9a (indicated by white arrows) are surrounded by a high density of refined V-inclusions. The band contrast of the zone containing cracks (Fig. 4.9b_2)

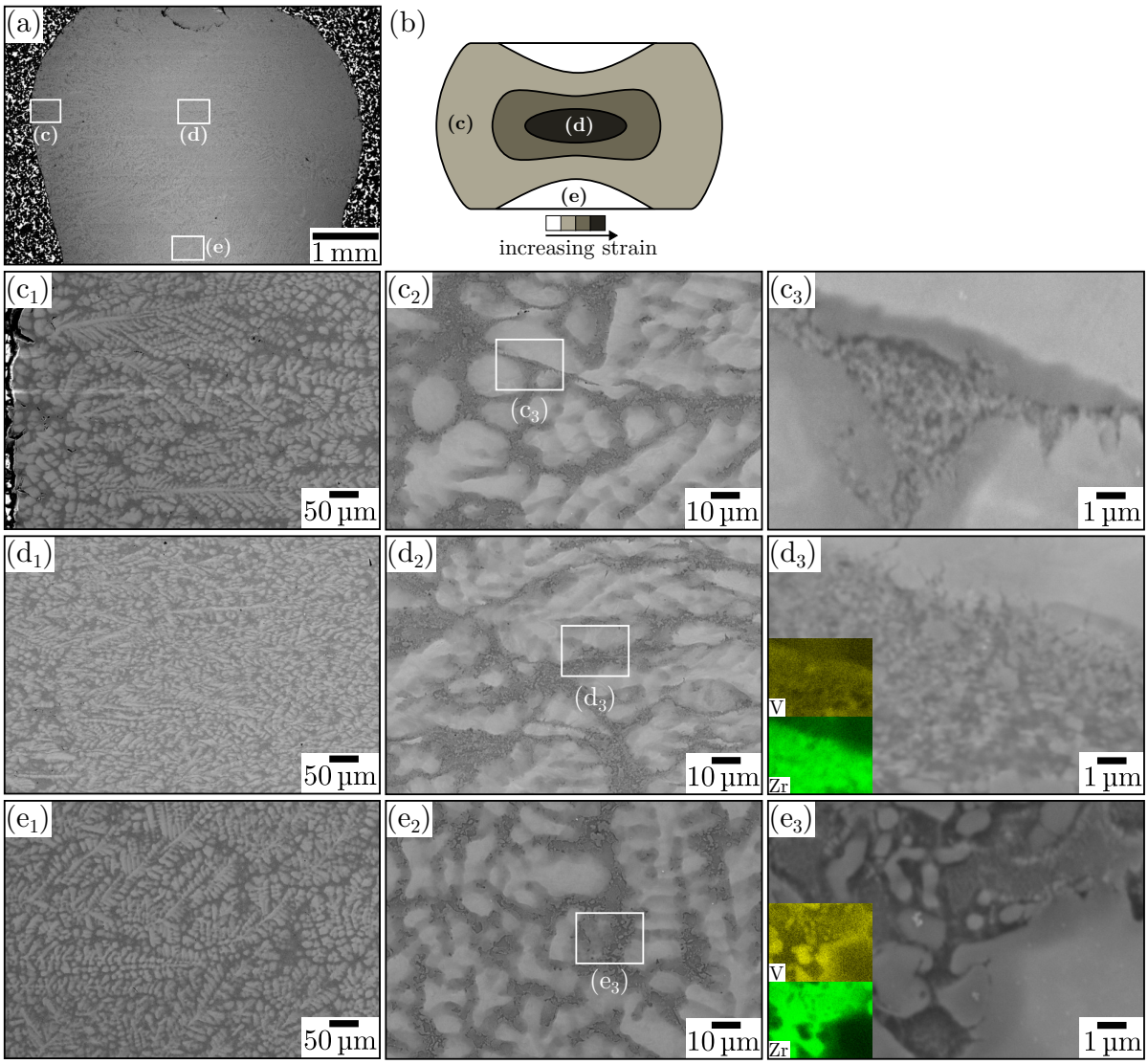

Fig. 4.8: SEM and EDS investigations on the deformation mechanism of the deformed RHEA MoNbTaTiVZr (V_1): (a) an overview of the cross section, (b) a simplified illustration of the strain distribution in compression with barreling of the sample, after [78]; Micrographs of the zones subjected to moderate (c), high (d) and negligible strain (e), with subscripts indicating their magnification: $_1$ low , $_2$ intermediate and $_3$ high. In d_3 and e_3, V and Zr EDS-mapping results are also shown.

also indicates a large amount of defects near the crack, which shows a zigzag pattern originating from the point of initiation. The crack appears to be halted within the interdendritic region, as indicated by red arrows. The inverse pole figure in Fig. 4.9b$_3$ reveals the presence of small V-inclusions at the arrest point of the crack, with red lines outlining the shape of the crack. Hence, the fine and soft V-inclusions distributed in the interdendritic region increase the size of the plastic zone around a crack tip and impede crack propagation, and an enhanced ductility is achieved. In contrast, Fig. 4.9c shows a straight crack in the brittle alloy $V_{0.1}$. This observation highlights the beneficial effect of the refined V-inclusions, which are able to impede crack propagation, leading to the transformation of a straight into a branched crack.

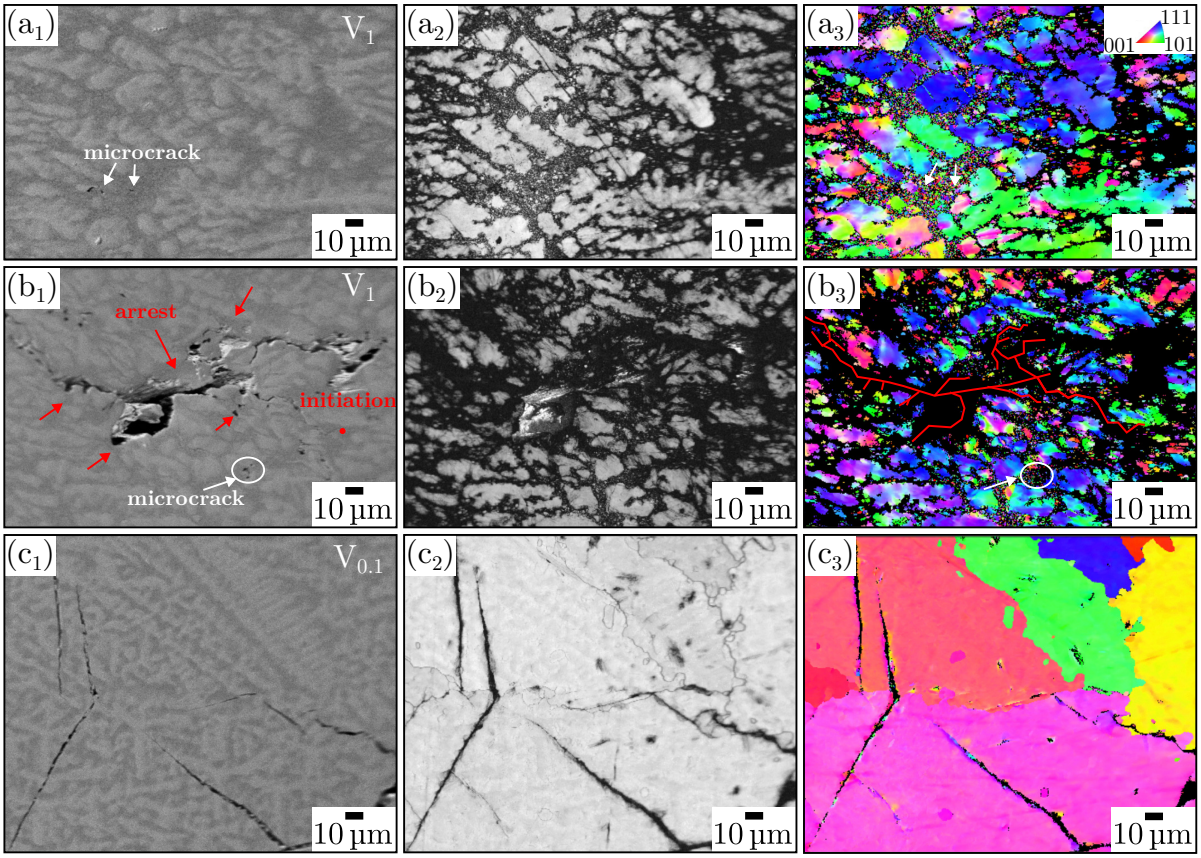

Fig. 4.9: EBSD investigations after deformation. (a-b) Ductile RHEA MoNbTaTiVZr (V_1) and (c) brittle RHEA MoNbTaTi$V_{0.1}$Zr ($V_{0.1}$). (a) shows the region with the largest strain and (b) illustrates a region with both large strain and cracks. Subscripts in the subfigures: $_1$ for SEM micrographs, $_2$ for band contrast and $_3$ for inverse pole figure (IPF).

4.3 Effect of heat treatment

The mechanical properties of the RHEA MoNbTaTiVZr benefit from a combination of dendritic microstructure and V-inclusions. However, it is important to note that during compression testing, the samples are subjected to a short duration at high temperatures. Given the maximum displacement of 3 mm in the dilatometer, the longest exposure time at the testing temperature is limited to six minutes, including one minute of hold time and five minutes of deformation. Although the literature often suggests that the dendritic microstructure of RHEAs is stable [17, 18], the short testing duration raises questions regarding the stability of microstructure after prolonged heat treatments. Moreover, exploring the possibility for homogenizing the microsegregation through heat treatment remains an important question to address.

Isochronal heat treatments of RHEA MoNbTaTiVZr are conducted at 800, 1000, 1100, 1200, 1300, and 1400 °C for 12 hours, followed by furnace cooling. The SEM micrographs of the heat treated samples are shown in Fig. 4.10. The characteristic microstructure (dendritic + inclusions) appears to be stable up to at least 1100 °C, although the dendritic region coarsens due to diffusion at this temperature. A further temperature increase to 1200 or 1300 °C makes the dendritic microstructure barely recognizable. The dendritic region continues to grow and reduces the size of the interdendritic region. Few interdendritic regions at 1200 °C contain rod-like inclusions, which almost vanish at 1300 °C. Based on the results obtained for 1200 and 1300 °C, it would be expected that the microstructure might become homogenized after a heat treatment at 1400 °C. However, the micrograph shows that the dendritic microstructure is even more pronounced compared to that for 1300 °C. In part of the interdendritic regions, inclusions are also observed.

The chemical compositions of the dendritic and interdendritic regions after heat treatments are shown in the left and right parts of Fig. 4.11, respectively. The results of the as-cast (AC) state are also included at the very left of the figure for comparison. These results are obtained using EDS point analysis, with each value representing the average of five measurements.

In the dendritic region, the chemical composition is stable up to 1000 °C, with minor variations at 1100 °C. From 1200 °C onwards, the elemental concentrations of all elements except Zr appear to equalize. This indicates that the elements Mo, Nb, Ta, Ti and V diffuse from the interdendritic to the dendritic region, as also proved by their concentration decrease in the interdendritic region. An unexpected increase in the Zr concentration of the interdendritic region is observed, reaching 90 % at 1300 °C. At 1300 and 1400 °C, the interdendritic region shows the dominance of Zr and Ti in chemical composition. While

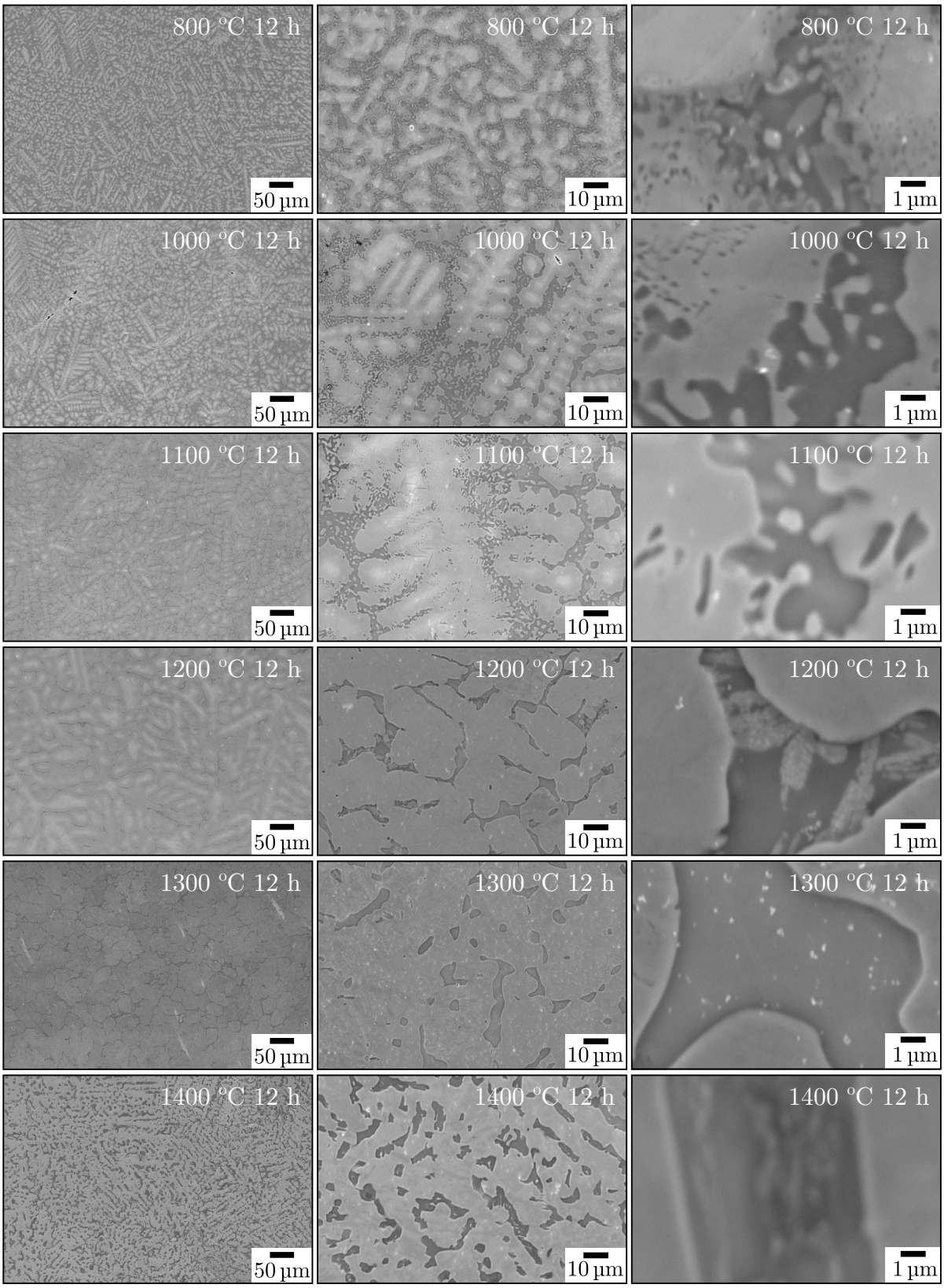

Fig. 4.10: SEM micrographs of the RHEA MoNbTaTiVZr after 12 hours of isochronal heat treatments at 800, 1000, 1100, 1200, 1300 and 1400 °C.

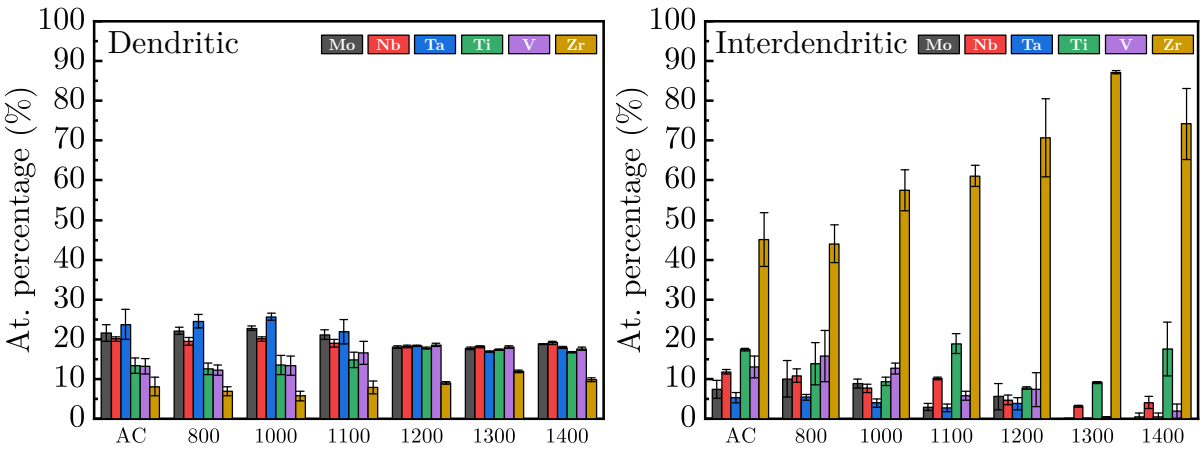

Fig. 4.11: EDS quantitative results for the RHEA MoNbTaTiVZr after 12-hour heat treatments at 800, 1000, 1100, 1200, 1300 and 1400 °C in comparison with the as-cast (AC) state.

this indicates the challenge of homogenizing RHEAs containing Zr-rich interdendritic regions through heat treatment, the result might also suggest possible oxidation. The Zr concentration in the dendritic region after heat treatment above 1200 °C could be unreliable. In practice, the EDS software does not detect the presence of Zr, and the values are obtained by assuming that Zr exists. As the characteristic energies of Zr and Nb are similar to each other, this could lead to potential discrepancies. Note that the results in Figs. 4.10 and 4.11 do not indicate an evolution of microstructure, but show an influence of temperature on the diffusion during heat treatment.

The microstructure after long-term heat treatment is not identical to that of the as-cast state, which could also influence the compression behavior. The assumption is made that samples undergoing a 12-hour heat treatment at 800, 1000, and 1100 °C would yield similar compression behavior, just as those treated at 1200, 1300, and 1400 °C are expected to. Due to the limited time available for the present study, a systematic investigation is not possible. Instead, two selected heat-treated samples are studied in compression tests, namely HT800 and HT1400. Their compressive stress-strain curves at 800 °C are shown in Fig. 4.12. The test conditions are the same as those for the as-cast samples shown before.

As expected, the ductility is retained in HT800 but disappears in HT1400. Furthermore, a significant increase in strength is observed for HT1400, which is most likely due to the presence of oxides. The change in mechanical properties for HT1400 is plausible, as the V-inclusions responsible for ductility are not present. However, a decrease of strength is found in HT800. The softening behavior is less pronounced than that in the as-cast state. It is hypothesized that the local areas of microstructure might have changed in

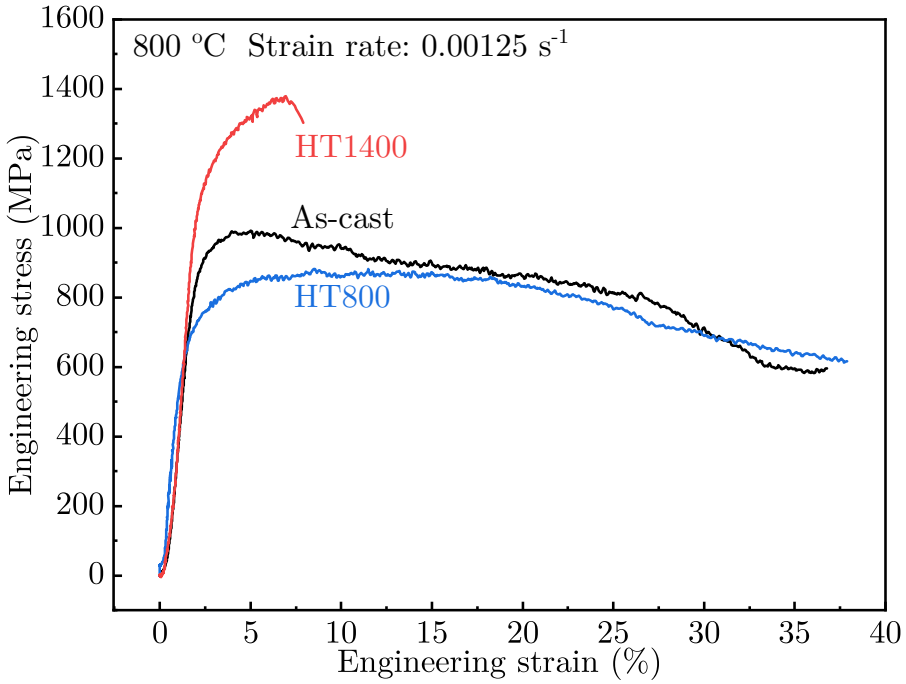

Fig. 4.12: Compressive stress-strain curves of RHEA MoNbTaTiVZr after a 12-hour heat treatment at 800 °C (HT800) and at 1400 °C (HT1400) in comparison to the as-cast state.

the interdendrtic region during the heat treatment, such as a relaxation of the intrinsic residual strain caused by the large atomic radii mismatch [79]. This could be a potential explanation for the drop of yield strength in HT800, as V and Zr, respectively, are the smallest and largest atoms in the present RHEA. However, a more thorough study is necessary for clarification. Due to the time constraints of this dissertation, it is not addressed in the current work.

The sample HT1400 is characterized using EDS-mapping, see the left panel of Fig. 4.13. Clear evidence of oxidation in the Zr-rich region can be found. Interestingly, the oxidation can even be found in the center of the cylindrical sample, which is 2 mm away from the surface. Unlike forming a dense oxide layer on the surface, the oxides appear to disperse in the dendritic matrix. It is assumed that the alloy fabricated using arc-melting contain pores, which provide a path for oxygen to diffuse into the center of the bulk sample. It can be concluded that the vacuum quality (about 2 Pa) is insufficient to prevent oxidation during the heat treatment of the present RHEA. This technical limitation leads to oxidation, attributed to the presence of oxygen-reactive elements such as Zr and Ti. The oxidizing atmosphere could have potentially affected the actual chemical potential of these elements in the dendritic and interdendritic region, thereby preventing the homogenization of the RHEA.

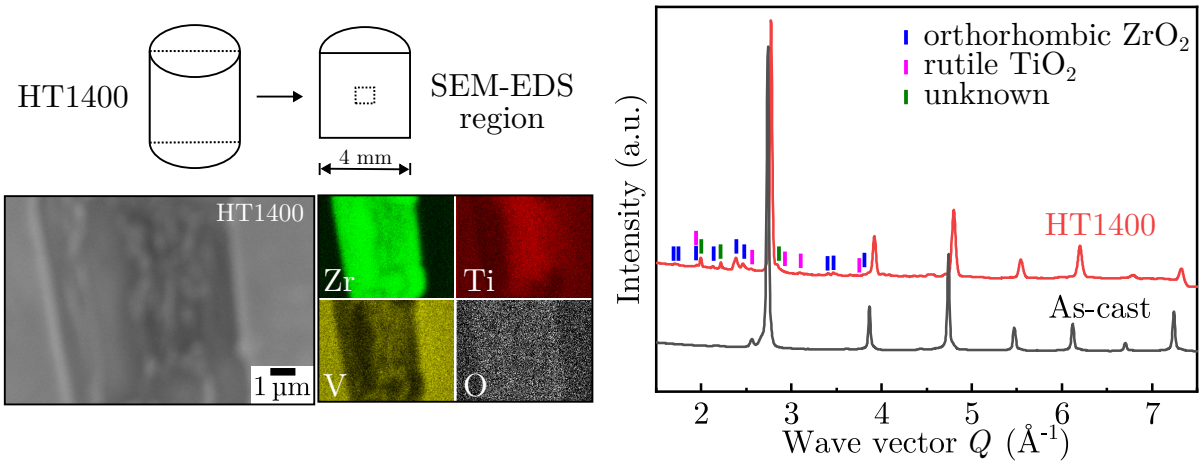

Fig. 4.13: Evidence of oxidation in RHEA MoNbTaTiVZr after a 12-hour heat treatment at 1400 °C (HT1400). The region for EDS-mapping and the mapping results for Zr, V, Ti, and O elements (left) and HEXRD pattern in comparison to as-cast state.

The presence of oxides is also confirmed in the HEXRD pattern, see the right panel of Fig. 4.13. These oxides are identified as orthorhombic ZrO_2 and rutile TiO_2. While the typical crystal structures for ZrO_2 are monoclinic, tetragonal, and cubic, orthorhombic ZrO_2 has been reported to form under high pressure [80]. However, the reason for its appearance remains unclear and is not addressed in the present dissertation.

The peaks corresponding to the V-inclusions and the asymmetry attributed to the interdendritic region have disappeared. This observation confirms the conclusions drawn from the microstructure studies in Chapter 3. Moreover, the peaks of the major BCC phase show a shift to a larger wave vector, thus a smaller lattice constant. This points out that the EDS results of Zr in the dendritic region after heat treatments might be unreliable (see Fig. 4.11), as an increase in Zr concentration should lead to a larger lattice constant.

In summary, the results in this section demonstrate the thermal stability of the microstructure at 800 °C, while also clearly revealing the difficulty of homogenization through heat treatments.

4.4 Concluding remarks

The RHEA MoNbTaTiVZr exhibits a combination of high strength and ductility, particularly at 800 °C. A hyperbolic relation between the 0.2 %-offset yield strength and the fracture strain at 800 °C is shown in Fig. 4.14, which allows a comparison of the alloy MoNbTaTiVZr with other RHEAs and traditional alloys [13, 18, 81–85].

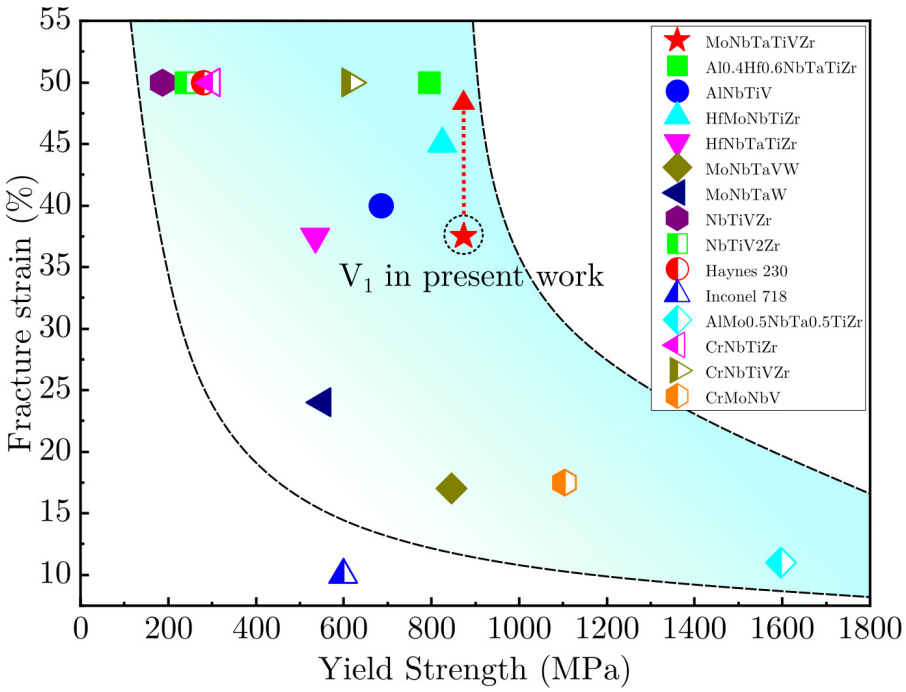

Fig. 4.14: 0.2 %-offset yield strength-fracture strain plot of RHEA MoNbTaTiVZr (V_1) in comparison with other RHEAs and traditional alloys at 800 °C [13, 18, 81–85]. The actual position of V_1 could be in the direction indicated by the dashed red arrow.

Note that the actual fracture strain of alloy most likely exceeds 37.5 % (see dashed red arrow), as this is the maximum strain achieved in the present study. Even though the compressive behavior of the RHEA at RT is not investigated in this study, the results clearly point out that the alloy exhibits improved mechanical properties at elevated temperatures. This is particularly significant for RHEAs, which are specifically designed for high-temperature applications.

Chapter 5

High-pressure torsion

The previous two chapters are devoted to analyzing the microstructure and mechanical properties of the initial state before HPT processing. This chapter addresses their evolution during HPT. For this purpose, a systematic investigation of the microhardness and microstructural evolution with increasing applied strain is conducted. In addition, considering the challenges in eliminating the microsegregation through composition modification and heat treatment, this chapter explores the potential of this severe plastic deformation technique to homogenize the present RHEA.
This chapter begins with an illustration of the microhardness evolution, followed by a thorough examination of the microstructure to enhance understanding of the relationship between the characteristic microstructure and its microhardness. From these findings, the deformation process can be separated into different stages, with corresponding observations and implications discussed for each stage.

5.1 Microhardness evolution

Fig. 5.1 shows the microhardness evolution with increasing applied strain. The values are obtained by averaging five measurements taken on the surface defined by the axial and the radial directions (see Fig. 2.4). When the strain is small, microhardness increases rapidly to about 525 HV. This might be due to the deformation by compression in HPT to allow for the required shear strain. Subsequent shearing leads to a gradual increase to the first saturation of about 550 HV at a strain of around 70. Thereafter, the microhardness shows a drastic increase to about 625 HV at a strain of about 100, followed by a slow increase and a tendency to saturate at about 675 HV at a strain of $\varepsilon \sim 400$.
The first saturation stage becomes more obvious when the applied strain is plotted on a logarithmic scale, as shown in Fig. 5.2. For single-phase materials, a saturation of

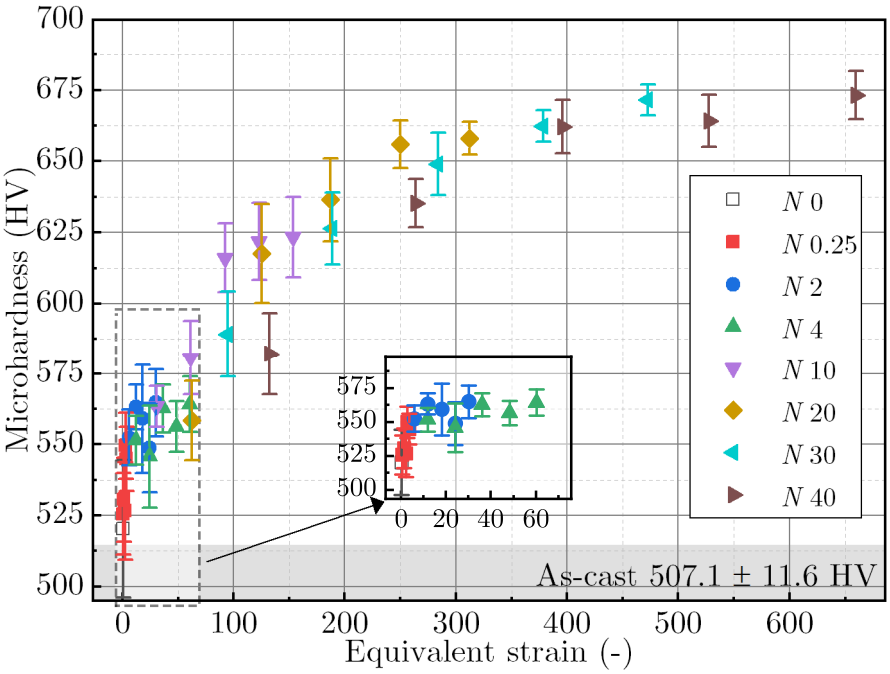

Fig. 5.1: Microhardness evolution during HPT processing. The inset shows a detailed view up to the strain of about 70.

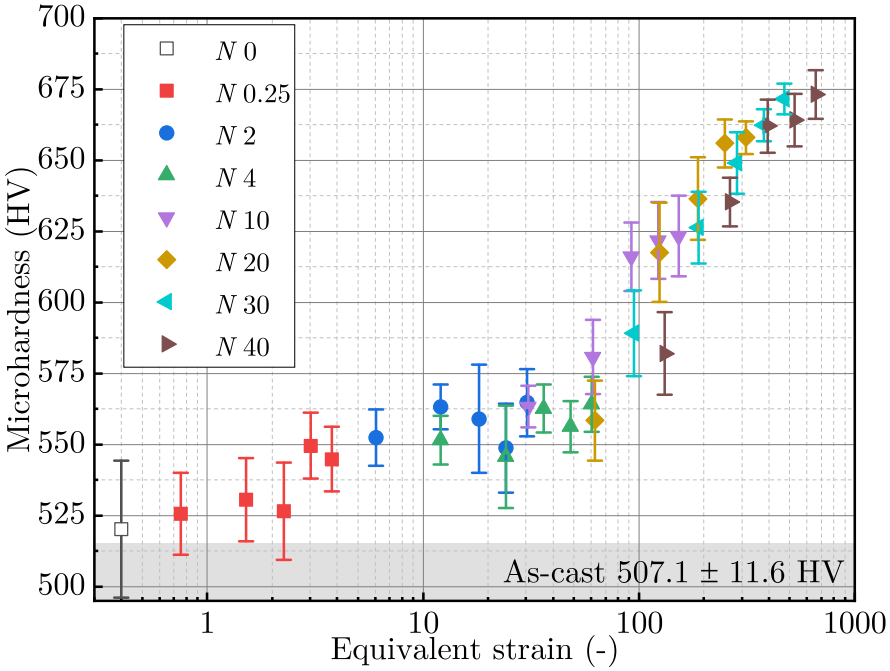

Fig. 5.2: Microhardness evolution with strain plotted on a logarithmic scale.

microhardness and grain refinement into nanoscale is often observed up to a strain of about 20 [32], which corresponds approximately to the strain value near the periphery of $N2$. It should also be noted that the increase in microhardness is less significant

compared to that in single-phase alloys processed by HPT. For instance, the Cantor-alloy, CoCrFeMnNi, exhibits an increase in microhardness from about 150 (as-cast) to a saturation plateau of 500 HV at a strain of about 20 [24]. The present work shows a much smaller increase in microhardness (50 HV) at $\varepsilon \sim 20$. In addition, it is not typical to observe two instances of saturation of microhardness in succession in single-phase HPT-processed materials.

Apart from the saturation regimes, a large deviation in the microhardness of $N0$ (as-compressed) is observed. In fact, the microhardness values of $N0$ exhibit a markedly non-uniform distribution (see its large error bar in Fig. 5.2). This could be attributed to the inhomogeneous deformation during compression, as the material outward flow in the quasi-constrained HPT processing occurs at the periphery of the HPT-disk. Similar results can be found in [24].

The modest slope of microhardness increase up to a strain of $\varepsilon \sim 70$ may suggest the occurrence of an interesting phenomenon related to a uniform distribution of strain, hence emphasizing the need for a detailed study, which will be undertaken in Section 5.3.1.

5.2 Microstructure evolution

SEM

The microstructure evolution is first characterized using SEM, see Fig. 5.3. Similar to that in previous chapters, the micrographs are obtained from a combination of secondary and backscattered electrons to simultaneously contrast the V-inclusions and to distinguish between dendritic and interdendritic regions. The shearing direction in all subfigures of Fig. 5.3 is horizontal, as indicated by the black arrow.

As the shear strain increases, a slightly deformed dendritic microstructure (Fig. 5.3a) transforms into a lamellar microstructure with elongated dendritic and interdendritic regions (Fig. 5.3b) at $\varepsilon \sim 18$. Such a lamellar microstructure fragments and becomes thinner with further increasing strain. The lamella thickness reduces from $\sim 10\,\mu m$ at the strain of $\varepsilon \sim 18$ to about 1 µm at the strain of $\varepsilon \sim 92$, resulting in the formation of a fragmented vortex microstructure, see Figs. 5.3b-d. The vortex microstructure further develops into a continuous stripe-like pattern when the strain increases to 192 (Fig. 5.3e). A homogeneous microstructure can be found at a strain of $\varepsilon \sim 396$ (Fig. 5.3f). Fig. 5.3g provides an overview of the evolution from the fragmented vortex to the stripe-like microstructure at $\varepsilon \sim 120$ to 200. Note that the micrographs of Figs. 5.3a-f are captured at $r = 1.5\,mm$ for $N0.25$, $N2$, $N4$, $N10$, $N20$ and $N40$, respectively. Fig. 5.3g is obtained by combining five micrographs along the radius of specimen $N20$ at about $r = 1$ - $1.5\,mm$.

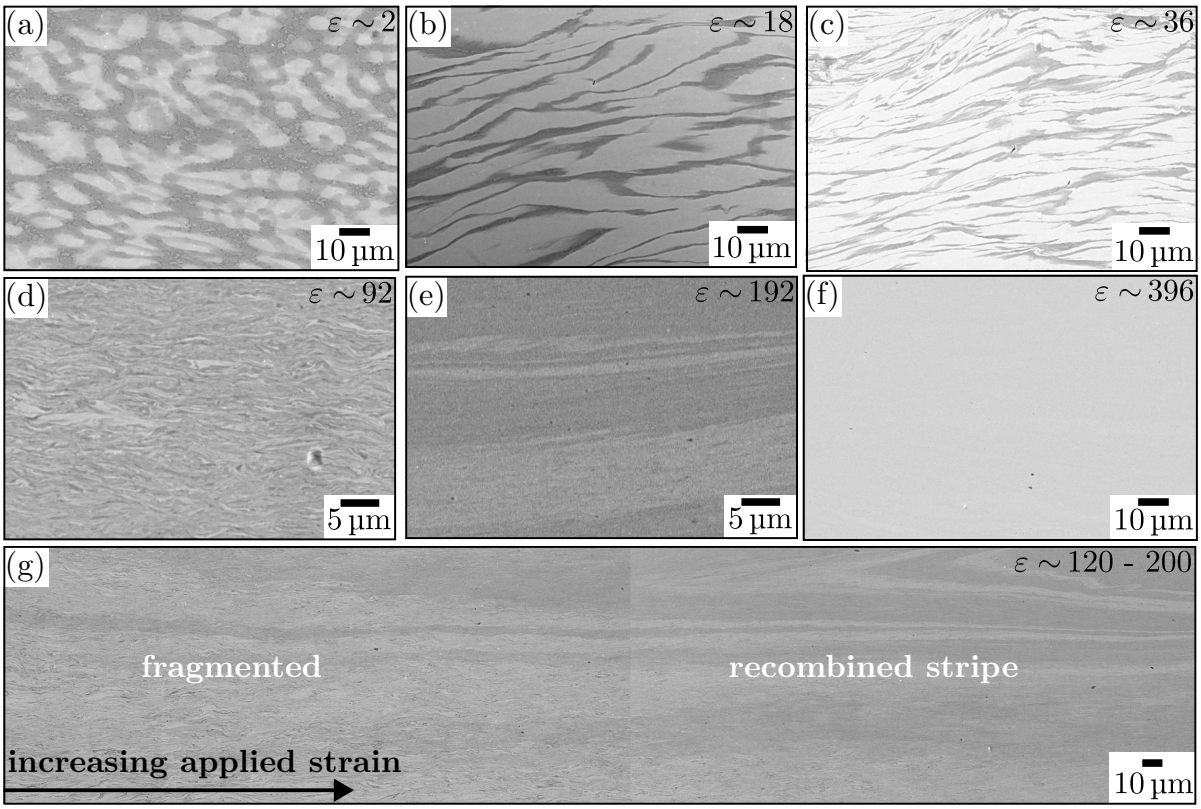

Fig. 5.3: SEM micrographs at $\varepsilon \sim$ (a) 2, (b) 18, (c) 36, (d) 92, (e) 192, (f) 396 and (g) 120 - 200.

Tab. 5.1: Microhardness H (HV) of the microstructures shown in Figs. 5.3a-f.

ε (-)	~ 2	~ 18	~ 36	~ 92	~ 192	~ 396
H (HV)	526.6 ± 17.1	559.1 ± 19.1	562.6 ± 8.5	616.1 ± 11.9	635.7 ± 6.1	662.1 ± 9.4

The microhardness values corresponding to the characteristic microstructures of Figs. 5.3a-f are listed in Tab. 5.1. Microhardness increases by 50 HV, while the microstructure evolves from dendritic to elongated lamella. The microhardness remains nearly constant during the elongation process of the dendritic microstructure until fragmentation begins. This fragmentation results in an increase in microhardness from around 560 HV to about 615 HV at $\varepsilon \sim 92$. The stripe-like microstructure, observed at $\varepsilon \sim 192$, exhibits a microhardness of approximately 635 HV, which is about 3 % higher compared to that at $\varepsilon \sim 92$. As the microstructure becomes chemically homogeneous, microhardness reaches a saturation point.

XRD

To examine the phase evolution during HPT, XRD patterns are measured at varied applied strains ε, see Fig. 5.4a. The XRD pattern for $\varepsilon = 0$, corresponding to the

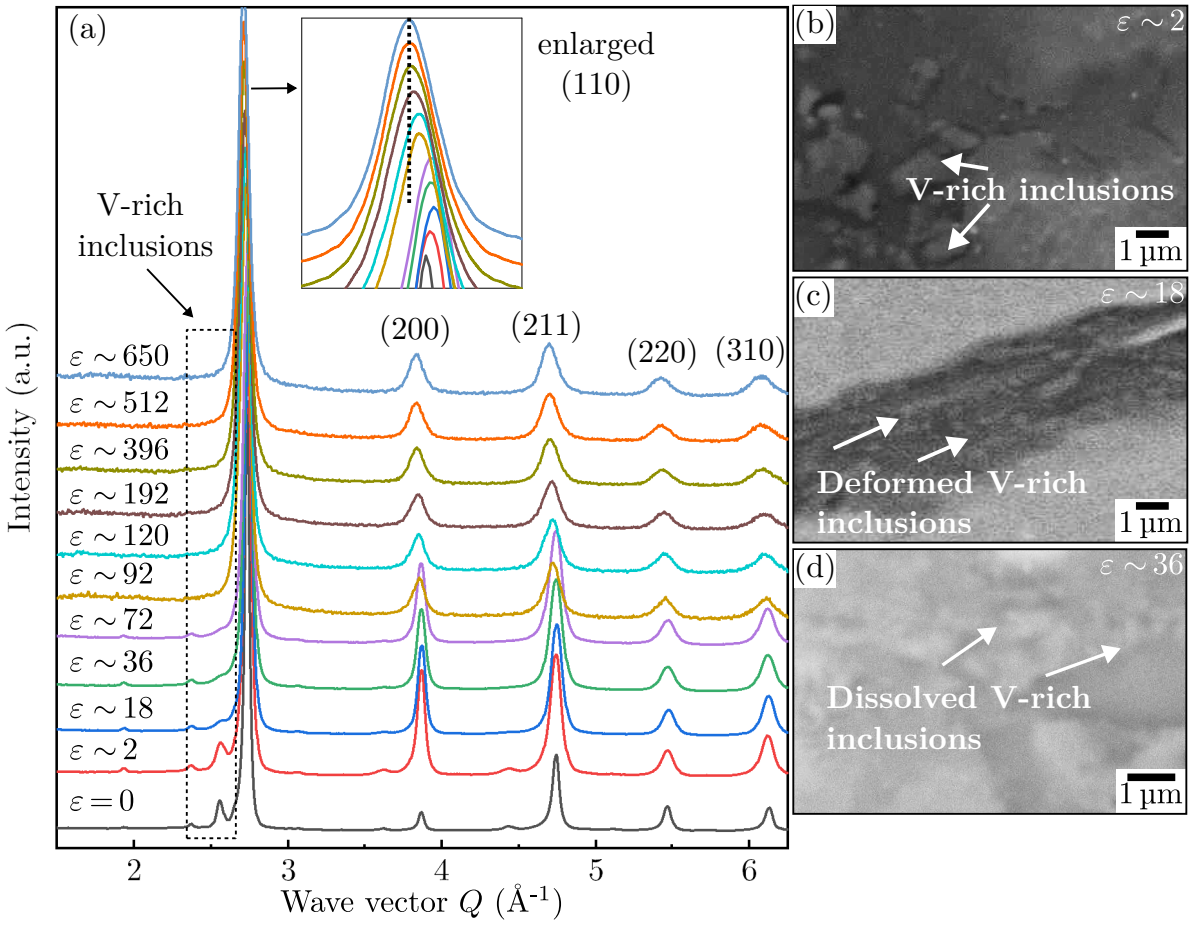

Fig. 5.4: (a) Evolution of the XRD pattern with increasing strain. (b-d) SEM micrographs show the deformation and dissolution of the V-rich inclusions.

result obtained from specimen $N0$, is presented for comparison to exclude the effect of compression on the patterns.

Throughout HPT, the major BCC peaks are consistently present, while the minor peaks representing V-rich inclusions gradually disappear. Additionally, the major BCC peaks initially broaden when the strain increases from 0 to 2, but no significant broadening occurs from $\varepsilon \sim 2$ to $\varepsilon \sim 36$. In this strain range, however, a severe broadening of the peak of the V-inclusions can be found, indicating large deformation of the inclusions, as confirmed by high magnification SEM micrographs (see Figs. 5.4b-d). The peaks representing V-rich inclusions nearly vanish after ε increases to 72, indicative for their dissolution. As ε increases from 72 to 92, a pronounced peak broadening of the major BCC peaks and the disappearance of the V-rich inclusions can be observed. No further pronounced broadening is seen up to $\varepsilon \sim 650$. Note that the XRD patterns from $\varepsilon \sim 92$ onward are measured using CuKα radiation due to limited synchrotron X-ray beam time. Despite this limitation, XRD with CuKα radiation has been shown to effectively resolve

the broadening effect and dissolution of V-rich inclusions at strains smaller than 92 (see Appendix A).
The inset of Fig. 5.4a shows the shift of the (110)-peak of the major phase. A slight peak shift to larger wave vectors Q is observed up to $\varepsilon \sim 18$, followed by a shift to smaller Q-values up to $\varepsilon \sim 650$. This peak shift points out a decrease in the lattice parameter up to $\varepsilon \sim 18$ and a subsequent increase up to $\varepsilon \sim 396$. Interestingly, a shift in the (110)-peak is observed after the applied strain ε reaches 120 and 192, at which the V-rich inclusions disappear and only fragmented dendritic and interdendritic regions remain. This is most likely due to the dissolution of the Zr-rich interdendritic region, which has been identified as reason for an asymmetry of the diffraction peaks. The quantification of the peak shift, which results from the evolution of the lattice parameter, will be addressed in Section 5.3.2.

EBSD

EBSD investigations are conducted to study the grain refinement during HPT, see Fig. 5.5. To distinguish the dendritic and interdendritic regions, the SEM micrographs of the investigated areas are shown, denoted with the subscript $_1$.
The interdendritic regions contain a large amount of crystal defects, leading to a significant extent of unresolved areas. These unresolved areas are shown in black in both band contrast ($_2$) and IPF images ($_3$). Notably, Fig. 5.5a indicates that interdendritic regions are already partially unresolved in the as-compressed specimen. At small strains, $\varepsilon \sim 2$ and 4, the unresolved areas are also observed in the interdendritic regions, while the dendritic regions remain mostly resolved (Figs. 5.5b and c). At $\varepsilon \sim 12$, both the dendritic and interdendritic regions become partially unresolved, with the latter almost entirely unresolved. Few exceptions related to the deformed V-inclusions are noted (Fig. 5.5d). As the strain increases to ~ 24, the unresolved area in the dendritic regions expands (Fig. 5.5e). Meanwhile, the few resolvable areas in the interdendritic regions gradually disappear, coinciding with the apparent dissolution of V-inclusions. It should be noted that the magnification of Figs. 5.5d and e are larger to reveal the grain refinement more clearly. It is observed that the coarse grain (about 100 µm) of the as-cast state remains unrefined up to $\varepsilon \sim 4$. Subsequent deformation results in a grain refinement to approximately 2 µm at $\varepsilon \sim 24$. Rather than a drastic increase in microhardness in this strain range, a plateau as the result of the first saturation is observed (Fig. 5.1). This discrepancy could potentially stem from the fact that the EBSD results are obtained in the axial direction (see Fig. 2.4), where the sample might undergo a larger strain due to contact with the HPT anvils. From $\varepsilon \sim 48$ onwards, almost the entire region (over 98 %)

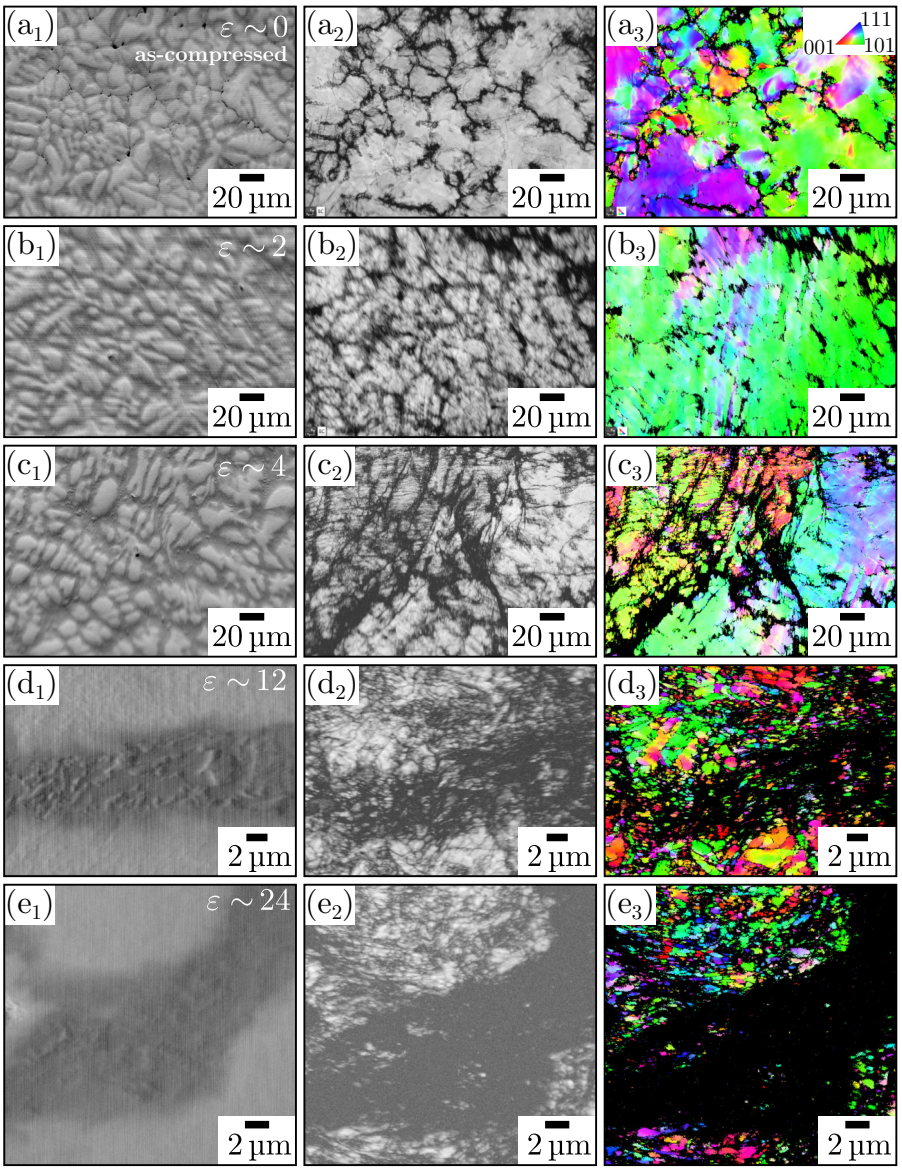

Fig. 5.5: EBSD investigations at $\varepsilon \sim$ (a) 0 (as-compressed), (b) 2, (c) 4, (d) 12 and (e) 24. Subscripts $_1$ for SEM micrographs, $_2$ for band contrast and $_3$ for inverse pole figure (IPF). Obtained in axial direction. Partially after [56].

cannot be resolved by EBSD. Although these results are obtained in the axial direction, investigations in the tangential direction at $\varepsilon \sim 48$ similarly yields a high percentage of unresolved areas.

The percentage of unresolved areas is plotted as a function of strain in Fig. 5.6. The results for the dendritic and interdendritic regions are obtained using the area calculation function in the software ImageJ [50]. Although the detected areas at $\varepsilon \sim 12$ and 24 are smaller than those at $\varepsilon \sim 0$, 2 and 4, the plot provides a rough estimate of the increase in crystal defects in both dendritic and interdendritic regions.

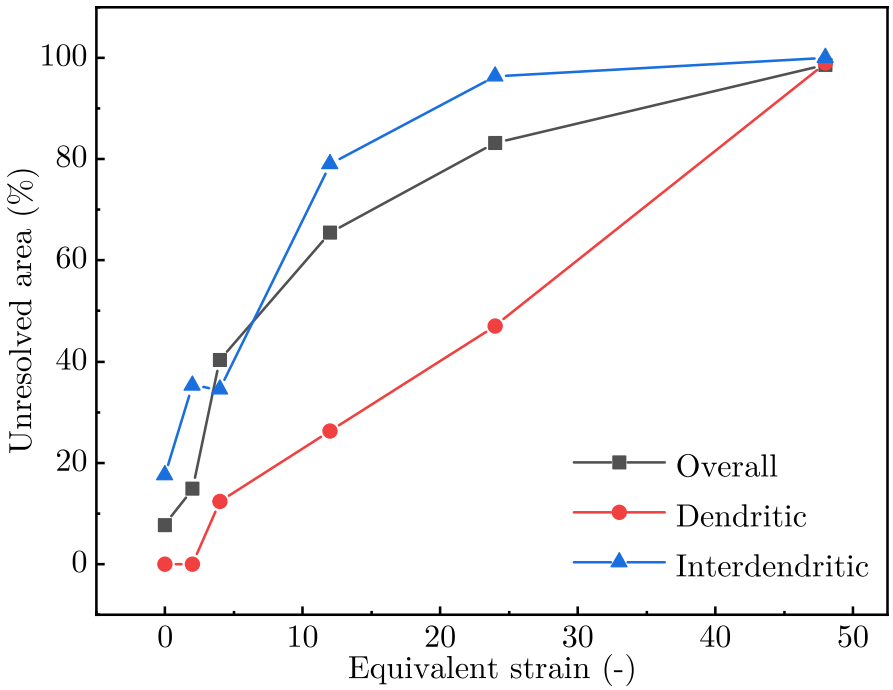

Fig. 5.6: Percentage of the unresolved area in EBSD measurements. Modified after [56].

The accumulation of crystal defects initially occurs in the interdendritic regions, with the dendritic regions showing a delayed increase. It seems reasonable to conclude that the strain localization, previously observed in the interdendritic region during hot compression tests, also occurs during severe plastic deformation at RT. The inability to resolve EBSD patterns at strains larger than 48, along with the discrepancy between grain refinement and microhardness evolution, indicates the limitations of this technique in characterizing severely deformed multi-phase RHEAs. These findings emphasize the need for TEM characterization.

TEM

TEM results at $\varepsilon \sim 2$, 18, 36, 92 and 396 are shown in Fig. 5.7. The FIB lift-outs are obtained from specimens $N0.25$, $N2$, $N4$, $N10$ and $N40$ at a radial distance of 1.5 mm. All bright field (BF) TEM micrographs display a strong contrast, which is related to the high density of defects such as dislocations and grain boundaries. The intense dark contrast in Fig. 5.7a$_1$ is further enhanced by the pronounced Bragg crystallographic orientation contrast. The corresponding selected area electron diffraction (SAED) pattern in Fig. 5.7a$_2$ shows a typical BCC spot pattern. Both the scanning transmission electron microscopy (STEM) BF image (Fig. 5.7a$_4$) and the annular dark-field (ADF) image (Fig. 5.7a$_5$) distinctly show the dendritic/interdendritic regions. As strain increases to

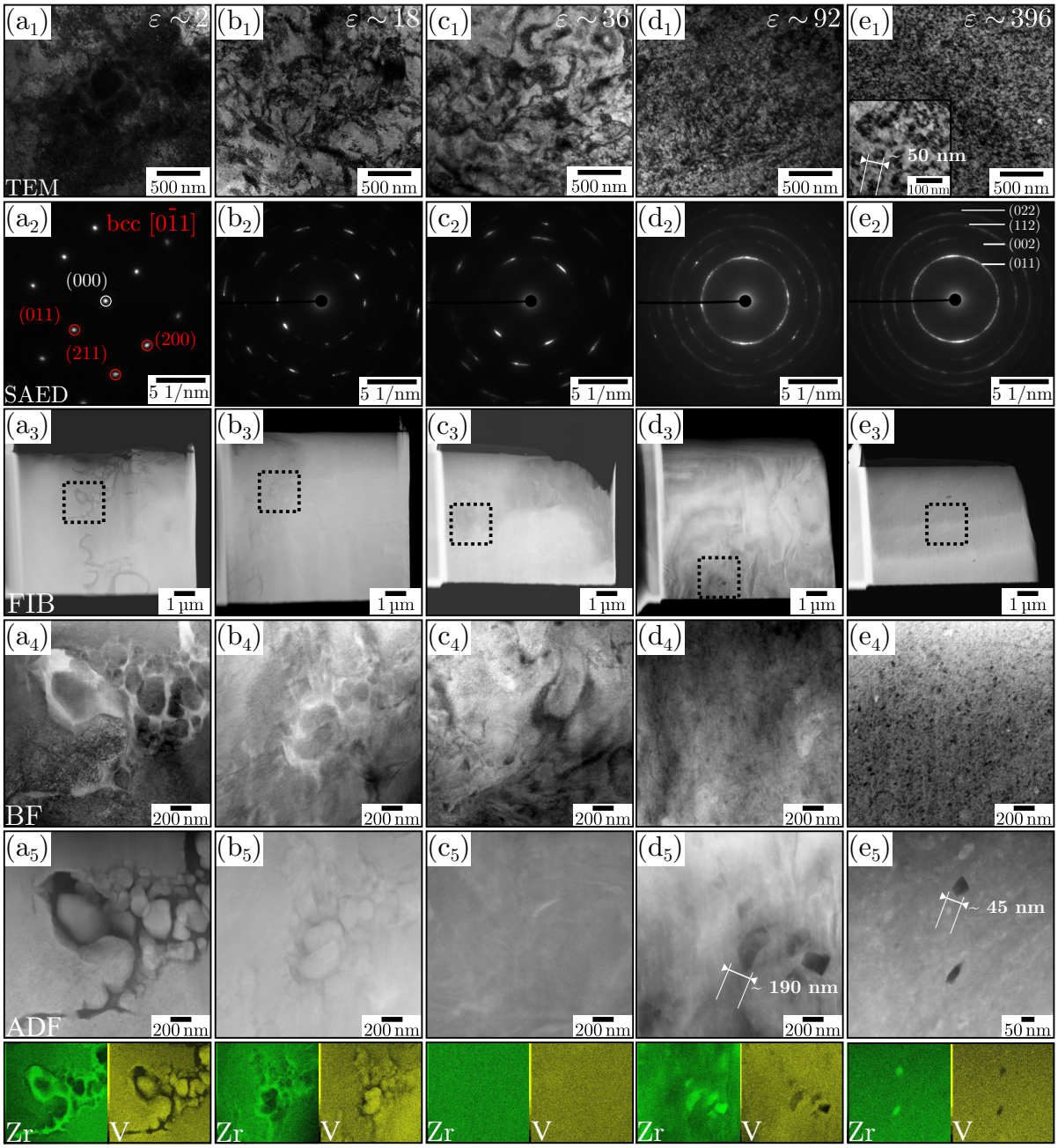

Fig. 5.7: TEM investigations at $\varepsilon \sim$ (a) 2, (b) 18, (c) 36, (d) 92 and (e) 396. Bright field (BF) images ($_1$) and corresponding SAED patterns ($_2$). Low magnification ADF STEM showing the FIB lift-outs ($_3$), BF STEM images ($_4$) and ADF images ($_5$) along with Zr EDS-maps and V EDS-maps at the bottom. The region of interest in the FIB lift-outs ($_3$) is indicated by a rectangle. After [48].

$\varepsilon \sim 18$, the diffraction spots become elongated and diffused (Fig. 5.7b$_2$), due to the accumulated distortion of the crystal lattice. This effect becomes even more pronounced for $\varepsilon \sim 36$ (Fig. 5.7c$_1$). The STEM BF and ADF micrographs for $\varepsilon \sim 18$ (Figs. 5.7b$_4$ and b$_5$) reveal the presence of V-rich inclusions, which dissolve only after applying higher

strains (Fig. 5.7c_4, c_5). The BF TEM micrograph for $\varepsilon \sim 92$ (Fig. 5.7d_1) shows an ultra-fine grained (UFG) microstructure. The corresponding SAED pattern (Fig. 5.7d_2) features rings (an identical selected area aperture is utilized for acquiring all diffraction patterns). At this applied strain, coarse dendritic and interdendritic regions are indistinguishable. Few remaining Zr-rich particles, about 190 nm in size, can still be observed (Fig. 5.7d_5). Increasing the HPT strain to $\varepsilon \sim 396$ leads to further structural refinement, see Fig. 5.7e_1 and e_4. However, the identical SAED patterns at $\varepsilon \sim 92$ and ~ 396 (5.7d_2 and e_2) demonstrate that the refinement is not intense. It should be noted that in Fig. 5.7d_1 and e_1, as well as in Fig. 5.7d_4 and e_4, the scale bar remains consistent. An enlarged view of Fig. 5.7e_1 indicates a grain size of approximately 50 nm. Similar to $\varepsilon \sim 92$, few small Zr-rich particles remain undissolved, yet exhibit a smaller size of about 45 nm.

5.3 Separation of deformation stages

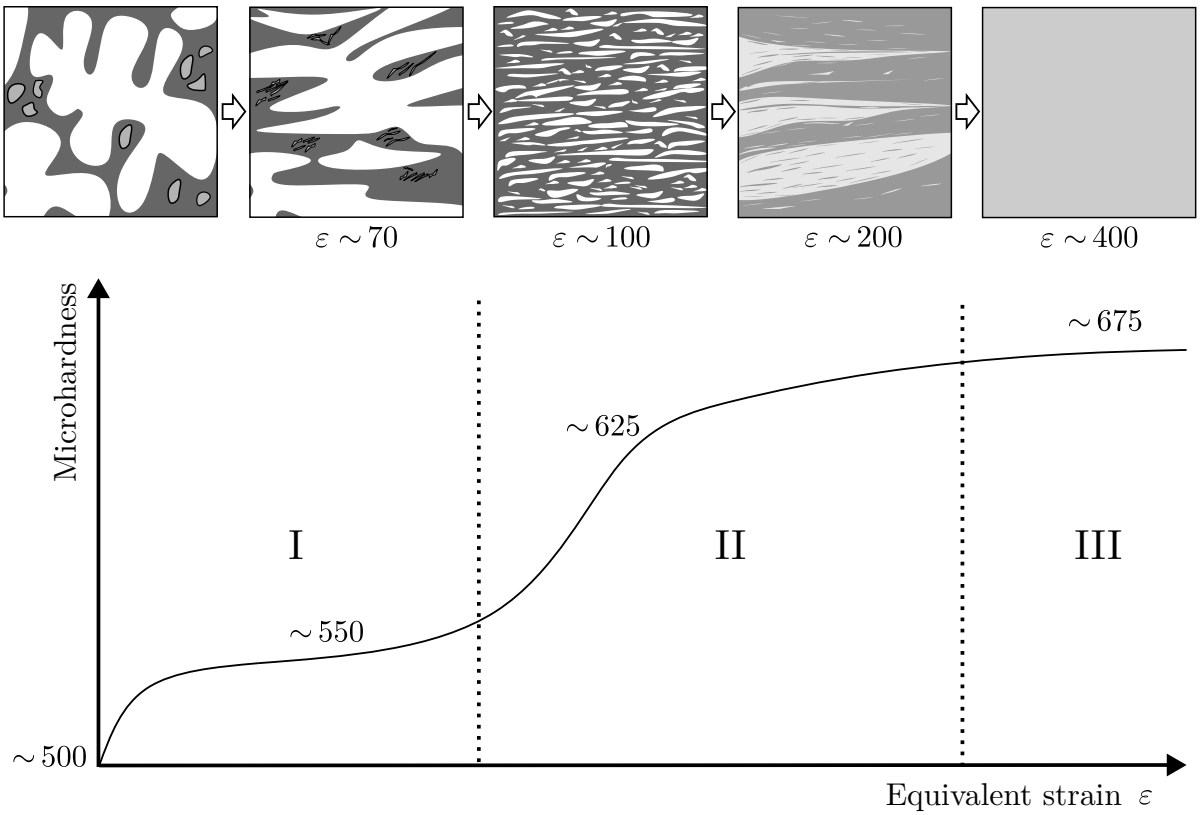

Fig. 5.8: Schematic illustration of microstructure and its corresponding microhardness evolution in the three deformation stages. After [48].

Fig. 5.8 provides an overview of the previously described microstructure evolution and the associated microhardness increase. However, there are still three questions that remain unclear and require further elaboration in the subsequent sections:

1. The uncommon moderate microhardness increase in the deformation stage I.
2. Possible underlying mechanisms for elemental mixing.
3. The discovered insights gained from the deformation-induced homogenization.

5.3.1 I: Strain localization and dissolution of V-inclusions

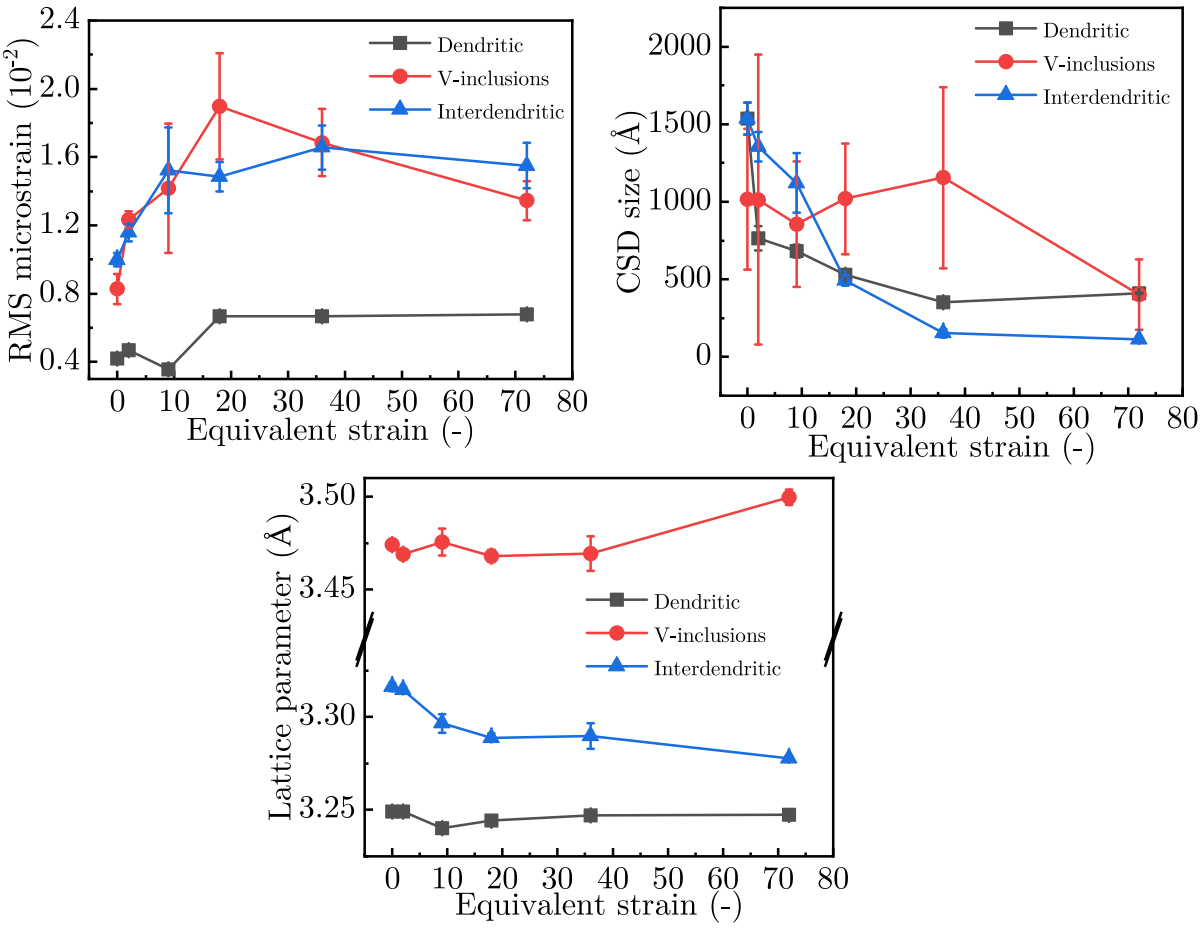

Fig. 5.9: Evolution of root mean square (RMS) microstrain, coherently scattering domain (CSD) size and lattice parameter obtained from Rietveld refinement in the first deformation stage. After [48].

In the broadening of XRD peaks, the effect of strain can be mathematically separated from that of crystallite/diffracting domain size, assuming that the broadening due to strain is Gaussian and the effect of size is Lorentzian [86]. Through Rietveld refinement of the synchrotron XRD data up to $\varepsilon \sim 72$, the evolution of the root mean square (RMS)

microstrain, coherently scattering domain (CSD) size and lattice parameter during the first deformation stage can be obtained, see Fig. 5.9.

The RMS strains in the interdendritic region (blue) and the V-rich inclusions (red) are significantly larger than that in the dendritic region (black), indicating a strain localization in the interdendritic region. Such a strain localization should result from an extensive deformation experienced by the V-rich inclusions. These results are consistent with the findings of EBSD investigations. In addition, the CSD sizes of all three phases show a decreasing tendency, pointing out the refinement of crystallites. The CSD size of the V-rich inclusions exhibit a considerable scattering, which might be due to their dissolution. It is important to note that crystallites are typically much smaller than grains. Hence, the CSD size derived from XRD deviates from the true grain size.

As the V-inclusions are found in the interdendritic region, where the strain localization is observed, it can be assumed that they primarily dissolve within this area. This assumption can be supported by the lattice parameter evolution of the interdendritic region. Since V exhibits a smaller atomic radius than the other five alloying elements, dissolution of V in the lattice of the interdendritic region should result in a decrease in the lattice parameter. It is also noteworthy that the lattice parameter of the V-rich inclusions shows an increase between $\varepsilon \sim 36$ and $\varepsilon \sim 72$. Considering the presence of multiple phases in the RHEA and the introduction of high shear strains by HPT, the change in lattice constants (increase in the V-rich inclusions and decrease in the interdendritic region) might contain the contribution from intergranular stresses between different phases. However, since the relationship between residual stress formation and HPT in the RHEA has not been thoroughly investigated in this dissertation, no conclusive inference can be made about such phenomenon.

To gain a more comprehensive understanding of the deformation stage I, local hardness in samples $N0.25$, $N2$ and $N4$ is investigated using the ultra-microhardness (UMH) test. The results for the dendritic and interdendritic region are shown in the left and right panels of Fig. 5.10, respectively.

It is evident that the two regions exhibit opposite strain hardening behaviors. The UMH of the dendritic region increases from 467 HV (as-cast) to approximately 540 HV at $\varepsilon \sim 60$, while that of the interdendritic region decreases from 517 HV (as-cast) to 480 HV at the same applied strain. During HPT, strain softening could result from various factors, including dynamic recrystallization, grain boundaries acting as dislocation sinks, and decomposition of supersaturated solid solutions [87–89]. However, in the present work, the softening of the interdendritic region can likely be attributed to the presence of soft V-inclusions. As shown in Figs. 5.4b-d, the deformed and refined V-inclusions are distributed in the interdendritic region.

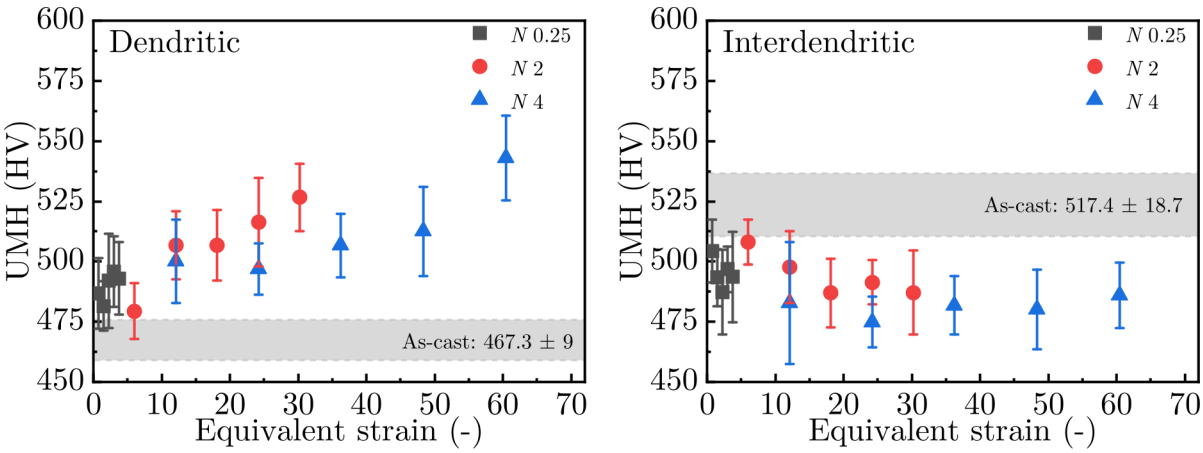

Fig. 5.10: Evolution of the ultra-microhardness (UMH) in stage I. Dendritic region (left) and interdendritic region (right). After [56].

This strain localization might explain the moderate microhardness increase observed in the deformation stage I. A similar phenomenon was reported in a study of the super-saturated solid solution of the Cu-Cr system processed by HPT [31]. Bachmaier et al. attributed this phenomenon to the refinement and saturation of microhardness within respective phases, analogous to the behavior of pure metals [31]. This is consistent with the TEM results, which show insignificant grain refinement within the strain range of $\varepsilon \sim 18$ to 36 (Figs. 5.7b and c).

5.3.2 II: Fragmentation, co-deformation and mixing

As V-inclusions dissolve in stage I, the primary deformation mechanism that follows should be the co-deformation of dendritic and interdendritic regions. In the deformation stage II, fragmentation as well as the recovery of the phases compete with each other to eventually reach an equilibrium [90]. As shown in Fig. 5.3d, the elongated dendritic region is fragmented at $\varepsilon \sim 92$. Although the fragmented regions are already too small for an accurate EDS measurement using SEM, it is still possible to roughly estimate the chemical composition via a line-scan, see Fig. 5.11a. The scanning line is oriented perpendicular to the shearing direction.

Significant segregations of Zr (brown) and Ta (blue) persist, compared to the theoretical value of 16.67 % for the senary HEA, with the segregation of Zr being more pronounced than that of Ta. In some Zr-rich areas, the Zr concentration exceeds 30 at. %. Note that the observed segregation is likely less than the actual one due to the large interaction volume of SEM-EDS. Up to $\varepsilon \sim 92$, it seems that the shear-induced mechanical mixing between the dendritic and the interdendritic regions is negligible. At $\varepsilon \sim 192$, the recombined stripe width exceeds 5 µm, allowing a more accurate quantitative EDS analysis on

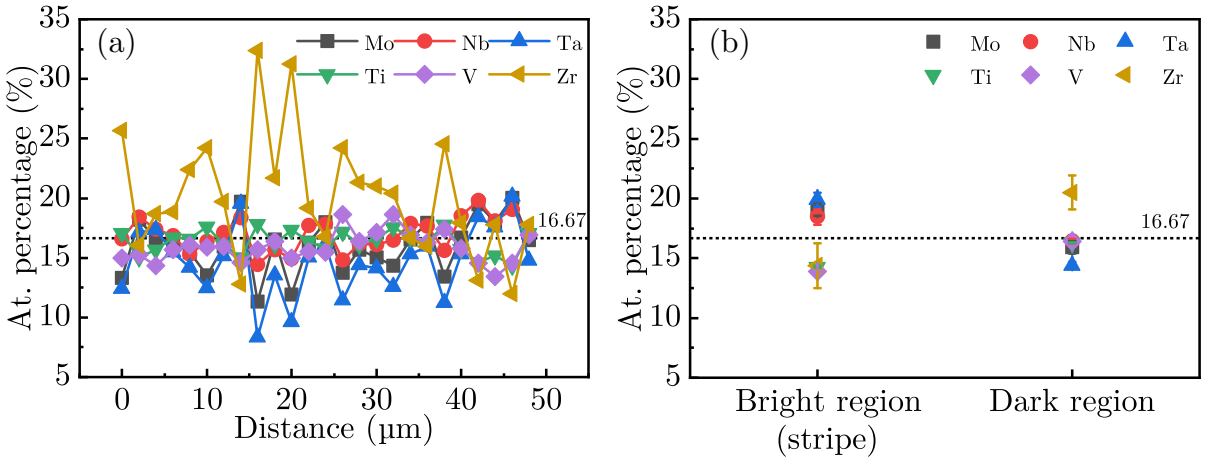

Fig. 5.11: (a) An EDS-line scan with a measurement distance of 2 µm at $\varepsilon \sim 92$. (b) EDS-point analysis of the recombined stripe and the matrix microstructure at $\varepsilon \sim 192$. After [48].

this microstructure (Fig. 5.11b). The elemental segregation is minimal at this applied strain, indicating a more intensive elemental mixing during shearing from $\varepsilon \sim 100$ to 200, compared to that in the range of $\varepsilon \sim 0$ to 100.

Various mechanisms have been suggested to explain deformation-induced mechanical mixing in immiscible systems. Bellon and Averback proposed a kinetic roughening of interfaces that leads to forced formation of a solid solution [91]. Yavari et al. suggested the Gibbs-Thomson effect, where fragmented phases dissolve into the other phase due to capillary pressure, after reaching a critical size (below 1 nm) [92]. More recently, a dislocation shuffling mechanism was proposed, in which dislocations glide across the heterophase interfaces and carry atoms from one phase to another [93, 94]. It was also proposed that one phase could eventually dissolve into the other by a process comparable to erosion or abrasion [95]. For the mechanical mixing of the dendritic and interdendritic regions of the present RHEA, the erosion and abrasion process proposed in [95] is a more plausible explanation for this phenomenon, as fragmented Zr-rich particles have been observed in the TEM results (see Figs. 5.7d_5 and e_5).

In addition to the EDS investigation, the XRD results are also studied carefully to reveal more insights into this stage. The (110)-peak of the dendritic region at $\varepsilon \sim 92$ is compared to that at ~ 396, see Fig. 5.12. By assuming the presence of only one group of peaks, the asymmetry left to the (110)-peak becomes apparent at $\varepsilon \sim 92$. This phenomenon indicates that the asymmetry persists during co-deformation and disappears after the microstructure is fully homogenized (at $\varepsilon \sim 396$). The observation confirms the existence of the interdendritic region's peaks, which evolve to an asymmetry by V-addition, as discussed in the microstructure study in Chapter 3.

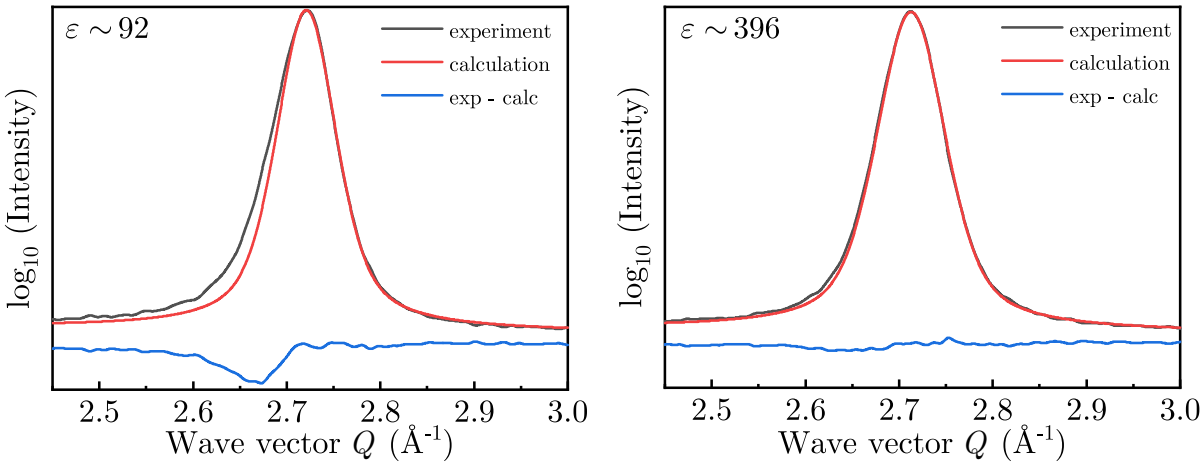

Fig. 5.12: Enlarged view of the (110)-peak in XRD at $\varepsilon \sim 92$ and ~ 396, assuming there exists only one BCC phase. After [48].

The lattice parameter of the dendritic region in stage II is difficult to determine using Rietveld refinement. This difficulty is not only due to the limited resolution of the laboratory X-ray diffractometer compared to the synchrotron beam, but also because the peaks of the two regions become closer in stage II than in the as-cast state and in stage I. However, the lattice parameter of the dendritic region can be estimated using a combined method of Rietveld refinement and peak fitting, see Fig. 5.13.

On the one hand, setting up a single phase in Rietveld refinement results in a lattice parameter larger than the actual value, as the calculated spectrum is shifted to smaller Q-values due to the asymmetry. This shift is because the Rietveld refinement program always tries to minimize the difference between the calculated spectrum and experimental results. On the other hand, fitting the peaks while ignoring the asymmetry would lead to a smaller lattice parameter than the actual value (see $\varepsilon \sim 92$ in Fig. 5.12). These two values establish the upper and lower bounds of the range for the actual lattice parameter, as indicated with the colored area in Fig. 5.13. The lattice constant of the dendritic region increases from about 3.25 to 3.28 Å in the deformation stage II, indicating the dissolution of the large atom Zr. Note that peak fitting is conducted on the (310)-peak instead of the (110)-peak. The error in determining a lattice parameter using laboratory XRD is proportional to $\cos^2\theta$ [96], suggesting less inaccuracy at larger diffraction angles θ (also larger Q-values). Hence, peak fitting of the (310)-peak results in an exacter lattice parameter than fitting the (110)-peak.

The determination of the single-phase composition in HEAs typically relies on the assumption that XRD patterns reveal only one group of peaks. As a result, although some HEAs exhibit deviations from chemical homogeneity, such as segregation or dendrites, they are still considered single-phase materials [9, 15]. A recent study demonstrates

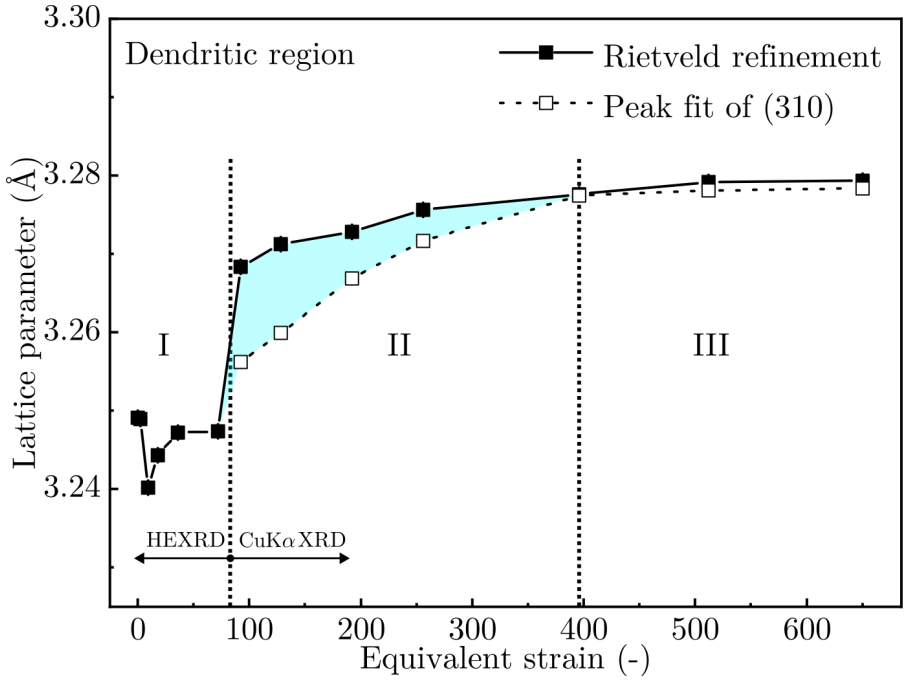

Fig. 5.13: Evolution of the lattice parameter of the dendritic region obtained from Rietveld refinement and peak fitting of the (310)-peak. The actual lattice parameter should be located between them (cyan area).

that "single-phase" HEAs containing elemental segregation comprise two phases with the same crystal structure and very similar lattice constants [16].

The findings of the present study clearly support the latter viewpoint. HEAs often comprise elements with comparable physical properties, such as atomic radii and electronic concentration. When multiple elements are grouped together in an HEA, the interactions between them can become complex, leading to phenomena such as a positive enthalpy of mixing that results in a miscibility gap. It is plausible that, following phase decomposition, these phases exhibit similar lattice constants such that they cannot be distinguished from each other in XRD patterns.

5.3.3 III: Deformation-induced homogenization

In the deformation stage III, the initially dendritic microstructure with microsegregation evolves into a chemically homogeneous state.

As discussed in Chapters 3 and 4, the microsegregation in the present RHEA can neither be homogenized using composition modification nor by heat treatment, especially due to the presence of V and Zr. The findings of the HPT-study reveal that homogenization of RHEAs could be achieved through severe plastic deformation. In addition to obtaining chemical homogeneity, the process refines the grains and enhances mechanical properties.

As also discussed in Chapter 4, microhardness often exhibits a linear relationship with yield strength [49], and hence the microhardness evolution represents a qualitative estimate of the change in yield strength. The yield strength σ_{y} of a metallic material can be expressed as the sum of the intrinsic lattice friction stress (σ_{fr}) and the contributions from different strengthening mechanisms [97]:

$$\sigma_{\mathrm{y}} = \sigma_{\mathrm{fr}} + \Delta\sigma_{\rho} + \Delta\sigma_{\mathrm{ss}} + \Delta\sigma_{\mathrm{ppt}} + \Delta\sigma_{\mathrm{gb}}, \tag{5.1}$$

where the terms on the right represent the contributions from the dislocation density $\Delta\sigma_{\rho}$, solid solution hardening $\Delta\sigma_{\mathrm{ss}}$, precipitation hardening $\Delta\sigma_{\mathrm{ppt}}$ and grain boundaries $\Delta\sigma_{\mathrm{gb}}$. Apparently, in the HPT processing, there is no contribution from the precipitation hardening $\Delta\sigma_{\mathrm{ppt}}$. The first increase in microhardness, up to $\varepsilon \sim 10$, is attributed to the increase in the dislocation density $\Delta\sigma_{\rho}$ (see Fig. 5.7a$_1$) and the grain refinement within the dendritic and the interdendritic regions $\Delta\sigma_{\mathrm{gb}}$ (see Fig. 5.5d$_3$). The lattice friction stress in BCC metals is much higher than in FCC metals. A recent study demonstrated that the compositional randomness in BCC HEAs could additionally increase the lattice friction stress, leading to an extremely high intrinsic strength σ_{fr} [98]. This high intrinsic strength might explain why the increase in microhardness in stage I is not significant compared to the initial microhardness. The substantial increase in microhardness at approximately $\varepsilon \sim 92$ is due to grain refinement by an intense fragmentation. As proposed by Bachmaier et al. [31], the decrease of the mean inter-particle distance (referred to as "phase spacing" in their study) in the Cu-Cr system could further refine grains that are already saturated. Since no intense grain refinement is observed from $\varepsilon \sim 92$ to $\varepsilon \sim 396$ in the TEM results, the subsequent increase in microhardness can only be attributed to the additional solid solution hardening $\Delta\sigma_{\mathrm{ss}}$ caused by the dissolution of the large atom Zr. Interestingly, the increase in microhardness due to grain refinement (~ 75 HV) in stage II does not differ much from that due to solid solution hardening (~ 50 HV).
The large atom Zr has been proved to particularly cause local chemical fluctuation and pronounced lattice distortion [43]. Although the results in this work also support this opinion, the fourteen RHEAs examined in [43] all had dendritic microstructures. It remains uncertain whether a homogenized microstructure would lead to improved mechanical properties for these RHEAs.

5.4 Concluding remarks

The HPT processing of the multi-phase RHEA MoNbTaTiVZr results in simultaneous chemical homogeneity and a UFG microstructure at an applied strain of $\varepsilon \sim 400$. The

investigation of the deformation mechanism indicates an initial strain localization in the interdendritic region, similar to the findings in the compression tests in Chapter 4. Therefore, the RHEA can also be ductile at RT. In addition to strain localization, the dissolution of V-inclusions is observed. Subsequent co-deformation of the dendritic and interdendritic regions occurs, during which elemental mixing is accelerated. As the elemental mixing progresses, the lattice parameter of the dendritic region increases and reaches saturation at the strain of chemical homogeneity. The examination of the microhardness contributions from grain refinement and solid solution hardening indicates that an increase in microhardness can be achieved by promoting the dissolution of Zr from the interdendritic region into the dendritic region. This finding provides new insights into the understanding of dendritic RHEAs.

Chapter 6

Conclusions and outlook

In the present work, the senary RHEA MoNbTaTiVZr fabricated using the vacuum arc-melting method is investigated. The study begins with the examination of microstructure, followed by the study of mechanical properties, to establish a comprehensive relationship between them. The fundamental understanding of the initial state prior to HPT facilitates a clearer picture of the microstructure and microhardness evolution during this process. A variety of characterization techniques are employed throughout the research, including SEM, (HE)XRD, EBSD, and TEM, as well as microhardness, local ultra-microhardness (UMH), and hot compression tests. Based on the findings, the following conclusions can be drawn.

The as-cast RHEA MoNbTaTiVZr exhibits a dendritic microstructure with a coarse grain size of about 100 µm. The HEXRD pattern displays two distinct groups of BCC phases and an asymmetry near the major BCC phase. The most segregated element is Zr, which separates the microstructure into Zr-depleted dendritic regions and Zr-rich interdendritic regions. In addition, V-rich inclusions are observed situated in the interdendritic regions. Motivated by the presence of the V-rich inclusions, a systematic study of the V-addition x is conducted for the dendritic RHEAs MoNbTaTiV$_x$Zr. The occurrence of V-rich inclusions is found from $x = 0.6$ onwards. The alteration of the HEXRD patterns indicates that the peak asymmetry is associated with the interdendritic region, and the peaks of the minor BCC phase belong to the V-rich inclusions. The formation of V-rich inclusions can be explained by the enrichment of V in the liquid phase during solidification when using the Scheil-Gulliver model. Such complex microsegregation, resulting from the combined effect of V and Zr, is confirmed by subsequent investigations of subgroup alloys. The compositional design strategy guided by natural mixing, as suggested in the literature, is ineffective in eliminating microsegregation. The microsegregation only disappears when both V and Zr are absent.

The investigation of mechanical properties indicates the positive effect of the alloying elements V and Zr in the as-cast RHEA MoNbTaTiVZr. The microhardness of the RHEA is significantly higher than that of Zr-free compositions (MoNbTaTiV and MoNbTaTi). The V-addition not only results in a slightly increased strength but also enhances ductility in the hot compression tests at 800 °C. The modest microhardness drop for $MoNbTaTiV_{0.6}Zr$, along with additional UMH test results, reveal the softness of the minor V-rich inclusions. During the compression test, the presence of these inclusions leads to strain localization in the interdendritic regions and to the refinement of the inclusions due to shear straining. The refined V-rich inclusions effectively impede crack propagation. At the same time, the high yield strength due to solid solution hardening by V and Zr is maintained, as the soft inclusions occupy only a minor fraction. As a result, the strength-ductility trade-off is overcome. A subsequent study of heat treatment demonstrates the thermal stability of the microstructure and mechanical properties at 800 °C, as well as revealing the persistence of microsegregation and the challenges associated with thermal homogenization.

In addition to the motivation of studying the multi-phase RHEA using severe plastic deformation, the HPT addresses the conflicting roles of V and Zr in causing undesired microsegregation while contributing to enhanced mechanical properties. HPT reveals *three* distinct deformation stages, separated by applied strains of approximately 70 and 400. In the *first* stage, strain localization is observed in the interdendritic region, a phenomenon similar to that found in the compression tests. Additionally, severe deformation and eventual dissolution of V-inclusions are observed. Despite grain refinement, the strain localization in this stage results in an unusually moderate increase in microhardness. In the *second* stage, fragmentation within the dendritic and the interdendritic regions leads to further grain refinement, causing a drastic microhardness increase at the applied strain of approximately 100. Following this significant increase in microhardness, the grain refinement reaches its saturation point at about 50 nm. The co-deformation of the fragmented regions paves the way for a gradual dissolution of the Zr-rich interdendritic region until the end of this stage. The dissolution of the large Zr atom results in an enlargement of the lattice constant of the dendritic region. This Zr dissolution also leads to an increase in microhardness due to the additional solid solution hardening. In the *third* stage, the alloy achieves chemical homogeneity. The peak asymmetry in XRD representing the interdendritic region disappears. Both the increasing lattice constant of the dendritic region and microhardness reach saturation. These novel findings could advance the understanding of the RHEAs, which commonly exhibit dendritic microstructures.

Based on the results, future research could pursue several directions. As nanocrystalline metallic materials may exhibit phase and grain size instability at high temperature, investigating the thermal stability of the deformation-induced homogenized state could provide deeper insights. This investigation can include both isochronal heat treatments, which address thermodynamic aspects, and isothermal treatments, which enable a study of the kinetics. By examining the microhardness evolution during heat treatments, a better understanding of the microstructure and mechanical properties due to static recrystallization and phase transformations could be obtained. Furthermore, exploring the intrinsically homogeneous state of the as-fabricated alloy for the present element system could be of interest. The concentrations of V and Zr could be finely tuned to maintain the chemically homogeneous microstructure of the base composition MoNbTaTi, while preserving the solid solution hardening effect provided by V and Zr. As the homogenization observed in HPT is similar to that of mechanical alloying, it would be worthwhile investigating the microstructure and mechanical properties of the equimolar senary RHEA fabricated using powder metallurgy. Additionally, during deformation-induced homogenization, quantification of the actual lattice distortion could be achieved using pair distribution function analysis. This approach could also be employed when exploring the intrinsically homogeneous composition of the as-cast state by fine-tuning V and Zr concentrations.

Appendix A

Laboratory X-ray diffractograms related to high-pressure torsion

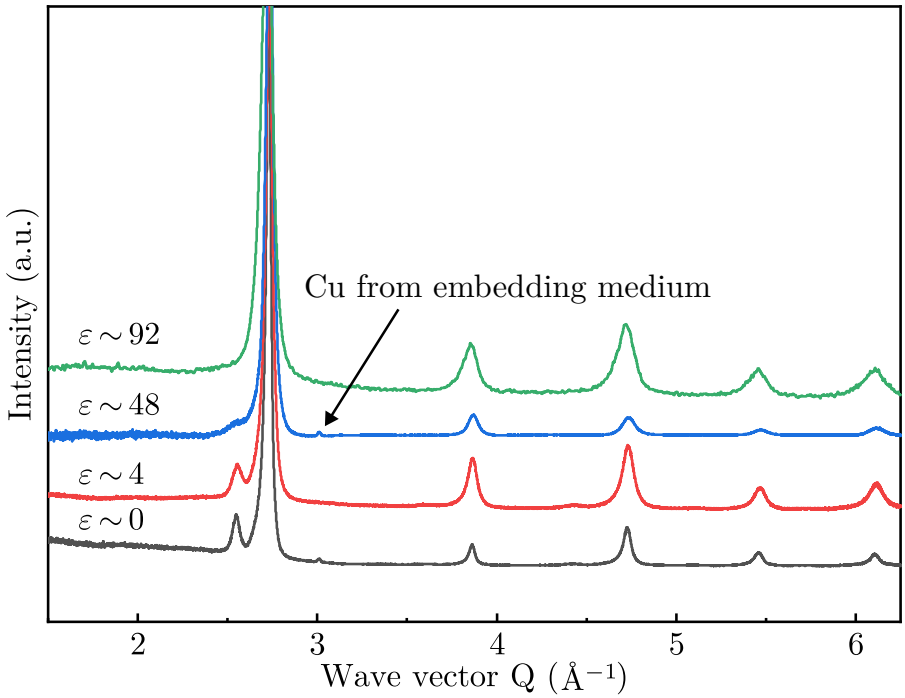

Fig. A.1: Laboratory XRD patterns of HPT-processed RHEA MoNbTaTiVZr in the deformation stage I.

Bibliography

[1] J. Fadok. Advanced gas turbine materials, design and technology. In D. Roddy, editor, *Advanced Power Plant Materials, Design and Technology*, pages 3–31. Woodhead Publishing, Cambridge, UK, 2010.

[2] O. N. Senkov, D. B. Miracle, K. J. Chaput, and J. P. Couzinie. Development and exploration of refractory high entropy alloys - A review. *Journal of Materials Research*, 33(19):3092–3128, 2018.

[3] J. W. Yeh, S. K. Chen, S. J. Lin, J. Y. Gan, T. S. Chin, T. T. Shun, C. H. Tsau, and S. Y. Chang. Nanostructured high-entropy alloys with multiple principal elements: Novel alloy design concepts and outcomes. *Advanced Engineering Materials*, 6(5):299–303+274, 2004.

[4] B. Cantor, I. Chang, P. Knight, and A. Vincent. Microstructural development in equiatomic multicomponent alloys. *Materials Science and Engineering: A*, 375:213–218, 2004.

[5] Y. Zhang, T. T. Zuo, Z. Tang, M. C. Gao, K. A. Dahmen, P. K. Liaw, and Z. P. Lu. Microstructures and properties of high-entropy alloys. *Progress in Materials Science*, 61:1–93, 2014.

[6] D. B. Miracle and O. N. Senkov. A critical review of high entropy alloys and related concepts. *Acta Materialia*, 122:448–511, 2017.

[7] Z. Li, K. G. Pradeep, Y. Deng, D. Raabe, and C. C. Tasan. Metastable high-entropy dual-phase alloys overcome the strength-ductility trade-off. *Nature*, 534(7606):227–230, 2016.

[8] S. Gorsse, D. B. Miracle, and O. N. Senkov. Mapping the world of complex concentrated alloys. *Acta Materialia*, 135:177–187, 2017.

[9] O. N. Senkov, G. B. Wilks, D. B. Miracle, C. P. Chuang, and P. K. Liaw. Refractory high-entropy alloys. *Intermetallics*, 18(9):1758–1765, 2010.

[10] O. N. Senkov, J. M. Scott, S. V. Senkova, D. B. Miracle, and C. F. Woodward. Microstructure and room temperature properties of a high-entropy TaNbHfZrTi alloy. *Journal of Alloys and Compounds*, 509(20):6043–6048, 2011.

[11] Q. Ding, Y. Zhang, X. Chen, X. Fu, D. Chen, S. Chen, L. Gu, F. Wei, H. Bei, Y. Gao, M. Wen, J. Li, Z. Zhang, T. Zhu, R. O. Ritchie, and Q. Yu. Tuning element distribution, structure and properties by composition in high-entropy alloys. *Nature*, 574(7777):223–227, 2019.

[12] F. Wang, G. H. Balbus, S. Xu, Y. Su, J. Shin, P. F. Rottmann, K. E. Knipling, J.-C. Stinville, L. H. Mills, O. N. Senkov, I. J. Beyerlein, T. M. Pollock, and D. S. Gianola. Multiplicity of dislocation pathways in a refractory multiprincipal element alloy. *Science*, 370(6512):95–101, 2020.

[13] O. N. Senkov, G. B. Wilks, J. M. Scott, and D. B. Miracle. Mechanical properties of Nb25Mo25Ta25W25 and V20Nb20Mo20Ta20W20 refractory high entropy alloys. *Intermetallics*, 19(5):698–706, 2011.

[14] O. N. Senkov, J. K. Jensen, A. L. Pilchak, D. B. Miracle, and H. L. Fraser. Compositional variation effects on the microstructure and properties of a refractory high-entropy superalloy AlMo0.5NbTa0.5TiZr. *Materials & Design*, 139:498–511, 2018.

[15] M. C. Gao, B. Zhang, S. Yang, and S. M. Guo. Senary Refractory High-Entropy Alloy HfNbTaTiVZr. *Metallurgical and Materials Transactions A: Physical Metallurgy and Materials Science*, 47(7):3333–3345, 2016.

[16] B. Zhang, Y. Mu, M. C. Gao, W. J. Meng, and S. M. Guo. On single-phase status and segregation of an as-solidified septenary refractory high entropy alloy. *MRS Communications*, 7(1):78–83, 2017.

[17] M. Wang, Z. Ma, Z. Xu, and X. Cheng. Designing VxNbMoTa refractory high-entropy alloys with improved properties for high-temperature applications. *Scripta Materialia*, 191:131–136, 2021.

[18] R. Feng, B. Feng, M. C. Gao, C. Zhang, J. C. Neuefeind, J. D. Poplawsky, Y. Ren, K. An, M. Widom, and P. K. Liaw. Superior high-temperature strength in a supersaturated refractory high-entropy alloy. *Advanced Materials*, 33(48):2102401, 2021.

[19] T. Whitfield, E. Pickering, K. Christofidou, C. Jones, H. Stone, and N. Jones. Elucidating the microstructural development of refractory metal high entropy superalloys via the Ti–Ta–Zr constituent system. *Journal of Alloys and Compounds*, 818:152935, 2020.

[20] A. P. Zhilyaev and T. G. Langdon. Using high-pressure torsion for metal processing: Fundamentals and applications. *Progress in Materials Science*, 53(6):893–979, 2008.

[21] R. Pippan, S. Scheriau, A. Hohenwarter, and M. Hafok. Advantages and limitations of HPT: A review. *Materials Science Forum*, 584–586:16–21, 2008.

[22] R. Z. Valiev, R. K. Islamgaliev, and I. V. Alexandrov. Bulk nanostructured materials from severe plastic deformation. *Progress in materials science*, 45(2):103–189, 2000.

[23] Y. Harai, M. Kai, K. Kaneko, Z. Horita, and T. G. Langdon. Microstructural and mechanical characteristics of AZ61 magnesium alloy processed by high-pressure torsion. *Materials transactions*, 49(1):76–83, 2008.

[24] B. Schuh, F. Mendez-Martin, B. Völker, E. P. George, H. Clemens, R. Pippan, and A. Hohenwarter. Mechanical properties, microstructure and thermal stability of a nanocrystalline CoCrFeMnNi high-entropy alloy after severe plastic deformation. *Acta Materialia*, 96:258–268, 2015.

[25] H. Shahmir, J. He, Z. Lu, M. Kawasaki, and T. G. Langdon. Evidence for superplasticity in a CoCrFeNiMn high-entropy alloy processed by high-pressure torsion. *Materials Science and Engineering: A*, 685:342–348, 2017.

[26] B. Schuh, B. Völker, J. Todt, N. Schell, L. Perrière, J. Li, J. P. Couzinié, and A. Hohenwarter. Thermodynamic instability of a nanocrystalline, single-phase TiZrNbHfTa alloy and its impact on the mechanical properties. *Acta Materialia*, 142:201–212, 2018.

[27] S. Taheriniya, F. A. Davani, S. Hilke, M. Hepp, C. Gadelmeier, M. R. Chellali, T. Boll, H. Rösner, M. Peterlechner, C. Gammer, S. V. Divinski, B. Butz, U. Glatzel, H. Hahn, and G. Wilde. High entropy alloy nanocomposites produced by high pressure torsion. *Acta Materialia*, 208:116714, 2021.

[28] A. Kilmametov, R. Kulagin, A. Mazilkin, S. Seils, T. Boll, M. Heilmaier, and H. Hahn. High-pressure torsion driven mechanical alloying of CoCrFeMnNi high entropy alloy. *Scripta Materialia*, 158:29–33, 2019.

[29] Q. H. Tang, Y. Huang, Y. Y. Huang, X. Z. Liao, T. G. Langdon, and P. Q. Dai. Hardening of an Al0.3CoCrFeNi high entropy alloy via high-pressure torsion and thermal annealing. *Materials Letters*, 151:126–129, 2015.

[30] P. Edalati, R. Floriano, Y. Tang, A. Mohammadi, K. D. Pereira, A. D. Luchessi, and K. Edalati. Ultrahigh hardness and biocompatibility of high-entropy alloy TiAlFeCoNi processed by high-pressure torsion. *Materials Science and Engineering: C*, 112:110908, 2020.

[31] A. Bachmaier, G. B. Rathmayr, M. Bartosik, D. Apel, Z. Zhang, and R. Pippan. New insights on the formation of supersaturated solid solutions in the Cu-Cr system deformed by high-pressure torsion. *Acta Materialia*, 69:301–313, 2014.

[32] K. S. Kormout, R. Pippan, and A. Bachmaier. Deformation-induced supersaturation in immiscible material systems during high-pressure torsion. *Advanced Engineering Materials*, 19(4):1–19, 2017.

[33] W. D. Callister and D. G. Rethwisch. *Materials science and engineering: an introduction*, pages 83–85. John Wiley & Sons, New York, NY, 7th edition, 2007.

[34] Y. Zhang, Y. J. Zhou, J. P. Lin, G. L. Chen, and P. K. Liaw. Solid-solution phase formation rules for multi-component alloys. *Advanced Engineering Materials*, 10(6):534–538, 2008.

[35] X. Yang and Y. Zhang. Prediction of high-entropy stabilized solid-solution in multi-component alloys. *Materials Chemistry and Physics*, 132(2-3):233–238, 2012.

[36] S. Guo and C. T. Liu. Phase stability in high entropy alloys: Formation of solid-solution phase or amorphous phase. *Progress in Natural Science: Materials International*, 21(6):433–446, 2011.

[37] M. Poletti and L. Battezzati. Electronic and thermodynamic criteria for the occurrence of high entropy alloys in metallic systems. *Acta Materialia*, 75:297–306, 2014.

[38] A. Takeuchi and A. Inoue. Classification of bulk metallic glasses by atomic size difference, heat of mixing and period of constituent elements and its application to characterization of the main alloying element. *Materials Transactions*, 46(12):2817–2829, 2005.

[39] A. Takeuchi and A. Inoue. Quantitative evaluation of critical cooling rate for metallic glasses. *Materials Science and Engineering: A*, 304:446–451, 2001.

[40] J. B. Mann, T. L. Meek, E. T. Knight, J. F. Capitani, and L. C. Allen. Configuration energies of the d-block elements. *Journal of the American Chemical Society*, 122(21):5132–5137, 2000.

[41] S. Ranganathan. Alloyed pleasures: Multimetallic cocktails. *Current science*, 85(10):1404–1406, 2003.

[42] B. Yin, F. Maresca, and W. A. Curtin. Vanadium is an optimal element for strengthening in both fcc and bcc high-entropy alloys. *Acta Materialia*, 188:486–491, 2020.

[43] Y. Tong, S. Zhao, H. Bei, T. Egami, Y. Zhang, and F. Zhang. Severe local lattice distortion in Zr- and/or Hf-containing refractory multi-principal element alloys. *Acta Materialia*, 183:172–181, 2020.

[44] C. Kittel. *Introduction to solid state physics*, pages 21, 51, 71. John Wiley & Sons, Hoboken, NJ, 8th edition, 2004.

[45] T. Prohaska, J. Irrgeher, J. Benefield, J. K. Böhlke, L. A. Chesson, T. B. Coplen, T. Ding, P. J. Dunn, M. Gröning, N. E. Holden, H. A. J. Meijer, H. Moossen, A. Possolo, Y. Takahashi, J. Vogl, T. Walczyk, J. Wang, M. E. Wieser, S. Yoneda, X.-K. Zhu, and J. Meija. Standard atomic weights of the elements 2021 (IUPAC Technical Report). *Pure and Applied Chemistry*, 94(5):573–600, 2022.

[46] A. P. Hammersley, S. O. Svensson, M. Hanfland, A. N. Fitch, and D. Häusermann. Two-dimensional detector software: From real detector to idealised image or two-theta scan. *High Pressure Research*, 14(4-5):235–248, 1996.

[47] L. Lutterotti, S. Matthies, and H.-R. Wenk. MAUD (material analysis using diffraction): a user friendly Java program for Rietveld texture analysis and more. In *Proceeding of the twelfth international conference on textures of materials (ICOTOM-12)*, volume 1, page 1599. NRC Research Press Ottowa, Canada, 1999.

[48] C. Duan, A. Kostka, X. Li, Z. Peng, P. Kutlesa, R. Pippan, and E. Werner. Deformation-induced homogenization of the multi-phase senary high-entropy alloy MoNbTaTiVZr processed by high-pressure torsion. *Materials Science and Engineering: A*, 871:144923, 2023.

[49] A. C. Fischer-Cripps. *Introduction to contact mechanics*, pages 8–14, 25. Springer, New York, NY, 2nd edition, 2007.

[50] C. A. Schneider, W. S. Rasband, and K. W. Eliceiri. NIH Image to ImageJ: 25 years of image analysis. *Nature Methods*, 9(7):671–675, 2012.

[51] J.-O. Andersson, T. Helander, L. Höglund, P. Shi, and B. Sundman. Thermo-Calc & DICTRA, computational tools for materials science. *Calphad*, 26(2):273–312, 2002.

[52] G. Gottstein. *Physical foundations of materials science*, page 375. Springer, Berlin, Heidelberg, 1st edition, 2004.

[53] P. Schaffnit, C. Stallybrass, J. Konrad, F. Stein, and M. Weinberg. A Scheil–Gulliver model dedicated to the solidification of steel. *Calphad*, 48:184–188, 2015.

[54] E. Scheil. Bemerkungen zur Schichtkristallbildung. *Zeitschrift für Metallkunde*, 34(3):70–72, 1942.

[55] G. Gulliver. The quantitative effect of rapid cooling upon the constitution of binary alloys. *Journal of Institute of Metals*, 9(1):120–157, 1913.

[56] C. Duan, M. Reiberg, P. Kutlesa, X. Li, R. Pippan, and E. Werner. Strain-hardening properties of the high-entropy alloy MoNbTaTiVZr processed by high-pressure torsion. *Continuum Mechanics and Thermodynamics*, 34(2):475–489, 2022.

[57] L. Wang, T. Cao, X. Liu, B. Wang, K. Jin, Y. Liang, L. Wang, F. Wang, Y. Ren, J. Liang, and Y. Xue. A novel stress-induced martensitic transformation in a single-phase refractory high-entropy alloy. *Scripta Materialia*, 189:129–134, 2020.

[58] S. Ge, H. Fu, L. Zhang, H. Mao, H. Li, A. Wang, W. Li, and H. Zhang. Effects of Al addition on the microstructures and properties of MoNbTaTiV refractory high entropy alloy. *Materials Science and Engineering: A*, 784:139275, 2020.

[59] J. B. Kortright and A. C. Thompson. X-ray emission energies. In A. C. Thompson and D. Vaughan, editors, *X-ray data booklet*, pages 1–8. Lawrence Berkeley National Laboratory, University of California Berkeley, CA, 2001.

[60] N. Brodusch, K. Zaghib, and R. Gauvin. Improvement of the energy resolution of energy dispersive spectrometers (EDS) using Richardson–Lucy deconvolution. *Ultramicroscopy*, 209:112886, 2020.

[61] Y. Mu, H. Liu, Y. Liu, X. Zhang, Y. Jiang, and T. Dong. An ab initio and experimental studies of the structure, mechanical parameters and state density on the refractory high-entropy alloy systems. *Journal of Alloys and Compounds*, 714:668–680, 2017.

[62] T. Nagase, M. Todai, T. Hori, and T. Nakano. Microstructure of equiatomic and non-equiatomic Ti-Nb-Ta-Zr-Mo high-entropy alloys for metallic biomaterials. *Journal of Alloys and Compounds*, 753:412–421, 2018.

[63] T. Hori, T. Nagase, M. Todai, A. Matsugaki, and T. Nakano. Development of non-equiatomic Ti-Nb-Ta-Zr-Mo high-entropy alloys for metallic biomaterials. *Scripta Materialia*, 172:83–87, 2019.

[64] H. Okamoto, M. Schlesinger, and E. Mueller. Binary alloy phase diagrams. In *Alloy Phase Diagrams*. ASM International, 2016.

[65] J. Zhang, C. Gadelmeier, S. Sen, R. Wang, X. Zhang, Y. Zhong, U. Glatzel, B. Grabowski, G. Wilde, and S. V. Divinski. Zr diffusion in bcc refractory high entropy alloys: A case of 'non-sluggish' diffusion behavior. *Acta Materialia*, 233:117970, 2022.

[66] H. Yao, J. Qiao, J. Hawk, H. Zhou, M. Chen, and M. Gao. Mechanical properties of refractory high-entropy alloys: Experiments and modeling. *Journal of Alloys and Compounds*, 696:1139–1150, 2017.

[67] Y. Zong, N. Hashimoto, and H. Oka. Study on irradiation effects of refractory bcc high-entropy alloy. *Nuclear Materials and Energy*, 31:101158, 2022.

[68] S. Wei, S. J. Kim, J. Kang, Y. Zhang, Y. Zhang, T. Furuhara, E. S. Park, and C. C. Tasan. Natural-mixing guided design of refractory high-entropy alloys with as-cast tensile ductility. *Nature Materials*, 19(11):1175–1181, 2020.

[69] P. Villars, M. Berndt, K. Brandenburg, K. Cenzual, J. Daams, F. Hulliger, T. Massalski, H. Okamoto, K. Osaki, A. Prince, H. Putz, and S. Iwata. The Pauling File. *Journal of Alloys and Compounds*, 367(1-2):293–297, 2004.

[70] W. Hu, Z. Huang, Q. Yu, Y. Wang, Y. Jiao, C. Lei, L. Cai, H. Zhai, and Y. Zhou. Ti2AlC triggered in-situ ultrafine TiC/Inconel 718 composites: Microstructure and enhanced properties. *Journal of Materials Science & Technology*, 51:70–78, 2020.

[71] M. Akmal, H.-K. Park, and H. J. Ryu. Plasma spheroidized MoNbTaTiZr high entropy alloy showing improved plasticity. *Materials Chemistry and Physics*, 273:125060, 2021.

[72] G. Cheng, K. Choi, X. Hu, and X. Sun. Determining individual phase properties in a multi-phase Q&P steel using multi-scale indentation tests. *Materials Science and Engineering: A*, 652:384–395, 2016.

[73] R. Rodrıguez and I. Gutierrez. Correlation between nanoindentation and tensile properties: influence of the indentation size effect. *Materials Science and Engineering: A*, 361(1-2):377–384, 2003.

[74] Y. Zhang, J. P. Liu, S. Y. Chen, X. Xie, P. K. Liaw, K. A. Dahmen, J. W. Qiao, and Y. L. Wang. Serration and noise behaviors in materials. *Progress in Materials Science*, 90:358–460, 2017.

[75] F. G. Coury, M. Kaufman, and A. J. Clarke. Solid-solution strengthening in refractory high entropy alloys. *Acta Materialia*, 175:66–81, 2019.

[76] A. S. Argon. *Strengthening Mechanisms in Crystal Plasticity*, pages 163–181. Oxford University Press, Oxford, 2007.

[77] D. Hull and D. J. Bacon. *Introduction to dislocations*, pages 139–142. Butterworth-Heinemann, Oxford, 1st edition, 2001.

[78] X. Wang, H. Li, K. Chandrashekhara, S. Rummel, S. Lekakh, D. Van Aken, and R. O'Malley. Inverse finite element modeling of the barreling effect on experimental stress-strain curve for high temperature steel compression test. *Journal of Materials Processing Technology*, 243:465–473, 2017.

[79] Y. Ye, C. Liu, and Y. Yang. A geometric model for intrinsic residual strain and phase stability in high entropy alloys. *Acta Materialia*, 94:152–161, 2015.

[80] M. Leffler and J. Helble. Development of nanoscale ceramics for advanced power applications. Technical report, University of Connecticut, Storrs, CT, 1999.

[81] O. N. Senkov, J. M. Scott, S. V. Senkova, F. Meisenkothen, D. B. Miracle, and C. F. Woodward. Microstructure and elevated temperature properties of a refractory TaNbHfZrTi alloy. *Journal of Materials Science*, 47:4062–4074, 2012.

[82] O. N. Senkov, S. V. Senkova, and C. F. Woodward. Effect of aluminum on the microstructure and properties of two refractory high-entropy alloys. *Acta Materialia*, 68:214–228, 2014.

[83] N. Stepanov, D. Shaysultanov, G. Salishchev, and M. Tikhonovsky. Structure and mechanical properties of a light-weight AlNbTiV high entropy alloy. *Materials Letters*, 142:153–155, 2015.

[84] O. N. Senkov, S. V. Senkova, D. B. Miracle, and C. F. Woodward. Mechanical properties of low-density, refractory multi-principal element alloys of the Cr-Nb-Ti-V-Zr system. *Materials Science and Engineering: A*, 565:51–62, 2013.

[85] Inc. Haynes International. Haynes 230 alloy (UNS N06230). *Material data sheet*, 2021.

[86] R. Delhez, T. H. De Keijser, J. Langford, D. Louër, E. Mittemeijer, and E. Sonneveld. Crystal imperfection broadening and peak shape in the Rietveld method. In R. A. Young, editor, *The Rietveld method*, pages 132–166. Oxford University Press, New York, NY, 1993.

[87] J. Xu, J. Li, C. T. Wang, D. Shan, B. Guo, and T. G. Langdon. Evidence for an early softening behavior in pure copper processed by high-pressure torsion. *Journal of Materials Science*, 51(4):1923–1930, 2016.

[88] Y. Ito, K. Edalati, and Z. Horita. High-pressure torsion of aluminum with ultra-high purity (99.9999%) and occurrence of inverse Hall-Petch relationship. *Materials Science and Engineering: A*, 679:428–434, 2017.

[89] A. Mazilkin, B. Straumal, M. Borodachenkova, R. Valiev, O. Kogtenkova, and B. Baretzky. Gradual softening of Al–Zn alloys during high-pressure torsion. *Materials Letters*, 84:63–65, 2012.

[90] R. Pippan, S. Scheriau, A. Taylor, M. Hafok, A. Hohenwarter, and A. Bachmaier. Saturation of fragmentation during severe plastic deformation. *Annual Review of Materials Research*, 40(1):319–343, 2010.

[91] P. Bellon and R. S. Averback. Nonequilibrium roughening of interfaces in crystals under shear: Application to ball milling. *Physical Review Letters*, 74(10):1819–1822, 1995.

[92] A. R. Yavari, P. J. Desré, and T. Benameur. Mechanically driven alloying of immiscible elements. *Physical Review Letters*, 68(14):2235–2238, 1992.

[93] D. Raabe, S. Ohsaki, and K. Hono. Mechanical alloying and amorphization in Cu–Nb–Ag in situ composite wires studied by transmission electron microscopy and atom probe tomography. *Acta Materialia*, 57(17):5254–5263, 2009.

[94] D. Raabe, P. P. Choi, Y. Li, A. Kostka, X. Sauvage, F. Lecouturier, K. Hono, R. Kirchheim, R. Pippan, and D. Embury. Metallic composites processed via ex-

treme deformation: Toward the limits of strength in bulk materials. *MRS Bulletin*, 35(12):982–991, 2010.

[95] A. Bachmaier, J. Schmauch, H. Aboulfadl, A. Verch, and C. Motz. On the process of co-deformation and phase dissolution in a hard-soft immiscible Cu-Co alloy system during high-pressure torsion deformation. *Acta Materialia*, 115:333–346, 2016.

[96] B. D. Cullity. *Elements of X-ray Diffraction*, pages 326–333. Addison-Wesley Publishing, Reading, MA, 1956.

[97] Z. Wu, H. Bei, G. M. Pharr, and E. P. George. Temperature dependence of the mechanical properties of equiatomic solid solution alloys with face-centered cubic crystal structures. *Acta Materialia*, 81:428–441, 2014.

[98] L. Zhang, Y. Xiang, J. Han, and D. J. Srolovitz. The effect of randomness on the strength of high-entropy alloys. *Acta Materialia*, 166:424–434, 2019.